STUDIES OF ZINC AND PHARMACEUTICAL

NANOPARTICLES

STUDIES OF ZINC AND PHARMACEUTICAL NANOPARTICLES

By

LINA GUNAWAN, B. Eng.

A Thesis

Submitted to the School of Graduate Studies

In Partial Fulfillment of the Requirements

For the Degree

Master of Applied Science in Materials Engineering

McMaster University

Master of Applied Science (2005)   McMaster University

(Materials Science and Engineering)   Hamilton, Ontario

Title :   Studies of Zinc and Pharmaceutical Nanoparticles

Author :   Lina Gunawan, B. Eng.

Supervisor :   Dr. G. P. Johari

Number of pages :   xiii, 137

ABSTRACT

This study is on thermodynamics of crystalline nanoparticles of materials. It provides measurements of the equilibrium melting point of nanocrystals of zinc in a size distribution of 30 - 120 nm, as observed by using Philips CM12 TEM and JEOL 2010F TEM/STEM, and of the heat capacity, and melting enthalpy by using Perkin-Elmer Pyris-Diamond and TA Q100 Calorimeters. The observed melting point of zinc nanoparticles is lower than that of the bulk zinc, but their heat capacity increases and enthalpy of melting decreases. During heating, the nanoparticles oxidizes and forms zinc oxide surface layer reducing the amount and size of zinc nanocrystals. Calculations based upon the Debye theory for heat capacity show that the surface atoms on the zinc nanoparticles have ~ 55 % larger vibrational amplitude and therefore increase the entropy of the surface layer over that of the interior of the particles. During cooling, the crystallization of zinc oxide encaged zinc nanodroplets occurs in two stages, which are heterogeneous and homogeneous nucleations. As the amount of zinc nanocrystals decreases and the liquid-zinc oxide interface increases, homogeneous nucleation becomes less dominant and the two-stage crystallization merges.

Nano-pharmaceuticals were produced by incorporating them in a nanoporous amorphous polymer matrix by using a technique based on diffusion method. The presence of embedded nano-pharmaceuticals is shown by their lower melting point relative to the bulk pharmaceuticals and by peak-broadening of x-ray diffraction, which shows that their size lies in 70 - 100 nm range. Although no phase inversion between allotropic forms of the pharmaceutical was observed, a sample calculation for polymorphs of tin shows that such phase inversion should occur at a smaller particle size at a lower temperature. In general, these findings show the effects of the increase in the surface energy relative to bulk energy of nanoparticles, and the consequent differences between the properties of their surface atoms relative to the interior atoms.

ACKNOWLEDGEMENTS

TABLE OF CONTENTS

LIST OF TABLES

LIST OF FIGURES

Chapter 1. General Introduction to Nanomaterials and Their Thermodynamics

1.1 Nanomaterials

Nano-materials are defined as those solids or liquids in which the characteristic length scale of crystal or amorphous particles or liquid droplets lies within the range of one to several hundred nanometers [Hunt (2004)]. It has been observed by Gleiter (2000) that physical properties at this size scale of matter are generally different from those of bulk materials. However, far beneath our awareness, nanomaterials have actually been important in the materials field for quite a long time. A few early examples are: the incorporation of gold nanoparticles in stained glass in 10 A. D. which exhibit a range of colors [The Royal Society and The Royal Academy of Engineering (2004)]; nano-sized carbon black particles for tire reinforcement for the past 100 years [Stix (2001)]; and precipitation hardening in copper aluminum alloys found in 1906 by Wilm [Hornbogen (2001)]. Evolution of nanotechnology is now faster with more products expected to appear in the future. There have already been applications of nanomaterials and nanotechnology in the military [Roncone (2004), Reynolds (2004)], cosmetics industries [www.lorealusa.com (2004)], biotechnology and drugs [Bergese et al. (2004), Fattal (2004)], microelectronics [Rittner (2004)], gas sensors [Vlachos and Xenoulis (1998), Ferroni et al. (1999), Hooker (2002)], and energy and environment [Gillet (1996)].

Dobson (1999) has reviewed the new properties of nanomaterials that are expected to have a significant potential in the perceived revolution in the use of materials. According to him, these properties are:

(1) enhanced luminescence, due to the localization of electron-hole pairs in small particles,

(2) very high permeability but no magnetic hysteresis loss,

(3) very high dielectric permittivity and low loss,

1

(4) enhanced reactivity and catalytic properties because of a high percentage of surface atoms, and,

(5) increased toughness and ductility in ceramic materials.

The resulting broad scope of studies of nanomaterials in recent years has been reviewed in a number of articles [Johari (1998), Dobson (1999), Valiev (2002)], and for convenience such materials have been classified according to [Liz-Marzan et al. (2003)]:

(1) Materials type: These may be either nanoamorphous or nanocrystalline. Such materials consist of amorphous or crystalline solids embedded in nanopores, solids that contain nanometer size crystallites in the bulk, and nanocrystallites embedded in a similar or different type of matrix. The last type is known as nanocomposite.

(2) Materials shape: These may be nanorods, nanowires, nanorings, nanotubes and nanoparticles.

Since change in materials properties on dimension reduction in general leads us into different perspectives of their behavior, it is important to understand how their properties become size-dependent, as nanometer size is approached. Firstly, and fundamentally, the changes in materials properties are due to a prominent change in the structure and configuration of atoms within matter as the size of the particle is reduced to nanometer scale, and secondly due to the very high ratio of the surface area to volume when compared to that of bulk materials. In nanocrystalline materials, a large percentage of atoms reside on the grain boundaries of the solid, which causes the position of atoms within the unit cell inside the nanocrystallites to differ from those in the bulk crystals. Similarly, the atoms on the surface of free nanoparticles also have higher energy in comparison with those of bulk particles and also higher energy than the atoms in the grain boundaries in a nanocrystalline solid. It is believed that the unique structure of nanocrystalline particles offers extraordinary fundamental properties that could be exploited to make '*future generation*' materials [Liz-Marzan et al. (2003)].

There are two main industrial concerns in the use of nanotechnology, (i) the techniques for production of nanomaterials and, (ii) to convert the nanomaterials thus produced into finished products. In order to obtain useful and specific properties and to

control and modify the size, morphology and compositions of nanomaterials, it is crucial to understand their characteristics and properties. Several research groups have developed ways of producing nanomaterials of different types [Shaw (2000), Cushing et al. (2004)], and others have attempted to characterize their properties and combined those properties for certain applications [Dobson (1999)]. The properties which have been characterized are mechanical [Nieh and Wadsworth (1991), Weertman (1993), Liu et al. (1997)], magnetic [Chen et al. (1995), Sato et al. (1997), Ram (2000, 2002)], electrical [Banerjee et al. (2000)], chemical [Koper (1997), Hayashi (1998)], thermal [Johari (1998)], and optical properties [Wakefield (1999)]. In this chapter, the focus is on reviewing the known thermodynamic and related properties and critically examining the merits of these studies. The importance of such a critical review stems from the fact that an understanding of thermodynamic characteristics of nanomaterials is crucial for their manufacture and further processing.

One of the well-known size-dependent thermal properties of nanoparticles is its much lower melting point in comparison with the bulk particles. There have been extensive studies of the melting behaviour of metal nanoparticles by several groups [Takagi (1954), Blackman and Curzon (1959), Blackman, Peppiat and Sambles (1972, 1975), Buffat and Borel (1976), Cotterill and Kristensen (1977), Couchmann and Jesser (1977)] over a long period of time. These groups have used various methods to study the melting behavior of Sn, Pb, Bi, Au, Ag, Ni, etc. by using x-ray diffraction, TEM, HRTEM, etc. However, these indirect methods of observations do not provide information about the heat capacity, enthalpy, and the heat of melting of the nanoparticles.

As mentioned earlier here the factors that cause the properties to become size-dependent are the difference between the surface structure of nanocrystalline and bulk materials, and the much higher ratio of surface area to volume in nanocrystalline than that in the bulk. Therefore, we begin with a description of such differences in the following section.

1.2 Surface Structure and Interfacial Energy of Nanocrystalline Materials

1.2.1 Excess Volume of Nanoparticles

In the bulk crystals, there are two or more layers of surface atoms that are disordered compared to a large volume of atoms that are ordered in its interior. Therefore, the thickness of this disordered layer, δ, compared to the radius of the bulk particle, r, is insignificant. As the size of the particle is reduced to nanoscale, the ratio of disordered layer thickness to radius, δ/r, becomes more and more significant so that the volume fraction of the disordered surface atoms of nanoparticles increases. This is illustrated in figure 1.1.

δ = Thickness of the surface disordered, two to three atoms layer.

r = Radius of a nanoparticle

r_x = Radius of crystalline core
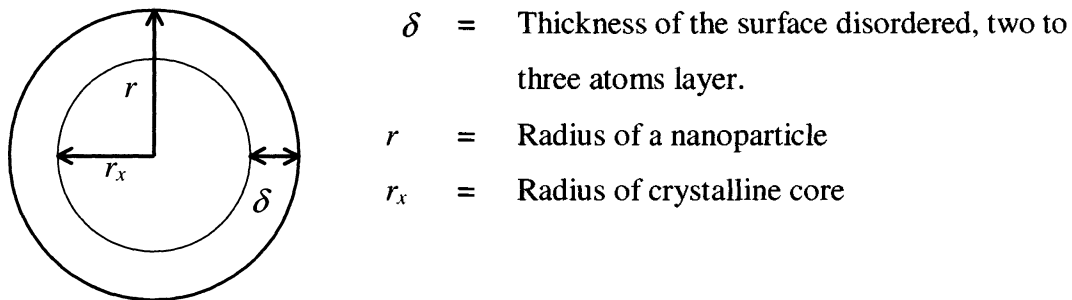
Figure 1.1 An illustration of the surface disordered layer, δ, and crystalline core of nanoparticles, r_x, of a nanoparticle with radius r

The volume of the crystalline core of the particle is given by,

$$V_{crystal} = \frac{4\pi(r-\delta)^3}{3}.$$ (1.1)

Since the total volume of the particle is,

$$V_{total} = \frac{4\pi r^3}{3},$$ (1.2)

the volume fraction of the disordered part in the surface of nanoparticle is:

4

$$X_{surf} = \frac{V_{surf}}{V_{total}} = 1 - \left(1 - \frac{\delta}{r}\right)^3. \tag{1.3}$$

It is clear that when the size of the particle is reduced, δ/r increases, and the volume fraction of the crystalline core, ($1-X_{surf}$), decreases.

According to the law of mixing for an ideal thermodynamic condition,

$$\rho_{nm} = \rho_{bulk} X_{crystal} + \rho_{surf} X_{surf} \tag{1.4}$$

where,

ρ_{nm}	=	Density of nanoparticle
ρ_{bulk}	=	Density of crystalline core region
ρ_{surf}	=	Density of surface disordered region
$X_{crystal}$	=	Volume fraction of crystalline core region
X_{surf}	=	Volume fraction of surface disordered region

It has been known that the surface disordered region has less number of nearest neighbours and a more open structure [Gleiter (2000)] than the crystalline core region. Therefore, its density will be less than the density of the core region, i.e., $\rho_{surf} < \rho_{bulk}$. If it is assumed that $\rho_{surf} = a\rho_{bulk}$, with a as a constant with a value less than one, and if δ, representing the thickness of a two-atom thick surface layers, is substituted by $4r_a$, where r_a is the radius of the atom, Eq. (1.4) may be written as,

$$\rho_{nm}(r) = \rho_{bulk}\left(1 - \frac{4r_a}{r}\right)^3 + a\rho_{bulk}\left(1 - \left(1 - \frac{4r_a}{r}\right)^3\right)$$

$$\rho_{nm}(r) = a\rho_{bulk} + (1-a)\rho_{bulk}\left(1 - \frac{4r_a}{r}\right)^3$$

$$\rho_{nm}(r) = \rho_{bulk}\left(a + (1-a)\left[1 - \frac{4r_a}{r}\right]^3\right). \tag{1.5}$$

For the same mass of bulk particles and nanoparticles, i.e. for $m_{bulk} = m_{nm}$

$$\rho_{bulk}V_{bulk} = \rho_{nm}(r)V_{nm}$$

5

$$\rho_{bulk}V_{bulk} = \left(a + (1-a)\left[1 - \frac{4r_a}{r}\right]^3 \right)\rho_{bulk}V_{nm}$$

$$V_{nm} = \frac{1}{\left(a + (1-a)\left[1 - \frac{4r_a}{r}\right]^3 \right)}V_{bulk} \tag{1.6}$$

The difference between the molar volumes of the nanoparticles and the bulk particle may be written as,

$$\delta V = V_{nm} - V_{bulk} = \left\{ \frac{(1-a)\left(1 - \left[1 - \frac{4r_a}{r}\right]^3\right)}{a + (1-a)\left(1 - \frac{4r_a}{r}\right)^3} \right\}V_{bulk} \tag{1.7}$$

For a bulk particle, the surface layer thickness is almost negligible compared to its particle radius, and therefore $4r_a/r$ value becomes less significant. Thus a value is nearly equal to one and the difference between the molar volumes of the bulk and nanoparticles vanishes.

1.2.2 Structure and Surface Energy Relationship

It has been known that the high surface to volume ratio of nanoparticles affects all its properties. In their thermodynamic behaviour, the most observable is the decrease in the melting point. Chalmers (1982) has reviewed this subject and has concluded that there are two explanations for this decrease.

The first is the large surface area relative to its volume when a crystal or particle is extremely small. Interfacial energy is added to the Gibbs energy, G, and in general the change in G with change in the pressure, P, temperature, T, chemical composition, n, and the surface area, A, is given by,

$$dG = -SdT + VdP + \sum \mu_i dn_i + \gamma dA. \tag{1.8}$$

6

Therefore, for a pure material considered here, $\mu_i\,dn_i$ term is zero and for a given P and T conditions, the γdA term in Eq. (1.8), which is now equal to dG, becomes increasingly important as the surface area per unit molar volume increases. This term bodily shifts the G against T curve of the nanoparticles upwards relative to the bulk solid, by an amount γA. Thus the G against T curve for the nanoparticles crosses the G against T curve for the bulk liquid at a lower temperature. At the melting point of the bulk particles, the nanoparticles have a higher G value than the bulk liquid.

We now consider the enthalpy difference between the bulk and nanoparticles. Since enthalpy, H, is given by the $C_p\,dT$ integral, and C_p decreases with decrease in the temperature for both the liquid and the crystal phase, but more for the liquid than for the crystal, it follows that the enthalpy increase on melting of a nanomaterial at its equilibrium melting point would be less than the enthalpy increase on melting of a bulk material at its equilibrium melting point. In brief, the enthalpy of melting decreases with decrease in the size of the particle.

These two aspects have been illustrated in figure.1.2. In Fig. 1.2 (a) the variation of G with temperature is given and in Fig 1.2 (b) the variation of H is given. In the next section it will be shown that C_p of nanoparticles is higher than that of the bulk particles and therefore the enthalpy of melting would further decrease.

(a)

(b)
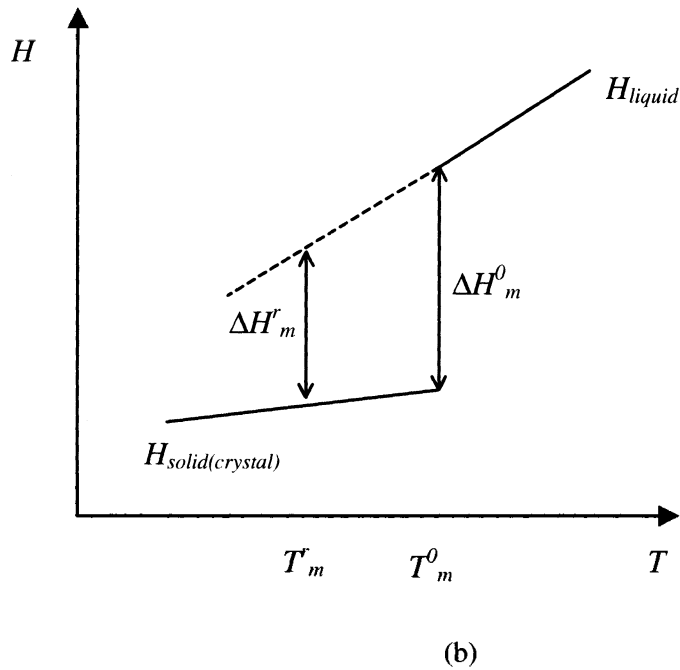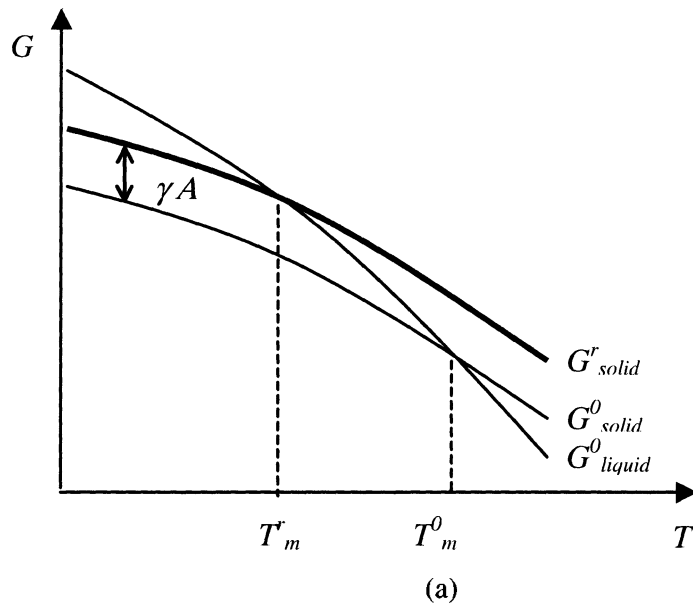
Figure 1.2 (a) An illustration for G against T of liquid, bulk crystal and nanocrystal. It shows that the contribution of nanoparticles to the total surface area shifts the solid-liquid transformation temperature to lower temperature than T^0_m (b) The resulting decrease in the enthalpy of melting. The superscript 0 corresponds to the standard value for the bulk phase and superscript r to nanoparticles

8

The second explanation given by Chalmers (1982) is that at a solid-liquid equilibrium, the rate of transfer of surface atoms to the melt at a given temperature is higher for extremely small particle or crystal than for the bulk particle or crystal. To elaborate, for a polycrystal with very small crystallites, a relatively high proportion of atoms resides on the grain boundaries and for single crystal particles on the free surfaces [Gleiter (2000)]. These surface atoms are more weakly bonded to the crystal than those in the core of the particles or grains because they have lesser nearest neighbours than those in the core. Specifically, as Wang et al. (2002) has stated, the surface or interface atoms have less nearest neighbours and weaker binding, and thus have higher interatomic forces due to the presence of dangling bonds than the core atoms, which are in a state of equilibrium forces with their neighbours. The smaller the size of the particles, the larger is the deviation from the equilibrium, so that according to the interatomic potential function, the asymmetric forces of these atoms increase and give rise to the surface energy of the particles. At a given temperature, the rate of transfer of atoms from the surface to the melt is therefore higher for the very small crystallites or particles than for the larger ones, while the rate of transfer of atoms from the melt to the surface is not affected. The temperature at which the two rates are equal is therefore lower for a small crystal or particle than for a larger one. Therefore the kinetics of atomic transfer is determined by the size of the crystallites.

An explanation similar to the one given above has been mentioned by Wang et al. (2002). They have suggested that a large surface-to-volume ratio, as discussed above, and an (undefined) quantum confinement effect in finite-size systems are responsible for the different melting behaviour of the nanoparticles relative to the bulk particles.

Similar explanation in the perspective of cohesive forces has also been used by Nanda et al. (2003). In the core of the crystallites and particles, interatomic distances are the same and the cohesive forces between the atoms tend to balance. But on the surface, there are atoms on only one side and not on the other, which causes a net inward cohesive force. As the particle size decreases, the net inward cohesive force increase results in an increase of the surface free energy. It is also mentioned that the surface energy of free

nanoparticles is higher than that of crystallites since the net inward forces are reduced by the presence of a matrix. As an example of the fact that surface energy, γ, for bulk particles is less than that for embedded nanoparticles, which in turn is less than that of the free nanoparticles, a list of several materials is presented in Table 1.1. Nanda et al. (2003) have mentioned that only Pd nanoparticles were embedded in polymer matrix, but it was not clear whether other particles were embedded in the same or a different matrix.

Table 1.1 List of the surface energy, γ, of the free and embedded nanoparticles and of the bulk

Material	γ of free nanoparticles (J/m^2)	γ of embedded or capped nanoparticles (J/m^2)	γ of bulk (J/m^2)
Ag	**7.9** [Nanda et al. (2003)] **6.4** [Berry (1952), Wasserman et al. (1970), Hofmeister et al. (1997, a)]	**1.3-5.9** [Planta et al. (1964), Montano et al. (1984), Hofmeister et al. (1997 a, b)]	**1.065-1.54**
Pd	--	**6.0 ± 0.9** (embedded in polymer matrix)	**1.808**
CdS	**2.50**	**1.74**	**0.75**
PbS	**2.45** [Nanda et al. (2002, a)]	--	**0.0383** [Janczuk (1994)] **1.4** [calculated by Nanda et al. (2002, b)]

1.2.3 Size-dependent Melting of Nanocrystalline Particles

Although melting is a common phenomenon, a general theory for this phase transformation has neither been established nor fully understood especially for nanoparticles [Zhong et al. (2001)]. Several explanations of melting behaviour reviewed in the introduction section of an article by Zhong et al. (2001) are:

- Lindemann (1910) has stated that melting is a vibrational instability that appears when the root mean square amplitude of vibration reaches a critical fraction of the interatomic distance depending on the size and shape of material,

- Kuhlmann- Wilsdorf (1965) and Cotterill (1980) have explained melting in terms of increase in dislocation generation,

- Górecki (1974, 1976) has emphasized vacancies as a crucial factor during melting, and

- Boyer (1985) has concluded that lattice shear instability is the precipitating feature for melting.

In order to explain melting behaviour of nanoparticles, extensive recent research has focused on their melting behaviour and modeling its size dependency. These studies have shown that mechanism of melting of nanoparticles is different from that of bulk particles described earlier by Kuhlmann-Wilsdorf in 1965. According to her theory, melting occurs as a result of increasing formation of dislocation cores with increasing temperature. The concentration of dislocation cores increases to a value at which a material can no longer sustain its shape. The temperature at which this value is reached is defined as the melting point of a material. From this perspective, Kuhlmann-Wilsdorf theory, that melting process begins from inside of the particle outwards, contrasts that of melting on nanoparticles, whose melting is found to initiate from the surface of the particles and proceeds inwards [Couchmann and Jesser (1977), Goldstein et al. (1992), Schmidt (1997)].

Johari (1998) has presented a comprehensive review of melting in terms of thermodynamics, and of the theories developed to explain the size-dependent melting

behaviour of nanoparticles. According to his review, several series of experimental observations and mathematical modeling of the size-dependent melting behaviour of nanoparticles had been performed by:

(a) Pawlow (1908, 1909) has derived an equation for the triple point at which spherical solid and liquid particles of equal mass were in equilibrium with a common vapour. Pawlow's theory was then extended by Hanszen (1960), who has showed that the depression of melting point of a given material is inversely proportional to the particle radius according to:

$$T_0 - T_P = \frac{2T_0}{\Delta H_f \rho_S} \left\{ \gamma_S - \left(\frac{\rho_S}{\rho_L} \right)^{2/3} \gamma_L \right\} \frac{1}{r} , \qquad (1.9)$$

where T_0 and T_P are the bulk temperature and the small particle melting temperature defined by Pawlow respectively. ΔH_f is the molar heat of fusion; r is the radius of the particle; ρ_S, ρ_L are the molar density of solid and liquid respectively, and γ_S and γ_L are the surface energy of solid and liquid respectively.

(b) Reiss and Wilson (1948) have suggested that pre-melting of nanoparticles is caused by formation of liquid skin whose surface energy gives a large contribution to the total free energy of nanoparticles. They defined melting temperature as the temperature at which movement of the liquid-solid interface into the particle is energetically favourable. Wronski (1967) has extended Reiss and Wilson's theory by assuming that the liquid skin formed is several atoms thick, thus causing the decrease in melting point to occur more rapidly than the increase in reciprocal particle radius. Therefore, melting point decrease does not depend linearly on $1/r$ according to:

$$T_0 - T_P = \frac{2T_0}{\Delta H_f \rho_S} \left\{ \frac{\gamma_{S.L}}{r-t} + \left(1 - \frac{\rho_S}{\rho_L} \right) \frac{\gamma_L}{r} \right\} \qquad (1.10)$$

where t is the critical thickness of liquid skin in thermodynamic equilibrium with the solid core.

(c) Mieko Takagi (1954) has studied melting points of Bi, Sn and Pb thin films (10-1000 Å) by electron diffraction technique. She found that the melting point decrease was inversely proportional to the particle radius.

(d) Coombes (1972) and Peppiat and Sambles (1975) have performed further experiments on melting of nanoparticles and have confirmed the liquid skin thickness formation of Pb at the equilibrium melting temperature.

(e) Buffat and Borel (1975) have studied melting of Au nanoparticles by using electron microscopy. Based on their observations, they have modified Wronski and Coombes equations for melting behaviour of gold nanoparticles. They have also reported that Au particles of 2 nm size melt at 600 K, much lower than 1336 K, the bulk melting point of Au.

(f) Couchmann and Jesser (1977) have re-derived an equation for the size-dependent melting point by introducing the effect of the thickness of liquid skin melting formed near the melting point of nanoparticles to the Gibbs-Thomson equation. They modified the term $1/r$ to $1/(r-t)$ in Gibbs-Thomson equation, where t is the thickness of liquid skin,

$$T_0 - T_P = \frac{2T_0 \gamma_{S.L}}{\Delta H_f \rho_S} \frac{1}{r-t} .$$

(1.11)

In his review article, Johari has also explained the mechanism of pre-melting phenomenon of polycrystalline solids, which may occur in two ways:

- firstly small particles melt as a whole and the larger particles at the grain junctions,

- secondly small particles melt at the surface as well as at their grain junctions and the large particles melt only at the grain junctions.

To conclude, the models describing the melting behaviour of small particles can be classified into [Peters, Cohen and Chung (1998)]:

(a) Homogenous melting model without a liquid skin [Pawlow (1909), Buffat and Borell (1976)],

(b) Liquid-skin melting model [Reiss and Wilson (1948), Hanszen (1960), Wronski (1967)]

13

(c) Liquid nucleation and growth model with an unstable liquid skin [Couchman and Jesser (1977), Skripov et al. (1981), Reiss et al. (1988), Vanfleet and Mochel (1995)].

There have also been a number of computer simulation and experimental studies of surface melting behaviour of small particles during the last decade, as summarized below:

(a) Molecular dynamics simulation for clusters of 40-147 atoms has been performed by Cheng and Berry (1992). They have concluded that surface melting is associated not with amorphous, random surface structures in constant, irregular motion, but rather with large-amplitude, organized, collective motion of most of the surface atoms accompanied by a few detached atoms and holes.

(b) Surface melting of free nanoparticles caused by curvature effects has been studied by Kofman and Lereah et al. (1994). They have suggested that surface melting occurs gradually until the particle radius reaches a critical size at which surface melting disappears and discontinuous melting occurs, in other words particles melt wholly.

(c) Surface-induced melting of small particles has been studied by Sakai (1996). Based on Landau theory [Landau (1944)] he has shown that there is a non-linear relationship between the melting point and reciprocal radius of the particle, which is derived from a difference between the radius dependence of surface-induced melting temperature and that of bulk melting temperature. In contrast to the common-belief that surface melting becomes more dominant for smaller particles, according to Sakai, it becomes more difficult as a particle radius decreases down to the critical value.

(d) Solid-liquid phase transition in nanoparticles contacting with a solid surface has been studied by Storozhev (1998). Using computer modeling within thermodynamic framework, he has found that presence of substrate affects the melting process of small particles. If the contact angle between the liquid adsorbate and substrate is close to 180°, the interaction between them is weak. Thus the measured melting temperature should be higher than that of the bulk. The melting point decreases as the contact angle between the solid substrate and the liquid adsorbate decreases.

Further molecular dynamic simulations of 13-3871 atoms by Zhao et al. (2001) have shown that there are not only two well-known mechanisms of surface and core melting [Kofman and Lereah et al. (1994,1999), Dippel et al. (2001) and Kimberly et al. (2002)], but also an intermediate mechanism between the two. Accordingly, the three distinctive melting mechanisms for isolated nanoparticles are:

(1) Surface pre-melting [Wronski (1967), Kofman and Lereah et al. (1994, 1999), Sakai (1996)] which occurs for particles containing 258-3871 atoms.

(2) Intermediate melting in which the depression of melting point is very slow while the latent heat of melting is greatly enhanced. This occurs for particles containing ~120-240 atoms.

(3) Dynamic coexistence melting in which transition from low energy (solid-like) to high energy (liquid-like) structure occurs spontaneously. This occurs for particles containing 13-116 atoms.

The above given review has described the relation between structure, surface energy and melting temperature of nanoparticles as well as the mathematical models used to explain the melting. In the next section, we review the effect of small particle size on the heat capacity, and finally on the inversion of phase transformation in nanocrystalline solids.

1.2.4 The Heat Capacity of Nanocrystalline Materials

The heat capacity of nanocrystalline materials was studied first by Gleiter et al. (1986). They found that C_p of nanocrystalline Pd at 295 K is ~ 50 % higher than that of its bulk polycrystalline solid. Similar studies of the increase in heat capacity were performed by Rupp and Birringer (1987) on nano-grained and coarse-grained Pd and Cu. They found that C_p of nanocrystalline Cu is 10% higher than that of its coarse polycrystalline, and C_p of nanocrystalline Pd is 40% higher than that of its coarse polycrystalline state. They have concluded that nanocrystalline materials consist of two components with comparable volume fractions, namely a core crystalline component comprising all atoms located in the lattice of the crystallites or grains and an interfacial component formed by all atoms situated in the interfaces or grain boundaries.

Based on these studies, the higher heat capacity and higher thermal expansion coefficient of nanoparticles has been attributed to, (i) the presence of a large fraction of atoms in the disordered interfacial structure. The lower relative density of nanocrystalline materials (~ 85 % of the bulk density) implies a more open structure of the grain-boundary component, and hence a weaker interatomic coupling. This decreases the vibrational frequencies and increases the vibrational and configurational entropy [Gleiter (1986)], (ii) thermally induced variation of the vibrational and configurational entropy of the materials due to lattice vibrations and variation of equilibrium defect concentration, especially in the disordered structures (grain boundaries) [Rupp and Birringer (1987)], and (iii) strong anharmonic forces that lower the vibrational frequencies due to different interatomic spacings [Schaeffer and Würschum (1988)].

There have also been several other studies of the heat capacity of nanocrystalline materials and these have been compared with amorphous and coarse-grained polycrystalline materials. Sun and Lu (1996) have compared the heat capacities of nanocrystalline, amorphous and coarse-grained polycrystalline states of Se. They have found that the nanocrystalline Se has 2% higher heat capacity than coarse-grained polycrystalline Se.

16

Zhang and Banfield (1998) have developed a model for describing the increase in the heat capacity of nanocrystals over the bulk phase by using the Einstein and Debye vibration modes. Borg et al. (1992) have discussed this increase by considering the differences in vibration modes between surface atoms and interior atoms of the solid particle. Calculations using this model were performed for silver and rutile, TiO_2.

In 2002, Shrivastava modeled the heat capacity of nanocrystals, namely nanoferromagnets, based on the theory of phonon scattering by the boundary of nanocrystals. This scattering generates new phonon frequencies, which contribute to the heat capacity. He has concluded that since the Debye T^3 law would not be applicable in the presence of additional contribution of spin-waves scattered by the surface of the nanocrystal, the low temperature heat capacity is instead expected to vary exponentially with both temperature and particle size.

In summary, the disordered surface atoms on nanoparticles have different modes of atomic motion resulting in different vibrational and configurational entropy contribution. In their study of free energy of active atoms in grain boundaries of nanocrystalline copper, nickel and palladium, Kirchheim et al. (1992) have indeed calculated the configurational entropy of the grain boundaries for the three metals at 330 K. They have shown that the configurational entropy of the grain boundary atoms of nanocrystalline (aggregate) metals are much higher than the corresponding entropy typical of coarse polycrystalline metals. For example, the configurational entropy of grain boundaries of Ni-coarse polycrystals is 8.314 J mol^{-1} K^{-1}, while that of Ni-nanocrystals of 12 nm diameter is 71.5 J mol^{-1} K^{-1}. They have also concluded that this may be due to grain boundaries having a large excess volume.

The variation in the vibrational and configurational contribution of these atoms has a further effect not only on the increase in heat capacity, but also on the increase in thermal expansion. Besides the increase in heat capacity, Rupp and Birringer (1987) mentioned that there is an increase in thermal expansion coefficient from 16×10^{-6} K^{-1} for coarse crystalline Cu to 31×10^{-6} K^{-1} for nanometer-size crystalline Cu aggregate. Similar results obtained by Lu et al. (1992) have shown that the thermal expansion

coefficient of the nanocrystalline Ni-P alloy is 21.6×10^{-6} K^{-1}, which is higher than that of the as-cast Ni-P crystalline alloy, 13.7×10^{-6} K^{-1}, by about 56 %.

1.2.5 Size-dependent Phase Stability Inversion of Materials

Bulk metastable phase becomes the stable phase when size is reduced to nanometer scale without changing the temperature or pressure. This phenomenon is named as a phase stability inversion.

Rao and Rao (1978) originally suggested that thermodynamic stability of polymorphs is determined by their particle size, surface area, and the presence of impurities or vacancies. The presence of high surface area of nano-sized particles stabilizes the metastable, higher temperature phase at ambient temperature. One example given is that of a ceramic tetragonal ZrO_2, which is usually formed at 1420 K, is stabilized at room temperature by reducing its particle size. However, they did not mention its critical size. Our literature survey showed that several polymorphic materials undergo phase stability inversion when their size is decreased to nanometer-scale. Some of these are listed in Table 1.2.

Table 1.2 Materials that undergo phase stability inversion at nanoscale size and the inversion temperature

Stable Bulk Phase	Metastable Bulk Phase	r_c (nm)	T (K)	Source
α- Al_2O_3 (2.04 J/m^2)	γ- Al_2O_3 (0.79 J/m^2)	7.5	800	McHale et al. (1997)
Rutile - TiO_2 (1.93 J/m^2)	Anatase - TiO_2 (1.34 J/m^2)	7	298	Zhang and Bainfield (1998)
HCP (α) Co (2.79 J/m^2)	FCC (β) Co (2.73 J/m^2)	10	293	Sato et al. (1997) and S. Ram (2001)
Monoclinic ZrO_2	Tetragonal ZrO_2	9	298	Chraska et al. (2000)
α- Fe	γ- Fe	25	300	Meng et al. (2002)
Hexagonal ice	Cubic ice	15	160-220	Johari (2005)

As described in section 1.2, the decrease in particle size to nanometer scale causes the total free energy to increase due to the large surface energy contribution. In materials that exist as polymorphs, a solid-solid phase transformation may occur at a fixed temperature and pressure due to the increase in net free energy resulting from reduction of particle size. This is illustrated in figure 1.3.

When a metastable phase has lower surface energy compared to the stable phase ($\gamma_\beta < \gamma_\alpha$), the increase in specific surface area will contribute less to the increase of Gibbs free energy. The slope of Gibbs free energy, G, to $1/r$ for the α-phase would be higher than that for the β-phase. As particle radius is decreased, G_α increases faster than G_β and at a certain r value, which is defined as r_c, $G_\alpha = G_\beta$, α and β phases coexist. If the particle radius is further reduced below r_c, α-phase, the stable bulk phase exists in a higher energy state than β-phase, the metastable bulk phase. As the system lowers its energy spontaneously, the phase transformation from α-phase to β-phase occurs at lower temperature. Therefore the phase stability inversion, where the metastable bulk phase becomes the stable phase in nanoscale size, can be explained through a decrease in total surface energy.

Chraska et al. (2000) have proposed this size induced phase inversion in terms of the free energy of an unconstrained spherical particle, G,

$$G = \frac{4\pi r^3}{3}G_v + 4\pi r^2 \gamma \qquad (1.12)$$

where r is the radius of a particle, G_v is the free energy per unit volume of an infinite crystal, and γ is the surface energy of the crystal. The difference in the free energy of two polymorphs is then given by,

$$\Delta G(r) = \frac{4\pi r^3}{3}\Delta G_v + 4\pi r^2 (\gamma_\beta - \gamma_\alpha) \qquad (1.13)$$

where ΔG_v is the free energy difference for the phase transition per unit volume of an infinite size crystal.

19
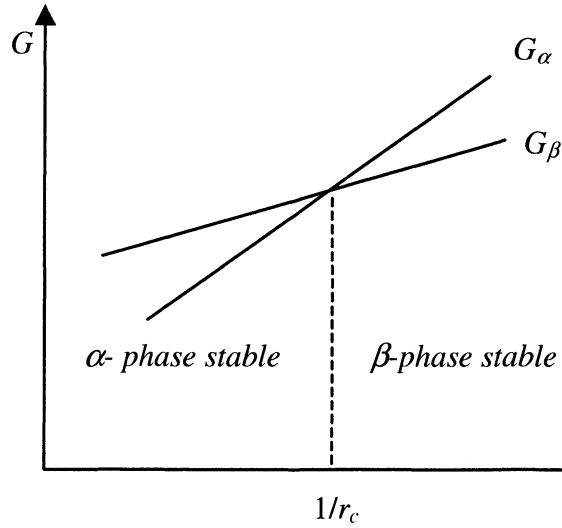
Figure 1.3 An illustration of the total free energy, G, as a function of $1/r$, for α and β phases of a material. At constant P and T, the decrease in particle size reverses the stability of the polymorphic phases. Particles with $r > r_c$ are stable in α-phase and those with $r < r_c$ are stable in the β-phase. At r_c the two phases are in equilibrium

Assuming that the β-phase has lower surface energy than the α-phase of a material, as the particle is reduced to some critical value, r_c, where $\Delta G(r_c)$ is zero at a given temperature, T, the metastable β-phase can exist below the normal transformation temperature. The critical radius would then be written as [Chraska (2000)],

$$r_c = \frac{-3(\gamma_\beta - \gamma_\alpha)}{\Delta H\left(1 - \frac{T}{T_t}\right)}$$

(1.14)

where ΔH is the heat of transformation per unit volume and T_t the transformation temperature of an infinite size crystal.

Johari (2005) has provided equations for calculating the critical dimension for both spherical and plate-shaped crystals' phase stability inversion and these equations are:

$$r_c = \frac{-3V_m(\gamma_\alpha - \gamma_\beta)}{\Delta H_{\alpha \to \beta}}$$

(1.15)

20

for spherical crystals, and

$$\delta_c = \frac{-2V_m(\gamma_\alpha - \gamma_\beta)}{\Delta H_{\alpha \rightarrow \beta}}$$

(1.16)

for plate-shaped crystals, where r and δ are the radius and thickness of the crystals respectively, and V_m the molar volume.

We concluded that thermodynamically, the change in the particle size below certain r_c modifies the structure and morphology of a stable bulk phase. As a particle size is decreased to sufficiently low value, the total free energy of bulk phase is higher than that of metastable phase. This phase inversion would vanish if the nano-scale particles are heated, coarsen, and returned to bulk size and thus to bulk stable phase.

Chapter 2. Thermodynamics of Melting of Nanoparticles and Bulk Zinc

2.1 Introduction

In view of the importance of more comprehensive understanding of the melting behaviour of nanoparticles, this research is focused on observing the thermodynamics of melting of pure free and confined nanocrystalline particles, especially in terms of melting point, enthalpy of fusion and heat capacity in comparison with the bulk crystals. For this purpose zinc metal was chosen for the study.

Differential Scanning Calorimetry has been used extensively to study experimentally the melting behaviour of materials dispersed as nanoparticles, including zinc [Wu et al. (1998, 2000a & b, 2002, 2004), Narayan et al. (2002)], tin and aluminum [Lai et al. (1996, 1998)], selenium [Sun and Lu (1996)], paladium and copper [Rupp and Birringer (1987)], indium [Sheng et al. (1996)] metal; CuI [Kumar et al. (2001)] and NiMo [Oleszak et al. (1999)] alloy; and pharmaceutical nanoparticles [Bergese et al. (2004)]. This has led to direct observations on the details of melting process by monitoring the heat involved during the process.

It is well known that zinc is widely used in galvanizing steel products to enhance their surface corrosion resistance, in alloying with other metals such as brass, and a lot of other uses have been found for zinc. Accordingly, ZnO also has as wide applications as zinc, such as (i) absorbent for ultraviolet radiations in sunscreen, as at a nanoparticle scale ZnO provide a wide range of energy band gap that can absorb ultraviolet radiations with less scattering preventing the whitening effect on the skin. [www.lorealusa.com (2004)] (ii) electro-optic and piezoelectric material [Puchert et al. (1996), Gupta et al. (2002)] (iii) as a catalyst for accelerating the adsorption of gases on gas sensor materials of other kinds [Dachun et al. (1997), Gupta et al. (2002)], and in the production of the n-type Metal Oxide Semiconductor sensor itself for the detection of CO, H_2, and NO_2 [Lin

et al.(1998)], (iv) as a wear resistance, shock resistance, sound insulation, photosensitization, fluorescence, and catalytic material in the form of tetrapod-shape nanocrystals [Wu et al. (2000)]

Because of their technical applications, research on both Zn and ZnO has been focused on their useful properties by characterizing the crystal structure of the nanoparticles and the relationship between structure and properties, yet not on thermodynamics of their nanoparticles. Wu et al. (1998, 2000 a & b, 2002, 2004) have provided a brief discussion on thermal properties of Zn and ZnO, but not on their thermodynamics.

Since this thesis is concerned only with zinc and zinc oxide that formed on the surface of nanoparticles, we discuss their known properties in the following section.

2.1.1 Physical and Thermodynamic Properties of Zinc Metal and ZnO

A detailed description of physical properties of zinc and zinc oxide has been provided by Matthewson (1959) and www.webelements.com (2004). It is presented in Table 2.1. The comparison between these physical properties of zinc and zinc oxide will later be shown to significantly affect the evolution of zinc nanoparticles on both heating and cooling, especially their crystal structure and orientation, thermal expansion coefficient, and modulus of elasticity.

A study of thermodynamic properties of bulk zinc was recently reported by Grønvold and Stølen (1999, 2003). Loss (2001) has re-determined the atomic weight of zinc as 65.409 Dalton at 692.68 K. Grønvold and Stølen (1999, 2003) have determined thermodynamic properties from measurement by using a high-temperature adiabatic calorimeter in temperature range 300-900 K. They have provided the following values:

$$\Delta H_{0\,K}^{298.15\,K} \quad = \ 5663 \text{ J mole}^{-1}$$

$$\Delta S_{0\,K}^{298.15\,K} \quad = \ 41.64 \text{ J K}^{-1} \text{ mole}^{-1}$$

$$\Delta H_{\text{melting}}^{692.68\,K} \quad = \ 7070 \text{ J mole}^{-1}$$

A complete list of the measured heat capacities of solid and liquid zinc and their other thermodynamic properties are presented in Appendix A.

Table 2.1 Physical properties of Zinc and Zinc Oxide

Properties	Zn	ZnO
Crystal Structure and Orientation	Hexagonal Close Packed , a = 2.665 Å, c = 4.947 Å, c/a = 1.856 Glide Plane (0001); glide direction [11$\bar{2}$0] Twinning Plane (10$\bar{1}$2)	Hexagonal Wurtzite , a = 3.250 Å, c = 5.207 Å No preferred orientation
Atomic Sizes	Metallic radius (12-coordinated), 1.38 Å Tetrahedral covalent radius, 1.31 Å Ionic radius (Zn^{++}), 0.74 Å	
Density	Solid at 298.15 K, 7.133 g cm^{-3} Solid at 692.65 K, 6.83 g cm^{-3} Liquid at 692.65 K, 6.62 g cm^{-3} Liquid at 1073.15 K, 6.25 g cm^{-3}	Solid, 5.6 g cm^{-3}
Heat Capacity	Solid - C_p = 22.38 + (10.04 × 10^{-3} T) J K^{-1} mol^{-1} for T 298 - 692.7 K Liquid - C_p = 31.38 J K^{-1} mole^{-1}	Solid - C_p = 49 + (5.1 × 10^{-3} T) – (9.12 × 10^{-5} T^2) J K^{-1} mole^{-1} for T 298 - 2248 K
Linear Coefficient of Thermal Expansion	Polycrystalline (293.15 - 523.15 K), 39.7 × 10^{-6} K^{-1} a-axis (293.15 -373.15 K), 14.3 × 10^{-6} K^{-1} c-axis (293.15 - 373.15 K), 60.8 × 10^{-6} K^{-1}	4 × 10^{-6} K^{-1} [Wu et al. (2000)]
Volume Coefficient of Thermal Expansion	(293.15 - 373.15 K), 8.9 × 10^{-5} K^{-1}	
Thermal Conductivity	Solid at 291.15 K, 112.97 watts m^{-1} K^{-1} Solid at 692.15 K, 96.23 watts m^{-1} K^{-1} Liquid at 692.15 K, 60.67 watts m^{-1} K^{-1} Liquid at 1023.15 K, 56.48 watts m^{-1} K^{-1}	
Modulus of elasticity	Solid - Zn, 70 - 140 GPa	Solid - ZnO, 210 GPa [Kittel (1996)]

2.2 Experimental Methods

2.2.1 Bulk and Nanoparticle Zinc

Nanocrystalline particles of zinc were purchased from Nanostructured and Amorphous Materials Inc. Its purity was 99.9 + %, the average particle size had been determined by XRD and TEM method by the supplier. It was stated to be in the 35-80 nm range, with no specification of their size distribution, and the specific surface area was stated as 30-50 m^2/g. It had been supplied in the form of dry powder, contained in a hermetically sealed plastic container. The container was opened in a glove box containing high purity Argon gas and small stocks of zinc nanoparticles were then stored in several sealed glass vials. These were kept in a dessicator until the measurements were performed.

Bulk zinc metal was purchased in the form of "metal shots" of > 99.9 % purity from Fischer Scientific Company.

2.2.2 Transmission Electron Microscopy (TEM)

2.2.2.1 <u>TEM Sample Preparation</u>

First the shape and particle size distribution of the zinc nanoparticles was studied by TEM. For this purpose, a JEOL 2010F TEM/STEM and a Philips CM12 TEM with specimen holder equipped with molybdenum-heating filament were used for direct observation of the melting of nanocrystalline particles. Zinc nanocrystals were firstly dispersed in toluene, a non-polar organic solvent, in order to reduce their reactivity and flammability with moist air. A drop of very dilute dispersion of the nanoparticles was then put onto the Cu grid carbon thin film and left in open air to allow the solvent to evaporate.

2.2.2.2 Basic Theory of Energy-Filtering TEM (EFTEM) and Scanning TEM

The basic principle of EFTEM and STEM is similar to that of TEM, which is based on the interaction between electrons generated by microscope probe, the so called primary electrons, and electrons in the sample. The primary electrons generated through heating of the tungsten filament are accelerated through an electric field of 20 to 120 keV range. These electrons hit the specimen and interact with electrons in the specimen. The electrons transmitted out of the specimen are then captured and recorded as an image.

In ordinary TEM, the recorded image is constructed from both the elastically and inelastically scattered electrons contained in the transmitted electrons. The elastically scattered electrons are those which are deflected electrostatically by the atomic nuclei and by the surrounding electrons during travel through the specimen, and thus these electrons have negligible change in energy. The inelastically scattered electrons are those which are scattered by the core electrons, involving both momentum transfer and energy losses. By using the zero-loss filtering techniques in EFTEM, the inelastically scattered electrons, which cause blurring of the image, can be removed so that contrast enhancement and sharper image or higher resolution can be attained.

The basic mechanism for EFTEM zero-loss filter imaging is shown in figure 2.1. The transmitted electrons coming out of the illuminated sample are filtered by the energy slit, which removes all inelastically scattered electrons. Thus the transmitted electrons captured in the image contain only the elastically scattered electrons and give a zero-loss filtered image with better contrast and resolution.
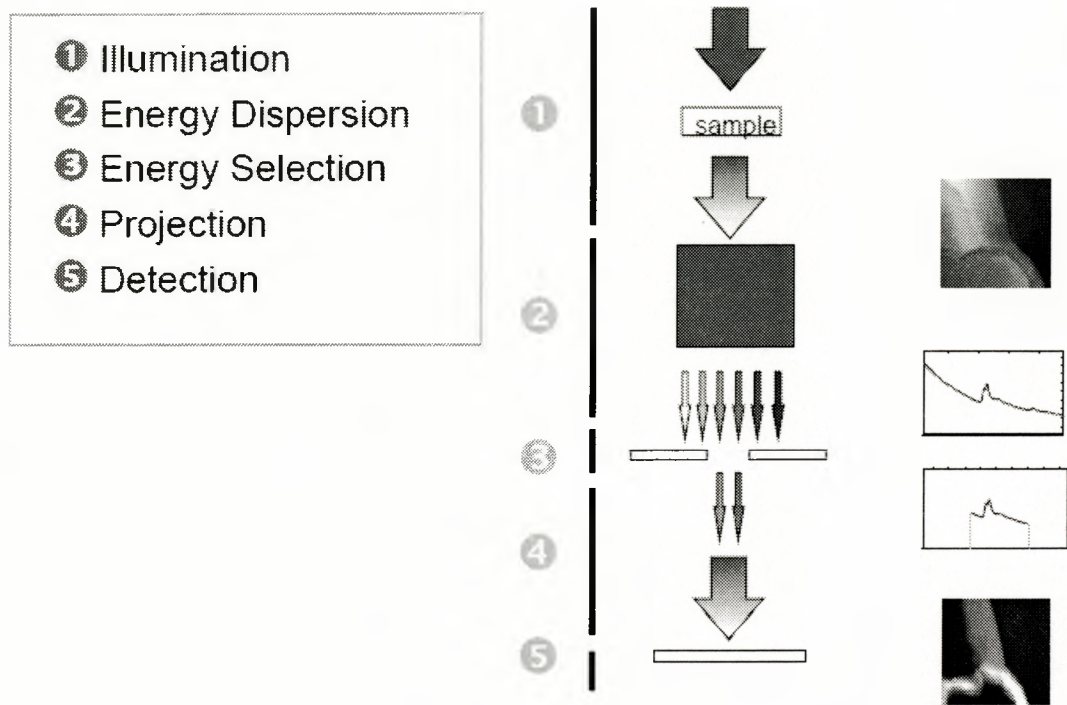
Figure 2.1 The sequence of the zero-loss filtering processes in EFTEM

One step further, this technique can also be used for the qualitative and quantitative elemental distribution image by generating elemental map, either by using EFTEM Spectrum Imaging or STEM Spectrum Imaging. The only difference between EFTEM and STEM is in the manner they obtain the spectra as depicted in figure 2.2(a) and (b). The two horizontal axes correspond to the x-y position on the specimen and the third, vertical axis contains the energy-loss information. In EFTEM Spectrum Imaging, the entire x-y plane of the specimen is investigated at once by parallel electron illumination (fixed electron beam) and the acquisition is repeated at a number of separate energy-loss settings (plane by plane). In contrast, in STEM Spectrum Imaging, the electron beam is focused on one pixel of the specimen. The focused electrons scan the x-y plane pixel by pixel, during which the energy-loss spectrum is sequentially recorded. This makes processing time of STEM longer than that of EFTEM.

28
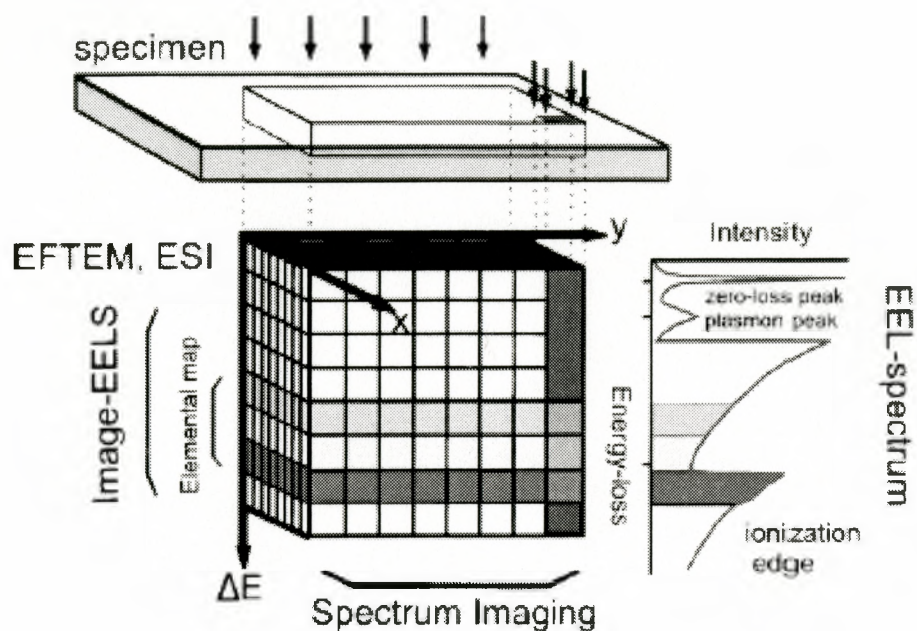
(a)
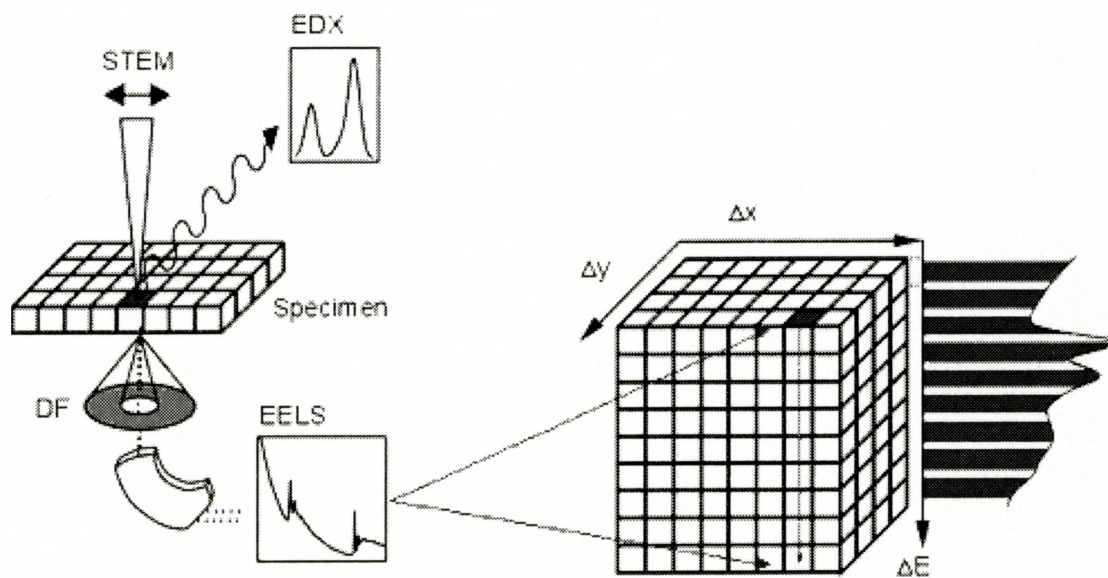
(b)

Figure 2.2 (a) EFTEM spectra collection is obtained using parallel illumination of electron plane by plane and **(b)** STEM spectra collection is obtained by focused illumination of electron pixel by pixel [Hofer et al. (2000), www.gatan.com/analysis/eftem_stem.html]

In EFTEM, a three-window technique is usually used for generating elemental maps. The principle is that the obtained spectra are filtered using an energy slit, also called a window, of 20 to 50 eV width, whose position depends on the edge of the element. The edge of the element is known from previously obtained Electron Energy Loss spectra. Two of the three windows are placed before the edge and the other window after the edge, as schematically shown in figure 2.3. The images of the two pre-edge windows and the post edge window are then recorded. The intensities of two pre-edge images are extrapolated to obtain the background intensity from which the intensity of post-edge image is subtracted and finally the net intensity is obtained. This net intensity image, the so called elemental map, depicts the distribution of the element in the sample. The intensity-based quantitative analysis can also be performed so that we can quantify the amount of the element present in certain areas of the sample.
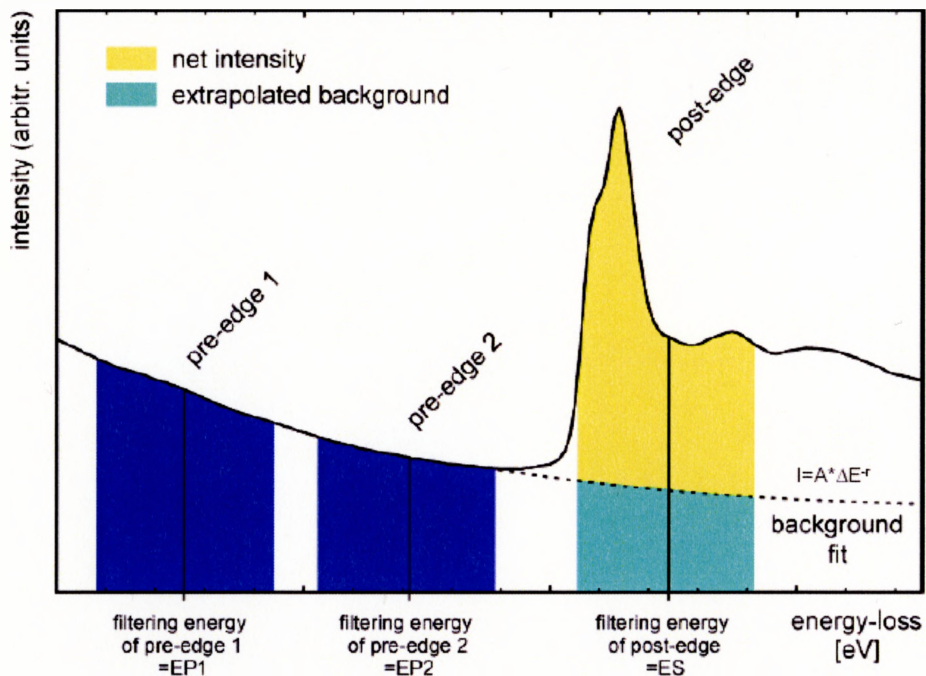
Figure 2.3 Schematic description of three-window method in EFTEM that is used for obtaining elemental maps. The total net intensity of the element is the post-edge intensity subtracted by the extrapolated background intensity from pre-edge 1 and pre-edge 2 intensities (Gerald Kothleitner, Felmi TU Graz, 2003)

2.2.3 Differential Scanning Calorimetry

2.2.3.1 <u>Basic Theory of DSC</u>

Two calorimeters were used for this study: one was a Perkin-Elmer Pyris Diamond Calorimeter and the second was a Thermal Analysis Q-100 assembly. The purging gas used for the former was high purity argon, while for the latter was high purity nitrogen. Both calorimeters were calibrated against the melting point and melting enthalpy of indium. Each instrument was equipped with data analysis software that allowed calculation of the enthalpy and heat capacity of the samples. Further data analysis was performed using Microcal Origin Software.

In the Perkin Elmer Pyris Diamond Calorimeter, the sample holder and the reference holder are each provided with individual heaters and thermometers as illustrated in figure 2.4(a), which enables the use of 'null-balance' or zero difference principle in the measurements. The temperature of the reference sample is then increased, or decreased, at pre-determined rates, which is continuously recorded. If a temperature difference develops between the sample and reference because of exothermic or endothermic effect in the sample, the feedback built into the instrument adds or subtracts power to the sample or reference to remove this difference. Thus, the sample and the reference are maintained at the same temperature by continuous and automatic adjustment of the power input. A signal, proportional to the difference between heat input to the sample and that to the reference, dH/dt in units of watts, is continuously monitored by the instrument's computer.

A schematic drawing of the core of this instrument, consisting of the sample holder, is shown in figure 2.4(b). The sample is enclosed in a sealed metal pan to avoid contamination of the sample holder. The complete DSC instrument consists of two such holders, one containing the sample in a sealed pan, called the sample holder and the other an empty but sealed pan called the reference. Both pans were continuously purged with a flow of argon gas at a pressure of two bars. The output signal of the calorimeter is

31

proportional to the difference in the heat flow to the samples and the reference, which is equal to $(dH/dT)_q$, where q is the heating rate or the cooling rate. The quantity, $(dH/dT)_q$ is directly proportional to the specific heat, C_p, of the sample. Therefore, the sample's C_p may be calculated by appropriate subtraction of the pan's contribution and using the sample's mass.

The sample pan used to contain the sample and reference were shallow aluminum pans with a diameter approximately 5 mm, height 2 mm, thickness 0.1 mm and nominal mass of 20 mg. Mass of different pans differed by 1 %. An empty aluminum pan with or without lid was placed in the reference compartment to balance the thermal mass with that of the sample compartment. In a typical experiment, an aluminum lid was crimp-sealed with mechanical crimping device for the sample. A typical sample mass used was between 5-20 mg. The lower mass of the sample minimized the thermal lag between the samples and its heaters. A baseline scan against the temperature of two empty pans one kept in the sample pan holder and the other in the reference pan holder helped to minimize the effect of mass difference of aluminum pans. This baseline was subtracted from the DSC thermogram obtained with the sample in the sample pan. By using this procedure, more accurate results were obtained.
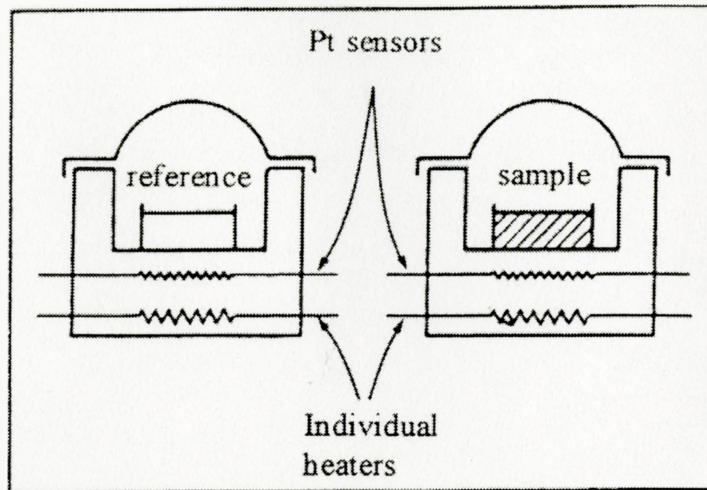
(a)
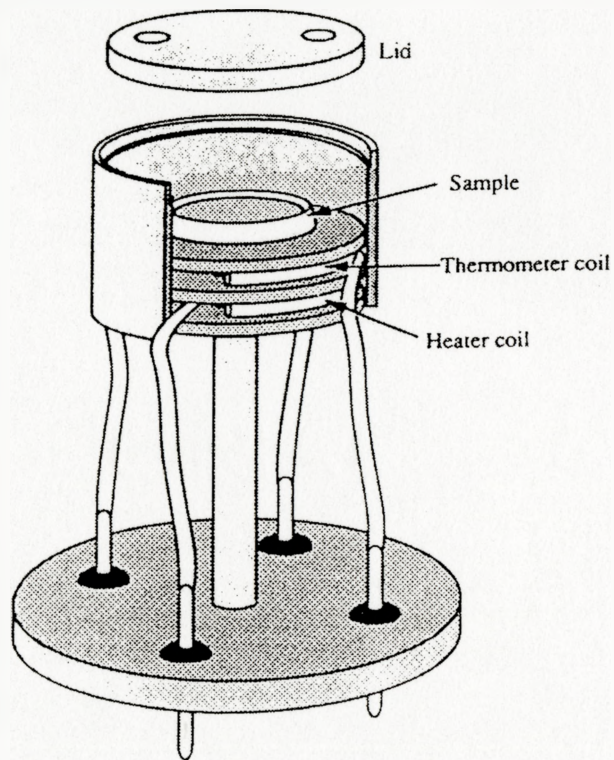
(b)

Figure 2.4 (a) Schematic diagram of Perkin Elmer Differential Scanning Calorimeter Cell, (b) Picture of DSC sample chamber

2.2.3.2 <u>Sample Preparation</u>

Two procedures of sample preparation of zinc nanoparticles were used for calorimetry, as follows:

1. Zinc nanoparticles stored in glass vials were transferred into the DSC pan while keeping all in a glove bag. For this purpose, the glove bag was flushed by high purity argon gas (99.998 % with less than 5 ppm impurities of H_2O and O_2) in order to remove the moisture and oxygen so that the oxidation or combustion of the sample could be avoided. Then the necessary equipment for sample transfer was transferred into the glove bag, and the glove bag was sealed. The zinc nanoparticles were transferred into the DSC pans while inside the glove bag. After the pans contained sufficient amount of the nanoparticles, they were covered with the lids, mechanically crimp-sealed and stored in small sealed glass vials. After this the glove bag was opened and the samples contained in the glass vials were weighed by means of a microbalance. This process took about two minutes. Immediately after weighing, the samples were put back into the glass vials and stored along with dry silica gel in resealable Ziploc plastic bags until needed for the measurements.

2. Zinc nanoparticles from different stock contained in the glass vials were put inside the glove bag without argon flush so that the samples could become contaminated by the atmospheric gases, increasing the probability of their oxidation. The samples transferred to the DSC pans were left in this condition for at least one hour. The pans were mechanically crimp-sealed while still inside the glove bag. Thereafter, the sample pans were weighed and stored in small glass vials inside resealable Ziploc plastic bags until needed for performing the DSC measurements.

Bulk crystalline zinc in the shape of teardrops had been stored at ambient temperature in a sealed glass container. These were studied in the same manner as nanoparticles except that in one set of experiments, the sample pans were left open to air. In several studies the teardrop shape bulk zinc was flattened and cut into flat samples of 3 mm × 3 mm × 0.5 mm dimensions.

2.2.3.3 Differential Scanning Calorimetry Scans

For studies by the Perkin-Elmer Pyris Diamond DSC, the purge gas used was 99.998 % high purity Argon, because its higher thermal conductivity assists in the heat flow. To ensure the accuracy of measurements, the instrument was calibrated for its baseline, sample temperature, furnace heating rate and heat flow prior to the measurements. However, even after this calibration, a temperature lag between the programmed temperature and the sample temperature persisted. For example, for the heating scan of pure bulk zinc at 10 K/min, the onset temperature for melting was found to be 687.5 K, which is 5.2 K less than the reference melting point value of 692.7 K reported by Grønvold and Stølen (1999, 2003). Therefore, a correction for the thermal lag was applied to the experimental data obtained. The thermal lag corrections varied with the heating rate, which are 5.2 K for 10 K/min rate, 3.8 for 20 K/min rate, and 2.9 for 40 K/min rate on both heating and cooling.

Experiments were performed for heating rate of 10 K/min for both the zinc nanoparticles and bulk zinc, also for the cooling rate of 10 K/min over the temperature range from 608 K to 713 K. Experiments were also performed for 20 K/min and 40 K/min heating rates, and for the same cooling rates over the temperature range of 573 K to 713 K. For each heating and cooling rate of the 10, 20 and 40 K/min rate, a new sample of the nanoparticles and of bulk zinc was used. Each sample was cycled as many as five times of heating and cooling through the above-given temperature range in order to determine the change in its state.

2.2.3.4 The Heat Capacity Measurement

For measuring the heat capacity, C_p, of zinc nanoparticles the calorimeter was calibrated with sapphire, whose C_p is known over a wide temperature range from 14 K to 1173 K in the literature [Ginnings and Furukawa (1953)]. C_p was determined by using the Multiple Curves Specific Heat software available for the Perkin Elmer Pyris equipment.

35

In the procedure used, several heating scans were made at the same heating rate of 20 K/min for an empty DSC pan over the temperature range of 323 K to 373 K.These scans were used as the baseline. Measurements were repeated for samples of bulk zinc, zinc nanoparticles, and sapphire. During these experiments, an empty pan, whose weight was within ± 0.05 mg of the weight of the pans used for containing the sample, was used as a reference. This matching of the weight of the DSC pans was crucial because the mass difference can result in a difference in the measured C_p from the true value. C_p was then calculated by comparing the DSC signals by using the following equation:

$$C_p^{Zn} = \frac{\Delta HF^{Zn} m^{Zn}}{\Delta HF^{sapp} m^{sapp}} C_p^{sapp} \tag{2.1}$$

where C_p^{Zn} and C_p^{sapp} are the respective heat capacities of zinc and sapphire and m^{Zn} and m^{sapp} their respective mass. The quantities ΔHF^{Zn} and ΔHF^{sapp} are the difference of the respective materials from the respective baselines that had been obtained by using empty DSC pans in each case.

Measurements were repeated at least three times. In each experiment a new sample was used and it was ensured that the oxidation of the nanoparticles to ZnO was minimum or negligible. A relatively low temperature range was chosen for measuring C_p in order to avoid agglomeration of nanoparticles and further ZnO formation on the surface of nanoparticles.

2.3 Electron Microscopy Results and Discussions

2.3.1 Transmission Electron Microscopy

Since the size distribution of nanoparticles zinc was not provided by the supplier, it was decided to determine first the histogram of the particles. For this purpose, Zn nanoparticles were agglomerated into a mass (collection of particles) that had the shape of roughly a sphere, and in which sharp facets of the nanoparticles were found to be arranged such that they pointed outwards. The radius of the spheres was in the 1-2 μm range. During the TEM experiment, as these agglomerates were hit by high intensity electron beam, the Zn nanoparticles spread out onto the carbon film and clearly showed their triangular, hexagonal, etc., faceted shapes, belonging to a hexagonal crystal. The photographs of the spreading out were not taken. But photographs of a similar spreading of the agglomerate and showing of the facets have been reported by Yan et al. (2003) from their studies of zinc nanoparticles. They had named the spread-out state of the nanoparticles as zinc nanodisc and nanobelt.

The TEM picture of the spread-out state zinc nanoparticles is presented in figure 2.5 (b). From such pictures, the particle size was determined, and it was found to be in the 30 - 200 nm range, instead of 35 - 80 nm, provided by the supplier. A histogram of the size of the particles is provided in figure 2.5 (a). It shows that the majority of particles are of 30 - 40 nm width and then an equal proportion in the 50 - 70 nm width.
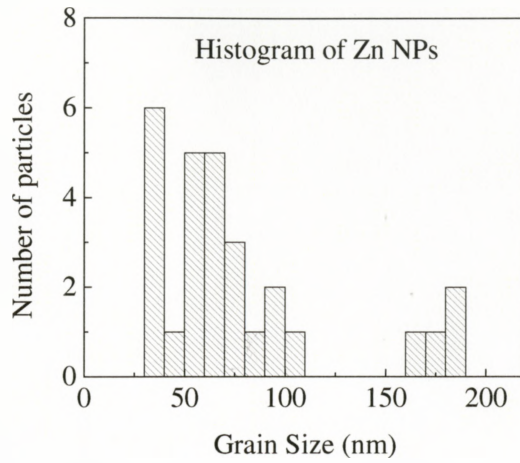
(a)
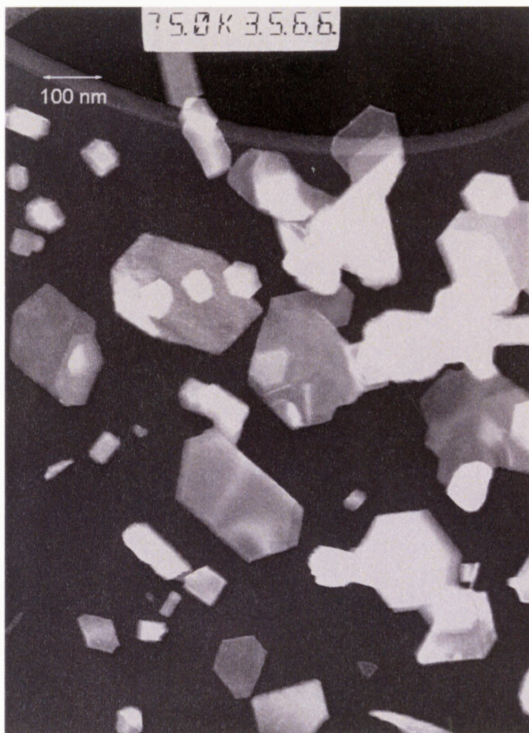
(b)
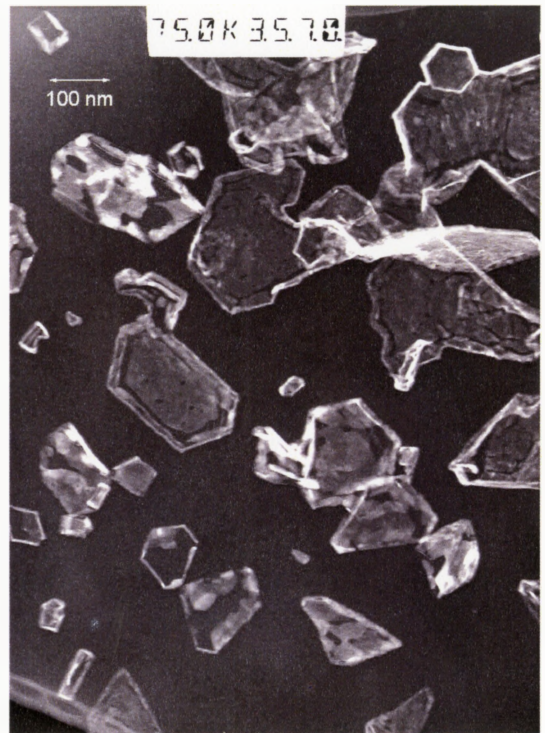
(c)

Figure 2.5 (a) The size distribution of zinc nanoparticles, **(b)** The TEM Bright Field picture of Zn nanoparticles at 298 K before and **(c)** after heating up to 20 K above the melting point of bulk zinc

38

To examine the effect of melting and the possibility of oxidation of the Zn nanoparticles, the spread-out particles while still in TEM holder were heated from 298 K to 713 K, which is 20 K above its melting point, and then cooled to 298 K. The heating rate and the cooling rate were not automatically controlled and therefore not recorded. The TEM picture of the particles taken at 298 K after the thermal cycling is shown in figure 2.5 (c).

The TEM photograph in figure 2.5 (c) shows that the particles contrast has faded and they appear as a skeletal shell with only the surfaces showing. Shape of the particles does not change but the intensity of the particles fades during their heating to 713 K, which is about 20 K above the melting point of bulk Zn, and then cooling to room temperature. During this experiment, a decrease of intensity was observed on heating, which indicated the beginning of melting process of nanoparticles at temperature in the 633 - 653 K range. This fading continued until all particles reached the same intensity at about 673 K. After the temperature had reached 713 K, the sample was cooled back to the room temperature. During the cooling it was noted that the intensity of the sample was not restored. This is in contrast to the expectation that the molten zinc would solidify and the intensity of the sample shall return to the initial intensity. The loss of intensity on thermal cycling indicates that during heating process, the sample did not only melt but that its melt also vaporized in the vacuum environment inside the TEM. Therefore what is left after cooling back to room temperature is the skeletal shell of ZnO layer that probably had already formed during the drying of the samples outside the microscope column.

Vaporization of a material occurs much more rapidly when it is in a small size, a phenomenon known as the Kelvin effect. The vapour pressure increases as particle size decreases, according to the equation,

$$\ln\left(\frac{P_r^{sat}}{P_\infty^{sat}}\right) = \frac{2\gamma V_L}{RTr} \tag{2.2}$$

$P_r^{sat}, P_\infty^{sat}$ = Vapor pressure of particle with radius r and of bulk particle respectively

γ = Surface tension, for zinc = 0.99 J m^{-2} [Vitos et al. (1998)]

39

V_L = Molar volume, for zinc$_{(l)}$ = 9.88 x 10^{-6} m^3 mole^{-1}

R = Gas constant, 8.3144 J/mole K

T = Temperature (K)

r = Radius of the particles

This means that the vapour pressure of the nanoparticles in the liquid Zn will be ~ exp(4/r) the vapour pressure of bulk liquid Zn at 692.68 K and r in nm, which makes their complete evaporation much more probable. There is no doubt that some of the solid particles would also sublime on raising the temperature towards the melting point. Thus, in the vacuum environment of 10^{-7} Torr, Zn metal from the nanoparticles evaporated at a temperature far below the bulk boiling point, 1180 K, and escaped from the surroundings of the particles.

Since all zinc metal had escaped, only the rigid shell remained after the above-described thermal cycling. This shell is likely to be made from ZnO which did not melt and which, like all other metal oxides, has too low vapour pressure to escape in the vacuum of 10^{-7} Torr.

2.3.2 High Resolution Transmission Electron Microscopy

In order to confirm whether or not the shell was entirely ZnO, a study of Energy Filtered TEM (EFTEM) and Scanning TEM (STEM) using the High Resolution TEM (HRTEM) were performed, as described below:

2.3.2.1 Zero Loss Filtered Imaging

The image of the region to be analyzed was taken using zero loss filtering technique, in which zero loss peak is aligned with the optic axis. The energy slit width was chosen to be 50 eV wide. The transmitted electrons were filtered by the energy slit so that the image contained only elastically scattered electrons, while inelastically scattered electrons, which caused blurring effect on the image, were removed. The zero loss filtered image of a zinc nanoparticle after heating to 713 K and cooling back to room temperature is shown in figure 2.6 (a), where contrast between the shell and the inner part is clearly observable.

2.3.2.2 Energy Dispersive X-ray Analysis

Energy Dispersive X-ray was then performed at different locations of zinc particle, i.e. at the inner and edge region of the particle. The image of the post-heated zinc particle after the EDX spectra were collected is shown in figure 2.6 (b). Note that the location at which the EDX spectra had been collected were hollow due to drilling and penetration of electrons through the sample.

(a)   (b)
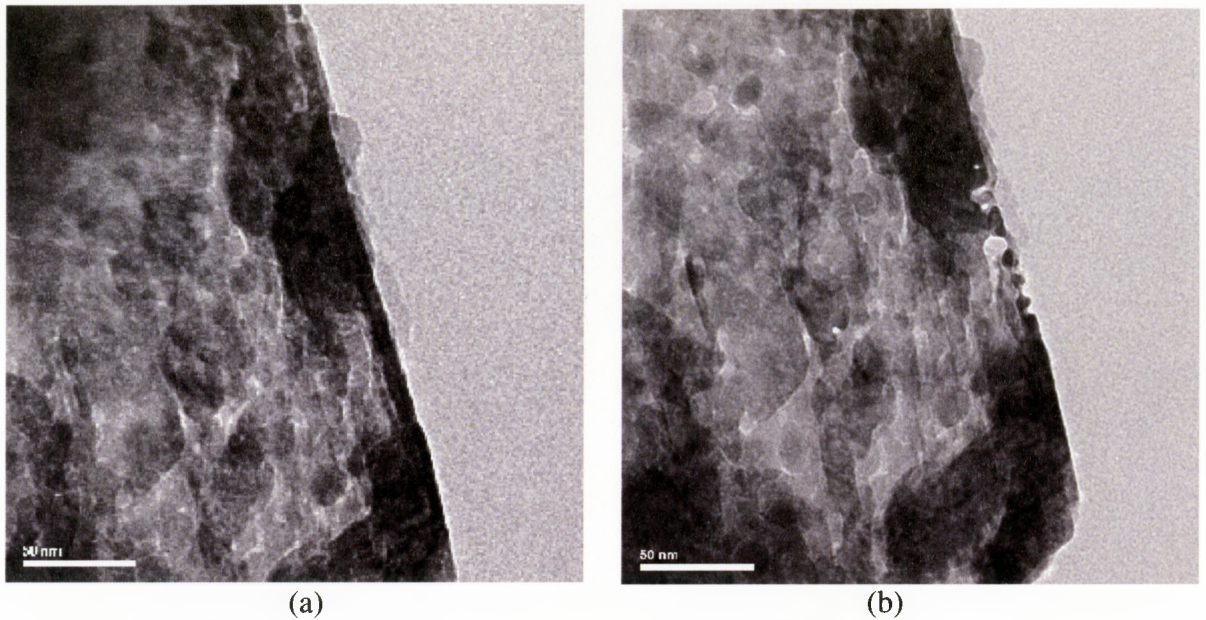
Figure 2.6 Zero Loss Filtered images of post-heated Zn particle **(a)** before and **(b)** after obtaining EDX spectra

The EDX spectra taken for the inner and edge region of zinc particle were collected and analyzed using *INCA*, elemental concentration analysis software. Since the main interest of elemental concentration analysis here is to determine the composition of the oxide at the outer layer of particle, other elements that are not of our interest were excluded from the analysis.
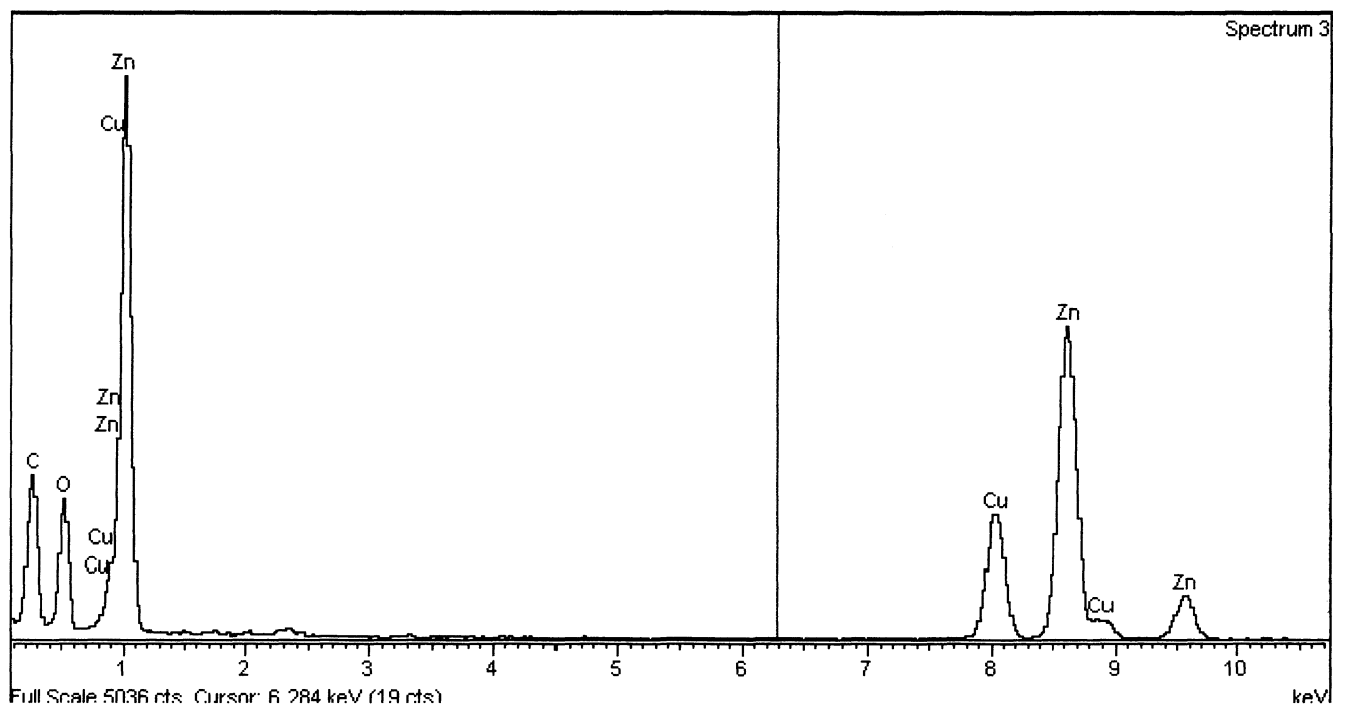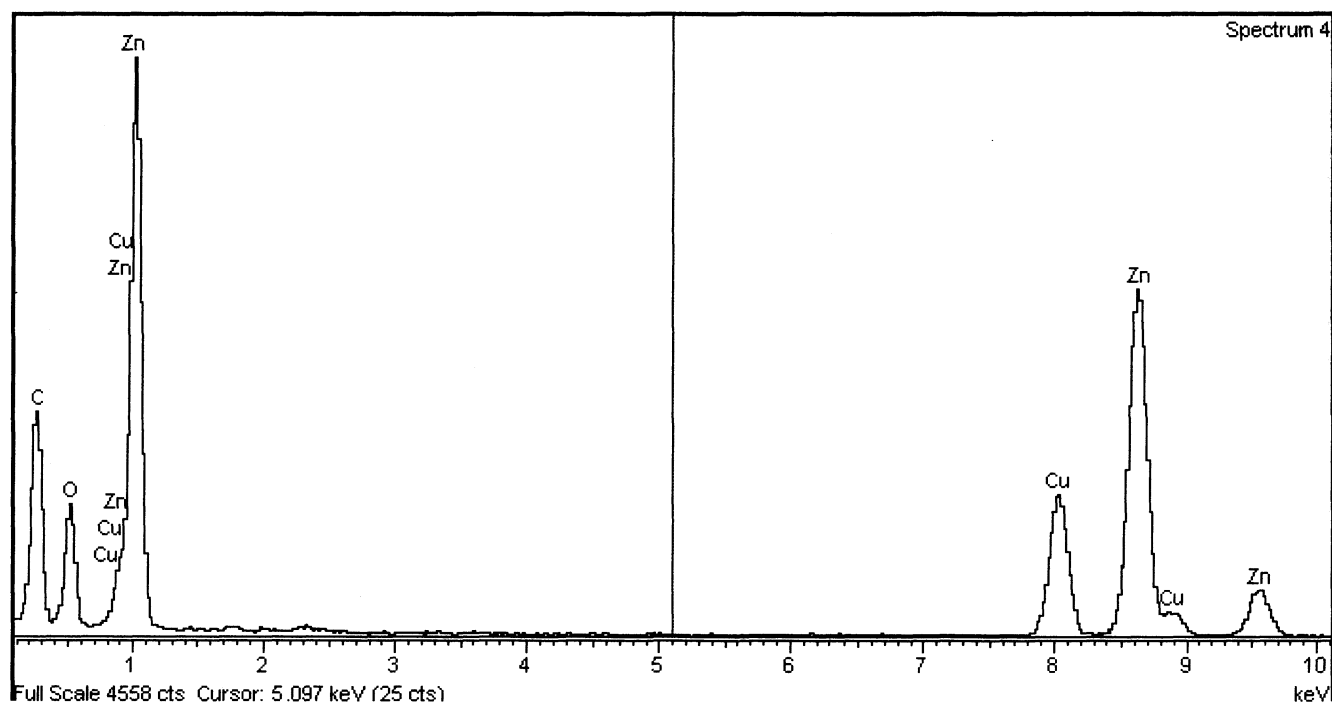
Figure 2.7 (a) EDX spectrum 3 was taken from the inner region of the Zn particle and
(b) spectrum 4 was taken from the edge region of Zn particle

The EDX spectra in figure 2.7(a) and 2.7(b) show that the major elements are zinc and oxygen, which confirm the presence of zinc oxide in the zinc particle that had been heated to 713 K. The C and Cu peaks seen in the figures are from the substrate of carbon thin film and the copper grid supporting zinc nanoparticles.

Therefore, the spectra analysis was focused on Zn and O, and the other elements were excluded from the concentration calculation using *INCA* software. The weight and atomic percentage for Zn and O based on their intensity in spectrum 3 and 4 are presented in Table 2.2. From this EDX analysis, the zinc oxide formed was confirmed to be ZnO instead of ZnO_2.

Table 2.2 The weight and atomic percentage of Zn and O elements from spectrum 3 and spectrum 4 corresponding to the inner region and edge region respectively of Zn particle

Spectrum	Weight (%)		Atomic (%)	
	Zn	O	Zn	O
3	77.65	22.35	45.95	54.05
4	80.26	19.74	49.87	50.13

2.3.2.3 Energy Filtered TEM Elemental Mapping

The EFTEM elemental mapping was performed using the three-window technique. Electron Energy Loss Spectra was generated firstly to align the Zero Loss Peak and secondly to find the right position of Zn and O edges for determining the position of three windows for spectrum imaging. The three-window method for Zn-$L_{2,3}$ (1020 eV) and O-K (532 eV) consequently was performed with the energy slit width of 20 eV. After the pre-edge 1, pre-edge 2 and post-edge images were obtained, the post-edge image was then subtracted from the extrapolation of the background from pre-edge 1 and pre-edge 2 images. The subtraction finally gave an elemental map showing the

distribution of Zn and O in the region of interest. The elemental map of the O-K and Zn-$L_{2,3}$ are presented in figures 2.8 (a) and (b) respectively.

(a)   (b)
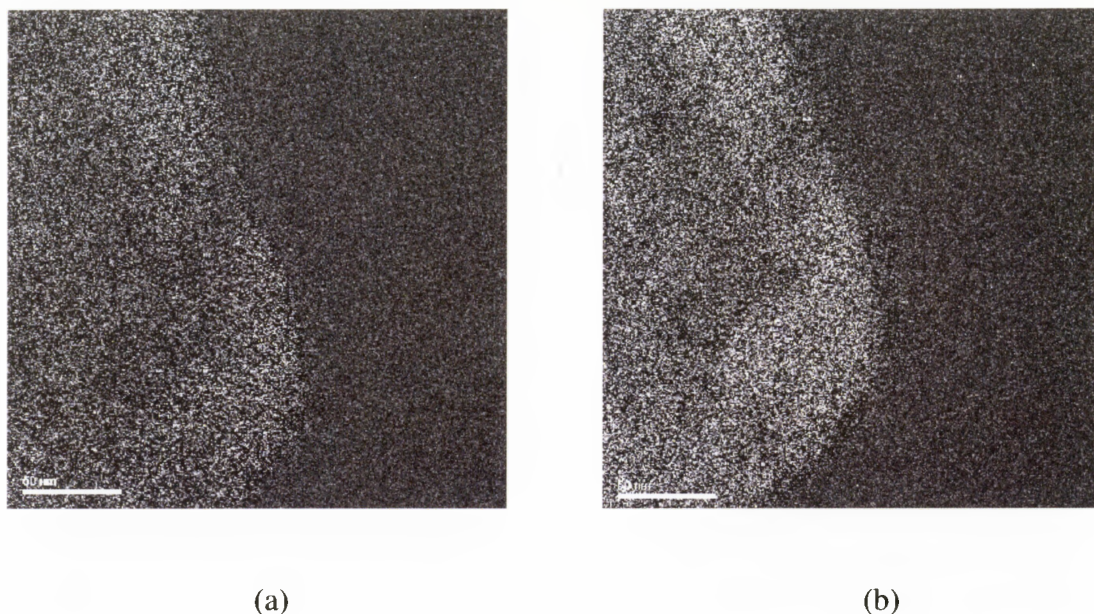
Figure 2.8 **(a)** O-K and **(b)** Zn $L_{2,3}$ elemental map obtained by using the three-window
EFTEM electron spectrum imaging

The Zn and O elemental maps showed that both Zn and O are more concentrated at the edge than at the inner region of the particle. ZnO shell formed shows a non-uniform thickness around the particle. Very weak signals of both Zn and O coming out from the inner region represent less concentration of both elements. This again confirms that on heating, Zn metal melted, evaporated and left the inner region to be filled by oxygen. The non-uniformity of the thickness of ZnO shell (30 – 50 nm) indicates the regions at which the crack was formed due to hydrostatic stress.

2.3.2.4 Scanning TEM Line Profiling

STEM line profiling was performed for observing the distribution of Zn and O along the shell of the particle. The results are shown in figure 2.9 and 2.10.
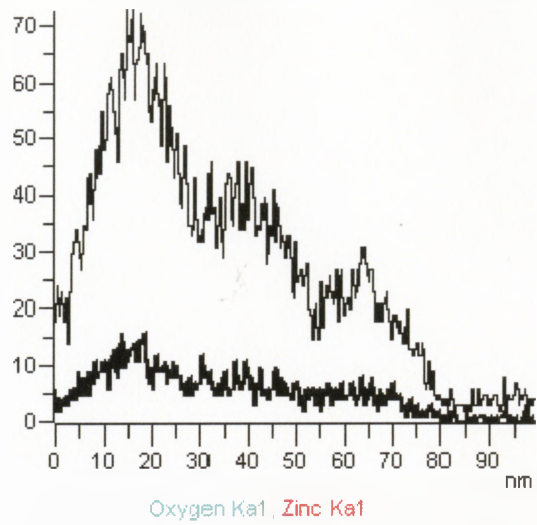
Figure 2.9 STEM Element Linescan of Zn and O
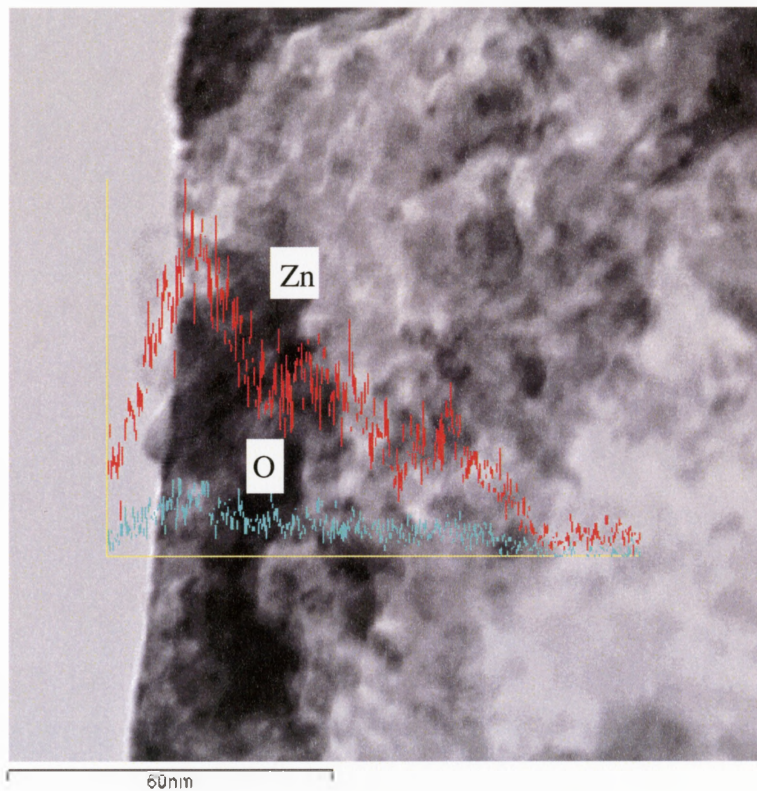
Figure 2.10 Position of the STEM linescan at the particle

The STEM linescan elemental profiling in figure 2.9 shows that the concentration of Zn and O decreases as one moves from the initial position toward the inner region of the particle. The slight displacement of the particles from its initial position was caused by the thermal expansion of the Cu-grid C film substrate. The concentration of zinc at ~ 60 nm depth from the surface plummeted down to nearly zero.

We now consider at what stage of the thermal treatment could ZnO have formed on the surface of Zn nanoparticles. Since all thermal-cycling treatment was performed in the vacuum environment of TEM, surface oxidation could have occured either during the production of the particles or during the handling of the particles prior to the TEM observations. In that case, it is necessary to explain how metal zinc could have escaped in vacuum through the ZnO skin of the nanoparticles. To examine this aspect it is necessary to recall some properties of ZnO, as follows:

The melting point of ZnO is 2248 K, much higher than that of Zn, yet its thermal expansion coefficient is $4 \times 10^{-6}\,K^{-1}$ which is much lower than the thermal expansion coefficient of $60.8 \times 10^{-6}\,K^{-1}$ for zinc in c-axis direction as noted by Wu et al. (2000).

Therefore, during heating in our TEM experiment, zinc metal expands more than its ZnO shell. This creates a hydrostatic pressure in both solid zinc and liquid zinc inside a hermetically sealed particle. Since the modulus of elasticity of ZnO, 210 GPa [Kittel (1996)], is higher than that of the Zn metal, 70 - 140 GPa [Matthewson (1959)], this hydrostatic pressure would rupture the ZnO shell. The crack formed would then expose the molten zinc to the TEM vacuum into which the molten zinc would escape in the vapour form, leaving the ZnO skeletal shell behind. If the nanoparticles were not hermetically sealed, the pressure generated by the expansion of the metal zinc would widen the already present crack in it, allowing easier escape of the zinc into the vacuum. In addition, it is conceivable that any oxygen present would increase the ZnO skeletal shell layer thickness, but the probability of oxygen present in 10^{-7} Torr vacuum is relatively small and therefore the process of thickening of the ZnO shell would be slow, if any.

Referring to Table 2.2 in section 2.3.2.2, the higher concentration of oxygen in the edge region than the inner region ensures that ZnO layer was formed. Since ZnO layer is brittle and the difference of thermal expansion coefficient between ZnO-Zn metal is large, the ZnO layer would therefore be easily cracked. The cracks in the ZnO layer provide crevices through which molten Zn would be able to come out and oxygen from the atmosphere to come in. The less concentration of zinc in the inner region than in the edge therefore confirms that molten zinc coming out of the ZnO shell later evaporated due to the vacuum environment.

2.4 Differential Scanning Calorimetry Results and Discussions

2.4.1 The Heat Capacity of Free Zn Nanoparticles

Since Zn melts at 692.7 K, there is a possibility that the endothermic heat of melting that could appear for nanoparticles at their melting temperature far below 692.7 K could effect the heat capacity, C_p, measurements. For that reason, the temperature range chosen for the C_p measurements was 323 K - 373 K. These values are listed in Table 2.3. For comparison, C_p of bulk Zn was also measured by the same equipment under the same conditions. These values are also provided in Table 2.3.

Table 2.3 The heat capacity of nanoparticles zinc, $C_{p,NPs}$, bulk zinc, $C_{p,bulk}{}^m$, as measured here and the corresponding value, $C_{p,bulk}{}^l$, for bulk zinc taken from the literature Grønvold and Stølen (1999, 2003), at different temperatures

T (K)	$C_{p,NPs}{}^m$ (J/mol K)	$C_{p,bulk}{}^m$ (J/mol K)	$C_{p,bulk}{}^l$ (J/mol K)	$\Delta C_{p,bulk}{}^{m-l}$ (%)	$C_{p,NPs}{}^m - C_{p,bulk}{}^m$ (%)
330.24	30.02	26.62	25.84	3.02	12.78
337.25	29.53	26.43	25.91	1.99	11.76
344.24	29.86	26.56	25.98	2.22	12.44
351.24	30.15	26.69	26.00	2.64	12.99
358.27	30.38	26.69	26.10	2.25	13.85
365.28	30.35	26.69	26.19	1.90	13.73
372.30	30.25	26.75	26.20	2.11	13.08
			Average	2.30	12.95
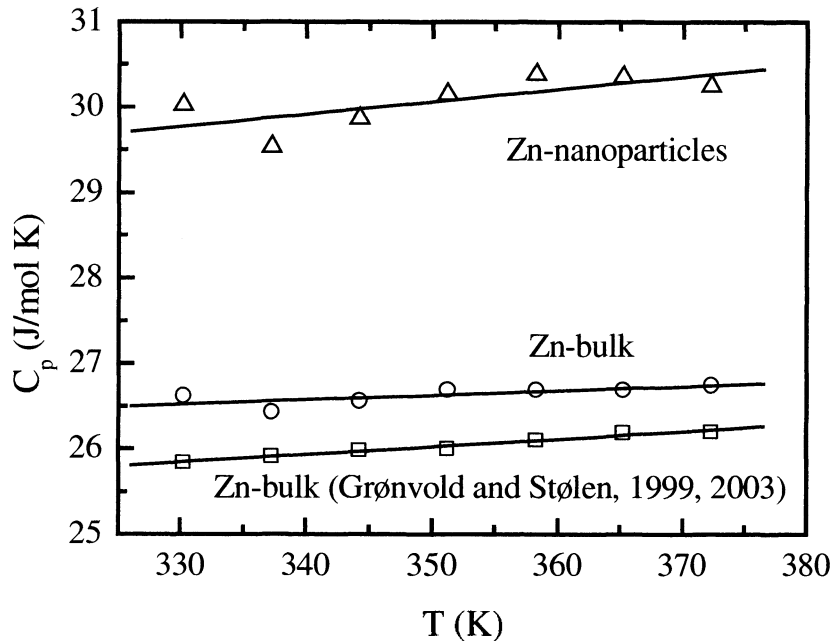
Figure 2.11 The measured heat capacity of the bulk and nanoparticles zinc and the literature values for bulk zinc over the 333 K - 373 K range

In Table 2.3 and Figure 2.11, the average C_p value measured for bulk zinc over the 323 – 373 K range is found to be 2.3 % higher than the average C_p value of bulk zinc provided by Grønvold and Stølen (1999, 2003). It should be noted that these values include the instrumental error of ± 1%. Therefore we consider that our values are consistent with the literature values, which themselves vary within 0.2 %.

Table 2.3 and Figure 2.11 also show that the C_p measured for zinc nanoparticles is ~13 % higher than C_p of bulk zinc. Part of this higher C_p value for nanoparticles may be due to the presence of ZnO on the surface of the particles, which may have formed during the production of the particles and/or during their handling in the laboratory. Therefore, it is necessary to consider whether the effect observed is material characteristic or an artefact of the presence of ZnO. It is done as follows:

After a study of gas sensing properties of nanocrystalline zinc oxide, Lin et al. (1998) stated that when nanoparticles Zn, with mean size of 11.1 nm, are sintered in air at 623 K for an hour, their oxidation remains incomplete. Oxidation of nanocrystalline zinc is, however, completed under the same conditions of sintering at 873 K. Their electron diffraction studies of nanocrystalline Zn, i.e. polycrystalline sample containing nanoparticles, indicate that it oxidizes slightly in air and that this slight oxidation results in a thin layer of ZnO on the surface of Zn crystals, which then inhibits further oxidation of the nanocrystalline Zn. Their Differential Thermal Analysis result showed that oxidation of nanocrystalline Zn occurs at about 582 K when it is heated at a rate of 5 K/min in air. From another study of photoluminescence and ultraviolet lasing of polycrystalline ZnO thin film, Cho et al. (1999) have found that 200 nm thick Zn film had totally transformed to ZnO by annealing for at least 30 minutes at temperature above 673 K. More recent observation by Gupta et al. (2002) have shown that in an oxygen atmosphere, ZnO begins to form on 3.1 μm thick zinc film even at 423 K, a much lower temperature.

According to the relation between C_p and temperature provided by Matthewson, C_p of ZnO in the temperature range of 323 - 373 K is 41.90 - 44.34 J/mole K. Therefore, there is a possibility that the higher heat capacity of nanoparticles zinc than that of bulk is due to the contribution of ZnO formed on the surface of nanoparticles. However, since all the best precautions in handling the nanoparticles had been performed, i. e.

- the samples for C_p measurement had been kept at much lower temperatures, 323 K - 373 K, during the measurement, than in the above reviewed studies,
- high purity (>99.9 %) argon (inert) atmosphere had been used, and
- the nanoparticle samples themselves had been contained in a crimp-sealed pan,

it is very likely that the amount of ZnO formed, if any, was insignificant during the C_p measurement and can therefore be neglected. The higher experimental value of heat capacity of nanoparticles zinc obtained than that of the bulk is only due to the contribution of the nano-size effect. So it can be concluded that the heat capacity of nanoparticles zinc is ~ 13 % higher than that of the bulk.

51

2.4.2 Thermodynamic Changes on Heating and Thermal Cycling

2.4.2.1 <u>Results</u>

The changes in thermodynamic properties of bulk and nanoparticles zinc observed here may now be discussed by using the results of differential scanning calorimetry (DSC scans or thermograms). Preliminary experiments showed that the thermograms contained no significant feature at temperature from 300 K to the onset melting temperature of 713 K. Therefore, only the temperature region over which features of thermodynamic interest occur were studied in detail. These studies consisted of heating from 573 K to a temperature above the melting point, 713 K, and thereafter on cooling to 573 K. At least three sets of calorimetric thermograms were obtained and each set of such thermograms was obtained for the same heating and cooling rate, i.e. 10 K/min, 20 K/min and 40 K/min. In each set of experiment, the nanoparticles zinc sample was thermally cycled five times between 573 K and 713 K. In contrast, the bulk sample was thermally cycled only two times.

The thermograms obtained were corrected for the thermal lag of the instrument, as explained in section 2.2.3.3, which was 5.2 K for 10 K/min rate, 3.8 K for 20 K/min rate and 2.9 K for 40 K/min rate for both cooling and heating. The thermograms for heating at 10 K/min for nanoparticles and for bulk samples are shown over the temperature range of 620 K-710 K in figure 2.12(A). The heating part of the thermal cycle for nanoparticles is labelled from 1 through 5, sequentially. Thermograms obtained during subsequent cooling in each cycle are shown in figure 2.12(B) for nanoparticles and bulk samples. For nanoparticles, these thermograms are labelled from 1' through 5', sequentially, where 1' was measured after 1 and 2' after 2, and so forth.

The corresponding thermograms for 20 K/min heating and cooling rates over the 640 K-720 K temperature range are shown in figures 2.13(A) and 2.13(B).

Figures 2.14(A) and 2.14(B) provide the thermograms obtained by heating and cooling at 40 K/min rate over the 640 K - 720 K temperature range.

The melting point was determined from the onset temperature of the melting endotherm for each DSC thermogram shown in figures 2.12(A), 2.13(A) and 2.14(A) and these values are listed in Table 2.4.

Table 2.4 Data of onset melting temperature of nanoparticles, $T_{m,ZnNPs}$, and bulk zinc, $T_{m,ZnBulk}$ observed in figures 2.12(A), 2.13(A), and 2.14(A)

q_h (K/min)	Cycle #	$T_{m,Zn\ NPs}$ ($^{\circ}$C)	$T_{m,Zn\ NPs}$ (K)	$T_{m,Zn\ Bulk}$ (K)
10	1	417.7	690.9	692.7
	2	416.5	689.6	
	3	416.2	689.3	
	4	415.5	688.6	
	5	415.5	688.6	
20	1	418.2	691.4	692.7
	2	416.6	689.7	
	3	416.5	689.6	
	4	416.6	689.8	
	5	416.7	689.8	
40	1	418.6	691.7	692.7
	2	417.1	690.3	
	3	417.1	690.3	
	4	417.0	690.1	
	5	417.0	690.1	

53
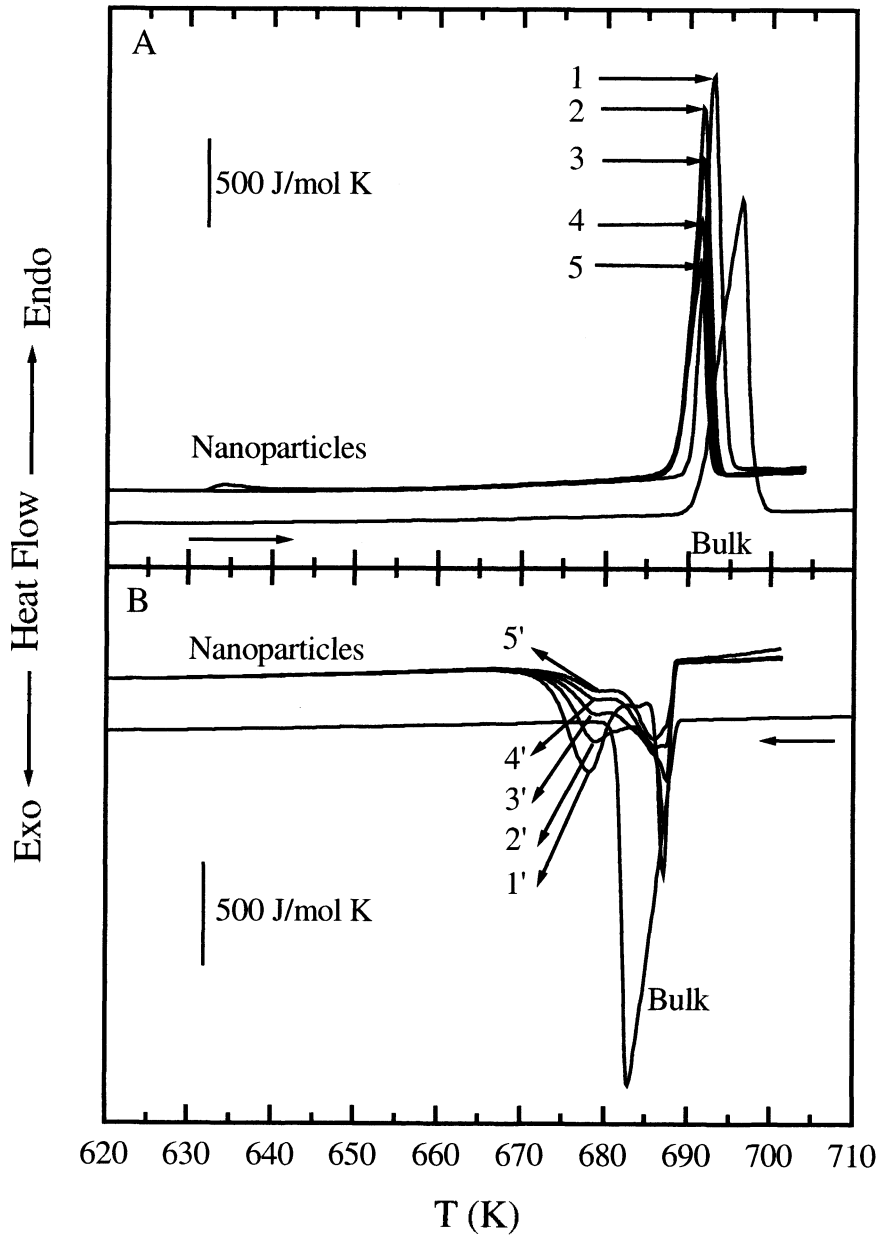
Figure 2.12 **A.** Heating curves of Zn bulk and nanoparticles at 10 K/min **B.** Cooling curves of Zn bulk and nanoparticles at 10 K/min
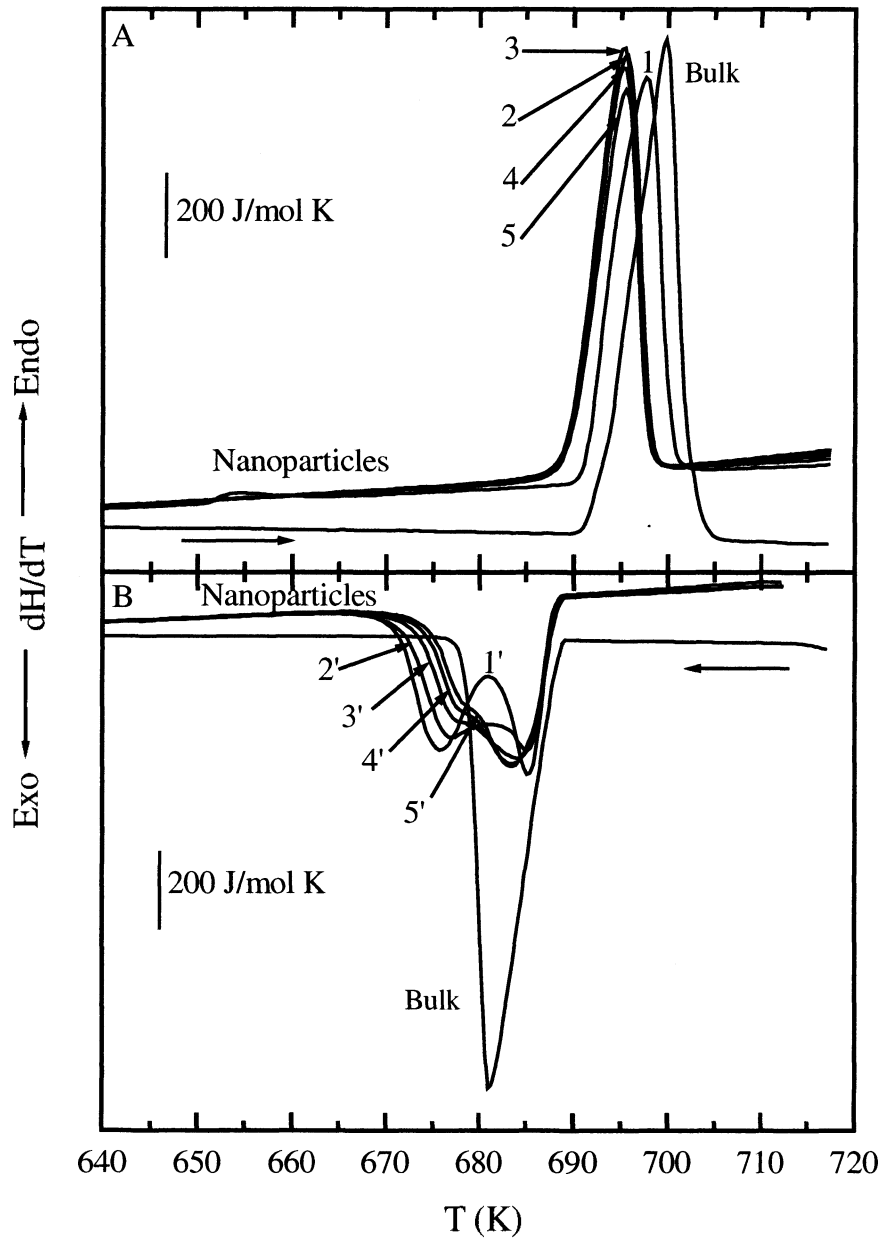
Figure 2.13 **A.** Heating curves of Zn bulk and nanoparticles at 20 K/min **B.** Cooling curves of Zn bulk and nanoparticles at 20 K/min
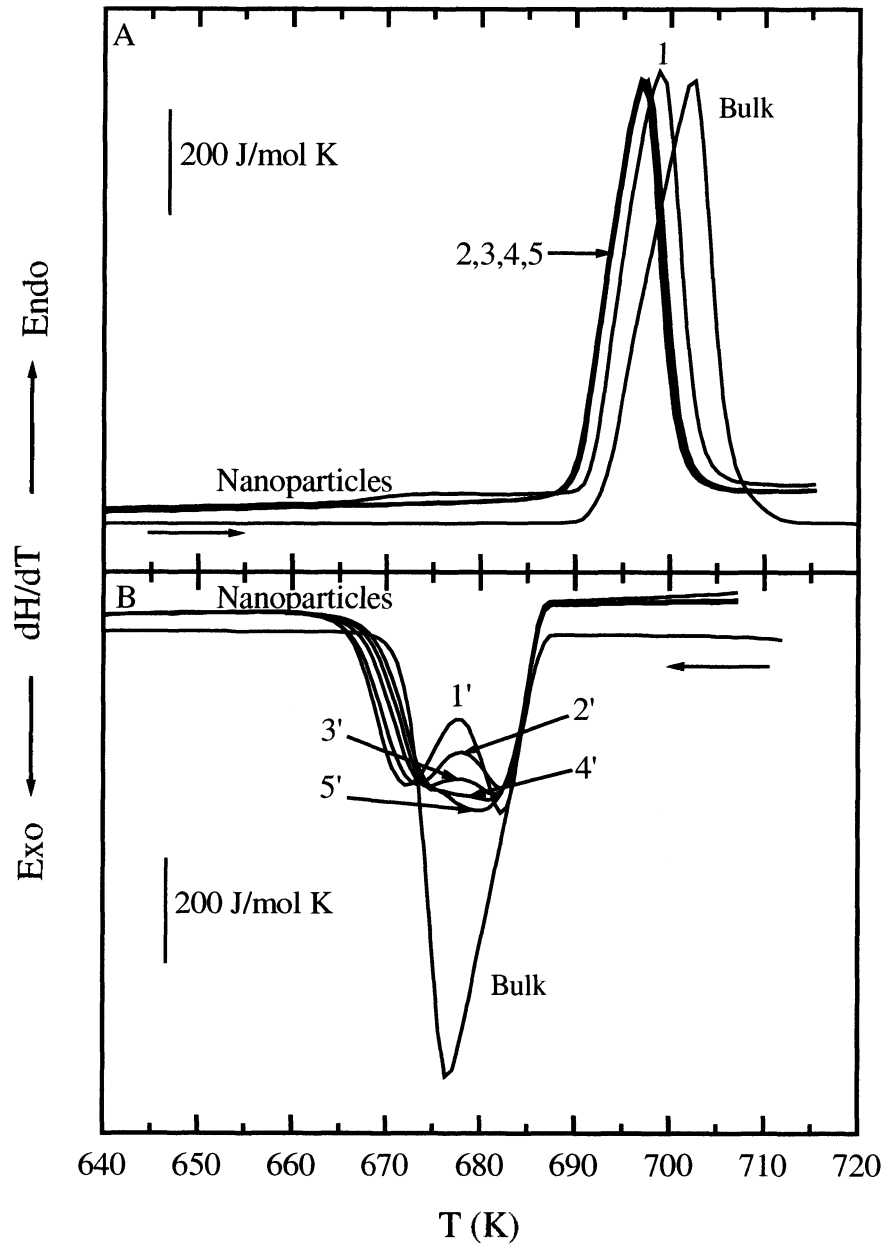
Figure 2.14 A. Heating curves of Zn bulk and nanoparticles at 40 K/min **B.** Cooling
curves of Zn bulk and nanoparticles at 40 K/min

Table 2.4 shows that $T_{m,ZnNPs}$ is 1-2 K lower than $T_{m,ZnBulk}$ for the first cycle. With further thermal cycling, $T_{m,ZnNPs}$ decreases and reached a relatively constant value after the third cycle. This value is 688.6 K for 10 K/min heating rate, 689.8 K for 20 K/min and 690.1 K for 40 K/min heating rates. In all cases a comparison against the melting point of bulk zinc shows that there is a significant decrease in the melting point of the nanosize particles. The difference between 688.6 K and 690.1 K decrease indicates that the nanoparticles were not in the specified size range of 35-80 nm, instead in the size range of 30 – 200 nm. This has been confirmed by the histogram and by the electron micrographs shown in figure 2.5(a), which were obtained by the TEM observations.

In figures 2.12(A), 2.13(A) and 2.14(A), a small endothermic feature on the low-temperature side of the main endothermic melting peak appeared in the first heating cycle of all nanoparticle samples regardless of the heating rate. This small endothermic feature which appears at about 670 K disappears from thermograms obtained from further heating cycle. The onset temperature, $T_{o,small}$, and end temperature, $T_{e,small}$, of the small endothermic feature observed from various heating rates, also the T_m of nanoparticles for the first cycle are listed in Table 2.5.

Table 2.5 The onset, $T_{o,small}$, and end temperature, $T_{e,small}$, of small endothermic feature and T_m of nanoparticles observed on heating at different rates

Heating Rate	10 K/min	20 K/min	40 K/min
Mass	8.36 mg	26.46 mg	17.82 mg
$T_{o,small}$ (K)	632.0	652.6	666.3
$T_{e,small}$ (K)	639.6	674.4	685.3
$T_{m,NPs}$ (K)	690.8	691.3	691.6

Feature of DSC thermograms of crystallization may now be discussed. Thermograms obtained for nanoparticles on cooling in the first thermal cycle provided in figures 2.12(B), 2.13(B) and 2.14(B) show double exothermic minima. Since the bulk sample shows only one exothermic crystallization minimum, the double exothermic

minima is attributed to a two-stage crystallization of molten zinc within nanoparticles. On further thermal cycling, the two exothermic minima of nanoparticles eventually merge, and its temperature width, ΔT, decreases. The onset and end temperatures of crystallization and the temperature width are listed in Table 2.6.

Table 2.6 The onset, $T_{o,cryst}$, and end temperature, $T_{e,cryst}$, of crystallization and the temperature width, ΔT, of nanoparticles zinc on cooling as observed in figures 2.12(B), 2.13(B), and 2.14(B)

q_c (K/min)	Cycle #	$T_{o,cryst}$ (K)	$T_{e,cryst}$ (K)	ΔT (K)
10	1	688.5	673.4	15.0
	2	688.6	673.7	14.9
	3	688.6	675.2	13.4
	4	688.6	679.7	8.9
	5	688.7	681.2	7.5
20	1	689.5	672.2	16.8
	2	689.5	673.3	16.2
	3	689.6	674.4	15.2
	4	689.8	675.2	14.6
	5	690.0	675.7	14.3
40	1	688.8	668.6	20.2
	2	689.0	669.0	20.0
	3	689.0	669.8	19.2
	4	689.1	670.6	18.5
	5	689.1	671.3	17.8

2.4.2.2 Discussions

2.4.2.2.1 Decrease of T_m

The decrease of T_m of nanoparticles zinc observed is attributed to the decrease in the size of zinc metal particles as an increasing amount of ZnO layer forms and consumes the zinc metal. As mentioned in Section 2.4.1, Lin et al. (1998) have observed ZnO formation in nanocrystalline zinc, which begins at 582 K for 5 K/min heating rate in air atmosphere. Since our samples were heated to 713 K, more ZnO would form in our samples of zinc nanoparticles. This is supported by our observation in Table 2.4 that the decrease of T_m of nanoparticles occurred continuously and reached a final value instead of occurring instantaneously.

However, the appearance of crystallization peak on cooling and melting peak on subsequent heating indicates that thermal cycling does not transform all nanoparticles zinc into ZnO. In subsequent thermal cycles, the transformation of zinc crystal into ZnO on the surface of nanoparticles is retarded by the presence of the former ZnO layer, acting as a barrier for agglomeration and further diffusion of oxygen. As ZnO layer thickens, the diffusion of oxygen through the layer becomes more and more difficult so that the decrease in size of zinc crystals occurs progressively slower during the time scale of our study. Thus slower diffusion of oxygen through an increasing thickness of ZnO on zinc metal particles and decreasing surface area of zinc metal particles prevent the total oxidation, and smaller zinc metal particles persists even after several thermal cycling.

In addition to progressively slower transformation of zinc crystal to ZnO, there is another phenomenon that appears during thermal cycling which promotes the thickening of ZnO layer. As discussed in Section 2.4.1, Wu et al. (2000) have explained the hydrostatic pressure build-up within a ZnO sealed nanoparticles zinc due to the difference in the thermal expansion coefficient between zinc metal and zinc oxide during thermal cycling. They also suggested that the difference between their respective modulus of rigidity makes the initially-formed, thin layer of ZnO more prone to cracking on increase

59

of the hydrostatic pressure inside the ZnO coated particle. The cracks formed on ZnO layer provide an entrance for oxygen diffusion into the zinc crystals. This enhances growth of ZnO layer on further thermal cycling. Therefore as the ZnO layer reach a sufficient thickness to resist cracking that may be caused by the hydrostatic pressure build-up, the zinc crystal size within nanoparticles would become constant. This is observed here in terms of the approach of a relatively constant T_m of zinc nanoparticles after the third or fourth thermal cycle.

2.4.2.2.2 Small Endothermic Feature

In the preliminary studies of nanoparticles zinc reported by Wu et al. (1998, 2000, 2002, 2004), a sharp endothermic peak at ~ 639 K was found in one DSC scan when the nanoparticles was heated at 20 K /min heating rate. In comparison, our results for 20 K/min heating rate show a small endothermic peak at 652.6 K. Yet, its height relative to that of the melting endotherm is only 2 % in comparison with the height of the corresponding peak observed by Wu et al. (2000). They had attributed this small endotherm to the evaporation of the sample when the ZnO film ruptured during heating as a result of the pressure increase inside.

In order to investigate the origin of this endotherm at 652 K, the sample was thermally cycled between 608 K and 673 K without melting. The DSC scans were obtained during both heating and cooling at the same rate, i.e. 10 K/min, 20 K/min and 40 K/min. The small endothermic feature was observed only on the first heating cycle and not in the subsequent ones.

As shown in Table 2.5, the onset temperature and position of the small endothermic feature increase with increase in the heating rate. Since it appears only in the first heating scan, and not thereafter, it may not be due to evaporation of zinc nanoparticles, as suggested by Wu et al. Rather it may be due to an intrinsic effect that vanishes on thermal cycling.

To investigate the origin of the small endothermic feature at 652 K, we first considered whether it can be due to melting of very small nanoparticles. But since this peak is found to depend on the heating rate in our study, this feature would appear to be due to a kinetically controlled instead of thermodynamically controlled process. However, if this small endotherm is considered to indicate melting of small nanoparticles, one possible reason why its onset temperature depends on heating rate may be due to an appreciable thermal lag between sample and instrument sensor when the ZnO layer formed had a thermal insulation effect on the zinc metal particles. This possibility is considered as follows:

Even though the nanoparticles are contained in a mechanically crimped DSC pan, in which a good thermal contact between the samples and the pans is maintained, the presence of ZnO layer of lower thermal conductivity that encages the nanocrystals zinc would provide a thermal barrier to zinc metal. Thus the temperature of the DSC pan is higher than of the zinc metal and the endothermic response appears at a higher temperature than the real temperature. The difference between the actual temperature of the sample and the detected temperature by the sensors increases as the heating rate increases. Thus, the small endothermic feature appears at higher temperature for a higher heating rate and seems as if it is kinetically controlled.

This endothermic feature vanishes within the range of observation on the second thermal cycle. If this feature were due to melting, it would reappear on second thermal cycling. However, even though it does not reappear, it does not necessarily indicate that it is not due to melting, because the feature corresponding to melting may vanish if:

(i) the very small nanoparticles were oxidized entirely to ZnO

(ii) the zinc crystals partly shrink to very small crystals, only a few nanometers in size, and partly agglomerate forming larger nanoparticles whose size range is similar with the mean size of the nanoparticles zinc sample, i.e. in the range of 30 –200 nm.

The second explanation suggests more reasonable explanation because the decrease in the size of nanoparticles is expected to shift its T_m to even lower temperature than the bulk and therefore show endothermic peak at an even lower temperature. This is not observed

over our corresponding temperature range. Instead, the small endothermic feature vanishes. On the contrary, increase in the size of nanoparticles would cause their melting endotherm to appear like the one observed for nanoparticles for the first cycle, but narrower. Since a double exothermic peak has been observed on cooling which corresponds to a two-stage crystallization of zinc nanodroplets, one expects two particle-size distributions within the sample. This aspect is further discussed in section 2.4.2.2.4.

2.4.2.2.3 Decrease of Enthalpy (ΔH) and Entropy (ΔS)

We now analyze the observed thermodynamic changes in the terms of the enthalpy and the entropy of both melting of nanocrystals zinc and crystallization of its nanodroplets. Formally, the change in enthalpy and entropy on change in temperature from T_1 to T_2 is calculated by using the following expressions,

$$\Delta H = \int_{T_1}^{T_2} C_p \, dT \tag{2.3}$$

$$\Delta S = \int_{T_1}^{T_2} C_p \, d\ln T \; . \tag{2.4}$$

Since the calorimeter measures the heat flow from which C_p is determined, we use the heat flow data to determine the enthalpy difference according to the relation,

$$\Delta H(T) - \Delta H(T_{ref}) = \int_{T_{ref}}^{T} \frac{1}{q}\left(\frac{\partial H}{\partial t}\right) dT \tag{2.5}$$

$$\Delta S(T) - \Delta S(T_{ref}) = \int_{T_{ref}}^{T} \frac{1}{q}\left(\frac{\partial H}{\partial t}\right)\frac{dT}{T}$$

$$\Delta S(T) - \Delta S(T_{ref}) = \int_{T_{ref}}^{T} \frac{1}{q}\left(\frac{\partial H}{\partial t}\right) d\ln T \tag{2.6}$$

where q is the heating rate.

Here, the enthalpy curves were obtained by integrating the heat flow from experimental results shown in figures 2.12(a) and (b), 2.13(a) and (b), and 2.14(a) and (b) against T and subtracting it from the enthalpy at a reference temperature as a baseline. The enthalpy of melting was obtained from the difference between the extrapolated value

of enthalpy of solid and that of corresponding liquid at T_m. The reference temperatures for calculation of the enthalpy of melting are 620 K for 10 K/min heating rate and 640 K for both 20 K/min and 40K/min heating rate. The enthalpy of crystallization was determined by using the same procedure, but the difference between the extrapolated value of the enthalpy of solid and that of corresponding liquid is taken at the onset crystallization temperature, T_{cryst}. The reference temperature for calculation of the enthalpy of crystallization is 700 K for all three cooling rates of 10 K/min, 20 K/min and 40 K/min. The details of the enthalpy of melting calculation are shown in figure 2.15.

The entropy curves are obtained by integrating heat flow plots obtained from experimental results shown in figures 2.12(a) and (b), 2.13(a) and (b), and 2.14(a) and (b) against ln T and subtracting it from the entropy at a reference temperature as a baseline. The entropy of melting was obtained from the difference between the extrapolated value of entropy of solid and that of corresponding liquid at T_m. The reference temperatures for calculation of the entropy of melting are 620 K for 10 K/min heating rate and 640 K for both 20 K/min and 40K/min heating rate. The entropy of crystallization was determined using the same procedure, but the difference is taken at the onset crystallization temperature, T_{cryst}. The reference temperature for entropy of crystallization calculation is 700 K for all three cooling rates of 10 K/min, 20 K/min and 40 K/min. The details of the entropy of melting calculation are shown in figure 2.16.

The results of the obtained enthalpy and entropy of melting and crystallization are given in Table 2.7 for 10 K/min heating and cooling rates, in Table 2.8 for 20 K/min heating and cooling rates, and in Table 2.9 for 40 K/min heating and cooling rates.

63
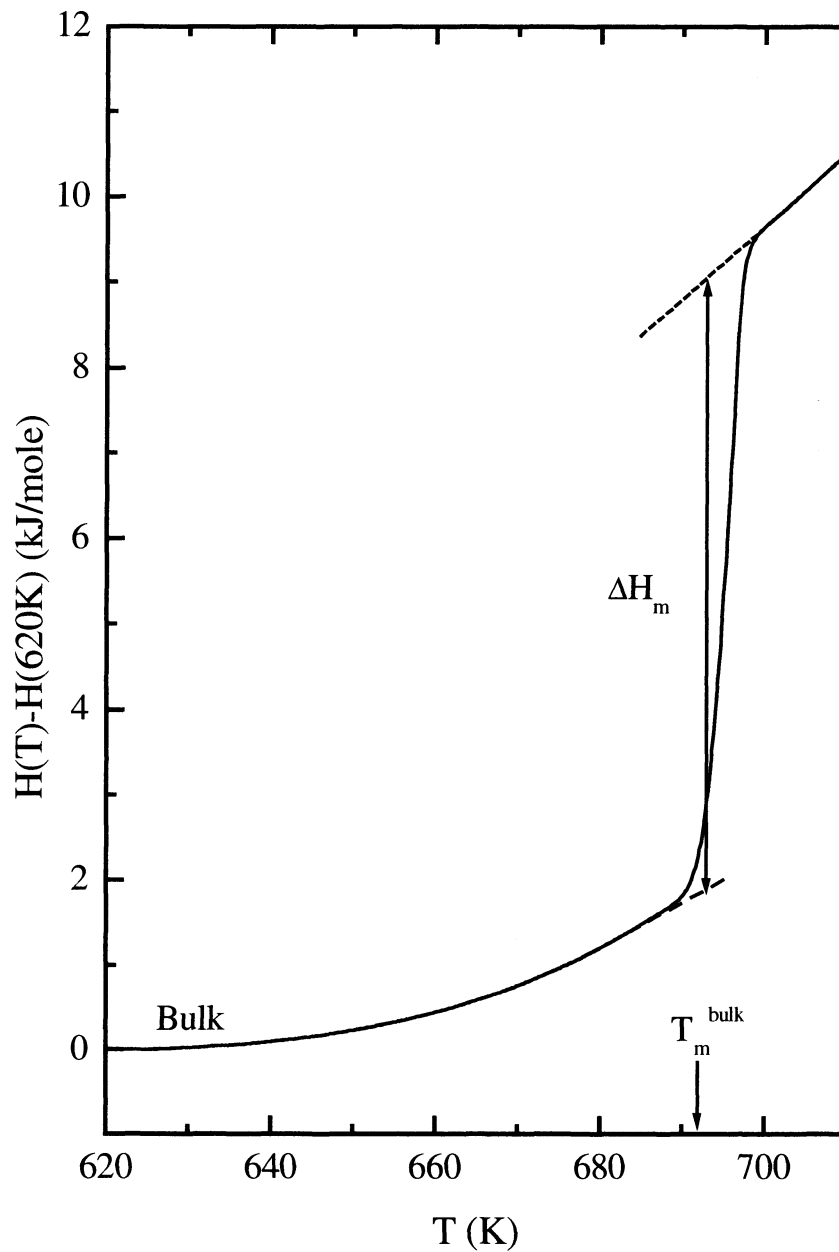
Figure 2.15 Details of calculation of enthalpy of melting for bulk zinc particle at 10 K/min heating rate. The solid line is the result of integration of heat flow against T with reference temperature of 620 K. The dashed lines are extrapolations of the solid and liquid states
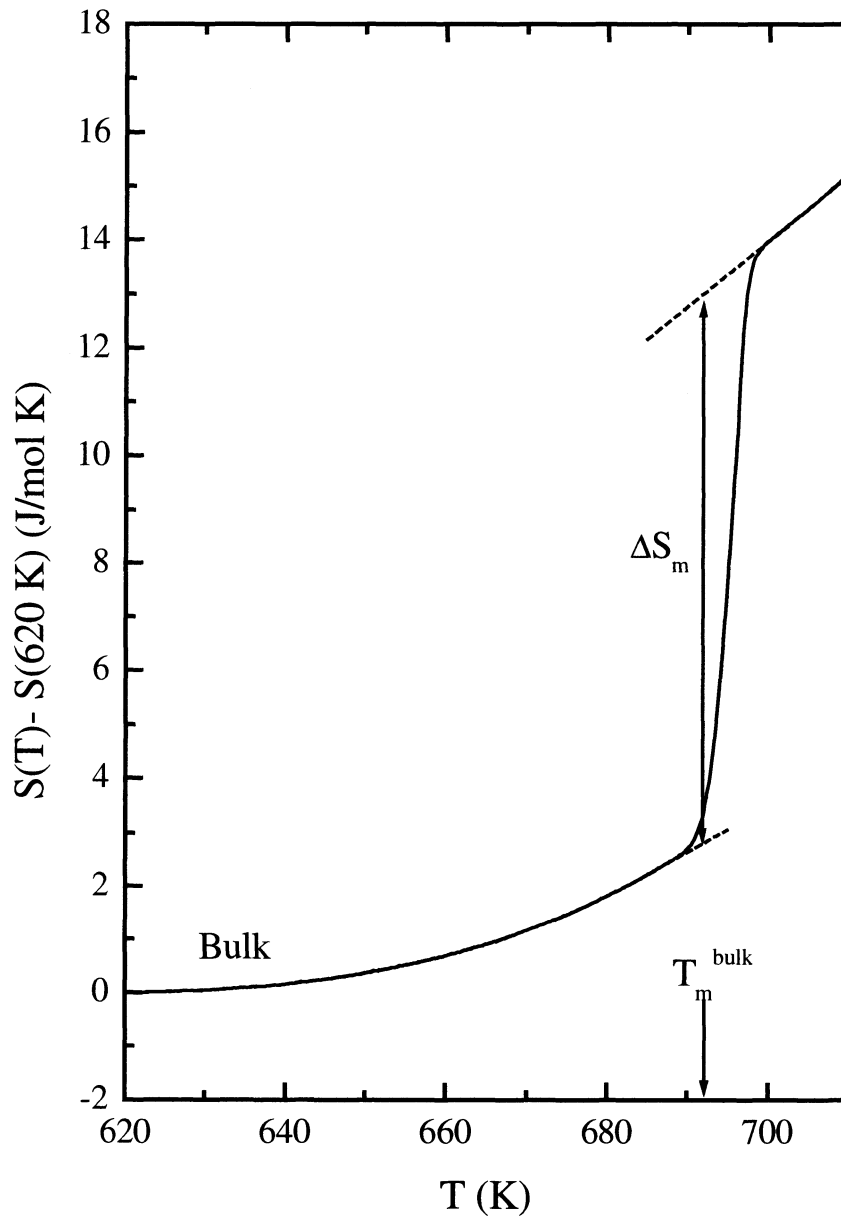
Figure 2.16 Details of calculation of entropy of melting for bulk zinc particle at 10
K/min heating rate. The solid line is the result of integration of heat flow
against ln T with reference temperature of 620 K. The dashed lines are
extrapolations of the solid and liquid states

65

Table 2.7 Enthalpy and entropy values of bulk and nanoparticles measured during the thermal cycling of the temperature as indicated by cycle number. Results are provided for both melting and crystallization on heating and cooling at the rate of 10 K/min

Cycle number	$\Delta H_m \pm 1\,\%$ (J/mole)	$\Delta S_m \pm 1\,\%$ (J/mole K)	$\Delta H_{cryst} \pm 1\,\%$ (J/mole)	$\Delta S_{cryst} \pm 1\,\%$ (J/mole K)
Bulk	7158 ± 71	10.2 ± 0.1	7047 ± 70	10.4 ± 0.1
1	5467 ± 55	7.9 ± 0.08	4588 ± 46	7.0 ± 0.07
2	5228 ± 52	7.6 ± 0.08	4331 ± 43	6.5 ± 0.06
3	4550 ± 45	6.6 ± 0.07	3409 ± 34	5.1 ± 0.05
4	3641 ± 36	5.2 ± 0.05	2757 ± 27	3.9 ± 0.04
5	2866 ± 29	4.1 ± 0.04	2172 ± 22	3.1 ± 0.03

Table 2.8 Enthalpy and entropy values of bulk and nanoparticles measured during the thermal cycling of the temperature as indicated by cycle number. Results are provided for both melting and crystallization on heating and cooling at the rate of 20 K/min

Cycle number	$\Delta H_m \pm 1\,\%$ (J/mole)	$\Delta S_m \pm 1\,\%$ (J/mole K)	$\Delta H_{cryst} \pm 1\,\%$ (J/mole)	$\Delta S_{cryst} \pm 1\,\%$ (J/mole K)
Bulk	7074 ± 71	10.1 ± 0.1	7064 ± 71	10.4 ± 0.1
1	5467 ± 55	7.8 ± 0.08	4384 ± 44	6.7 ± 0.07
2	5321 ± 53	7.5 ± 0.08	4367 ± 44	6.6 ± 0.07
3	5112 ± 51	7.2 ± 0.07	4172 ± 42	6.2 ± 0.06
4	4799 ± 48	6.8 ± 0.07	3965 ± 40	5.8 ± 0.06
5	4492 ± 45	6.4 ± 0.06	3773 ± 38	5.5 ± 0.06

Table 2.9 Enthalpy and entropy values of bulk and nanoparticles measured during the thermal cycling of the temperature as indicated by cycle number. Results are provided for both melting and crystallization on heating and cooling at the rate of 40 K/min

Cycle number	$\Delta H_m \pm 1\ \%$ (J/mole)	$\Delta S_m \pm 1\ \%$ (J/mole K)	$\Delta H_{cryst} \pm 1\ \%$ (J/mole)	$\Delta S_{cryst} \pm 1\ \%$ (J/mole K)
Bulk	7046 ± 70	10.0 ± 0.1	6995 ± 70	10.4 ± 0.1
1	5436 ± 54	8.0 ± 0.08	5089 ± 51	7.5 ± 0.08
2	5364 ± 54	7.7 ± 0.08	5042 ± 50	7.4 ± 0.07
3	5307 ± 53	7.6 ± 0.08	5012 ± 50	7.4 ± 0.07
4	5214 ± 52	7.5 ± 0.07	4938 ± 50	7.2 ± 0.07
5	5126 ± 51	7.4 ± 0.07	4852 ± 50	7.1 ± 0.07

In Table 2.7, ΔH_m and ΔS_m values for bulk zinc are 7158 J/mole and 10.2 J/mole K respectively. The values measured for different heating rates are within 1 %. The literature values [Grønvold and Stølen (1999, 2003)] of ΔH_m and ΔS_m are 7.07 kJ/mole and 10.2 J/mole K respectively. Therefore our measurement agrees with the bulk value from the literature. Table 2.7 shows that ΔH_m of nanoparticles zinc on heating in the first thermal cycle is 5.47 kJ/mole. This value is ~ 77 % of ΔH_m of the bulk zinc. Table 2.7 also shows that ΔH_m of nanoparticles continuously decreases on thermal cycling.

The decrease in the enthalpy of melting of nanoparticles with further thermal cycling can occur for two reasons:

(1) The amount of zinc metal in nanoparticles decreases as ZnO layer thickens and further consumes the zinc metal on thermal cycling. Therefore, the amount of heat needed for melting per gram of the sample is reduced.

(2) The heat capacity of nanoparticles zinc is higher than that of the bulk zinc. This would appear as a higher enthalpy of zinc nanoparticles. This view is illustrated in figure 2.17 where nanoparticles are shown to have higher enthalpy than the bulk material. The ~ 13% higher C_p of solid nanoparticles relative to solid bulk materials, as described in section 2.4.1, implies a higher slope of the NPs$_{(s)}$ enthalpy against

temperature curve relative to the Bulk$_{(s)}$ curve. Since we have no data of C_p liquid nanoparticles as function of temperature in figure 2.17, in one curve, NPs$_{(l), 1}$, it has been assumed that C_p of liquid nanoparticles is the same as that of liquid of bulk materials and in the second, NPs$_{(l), 2}$, it has been assumed to be higher. Both plots indicate that ΔH_m is lower for the nanoparticles than for bulk materials.
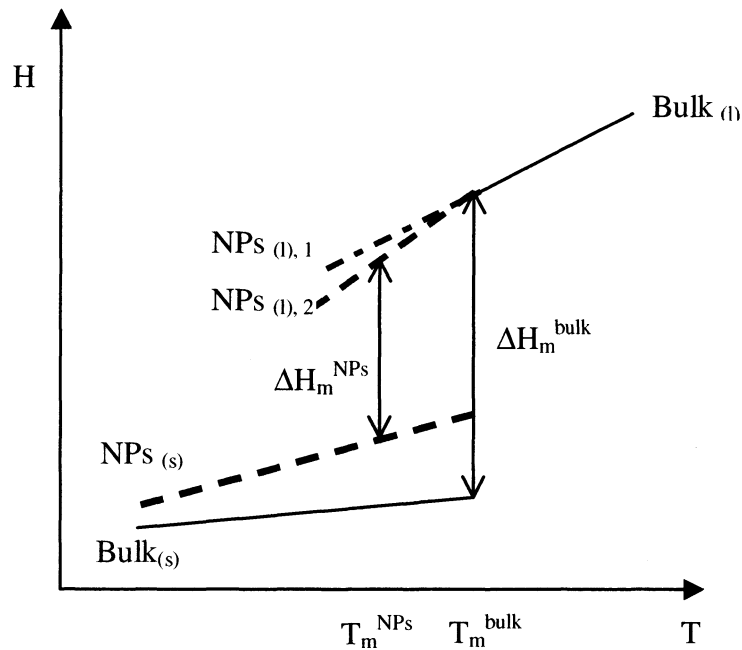
Figure 2.17 H vs. T diagram shows the decrease of enthalpy of melting as the melting temperature decreases due to reduction in particle size. Subscript (s) and (l) refer to solid and liquid state respectively. Solid lines represent the bulk, while the bold, dashed line the nanoparticles

As the size of the nanoparticles zinc decreases with decreasing amount of zinc metal on thermal cycling, the onset melting of nanoparticles would be lower than that of the bulk materials, $T_{m,bulk}$. The amount of heat needed for melting at a lower temperature would therefore be less than ΔH_m^{bulk} for melting of bulk particles at $T_{m,bulk}$. It is also known that when the enthalpy against temperature plot of a liquid has a finite slope of $C_{p(l)}$, which is higher than the corresponding slope for solid, $C_{p(s)}$, in the bulk state, the enthalpy of freezing will be reduced when freezing occurs at a lower temperature after

68

the liquid has supercooled. Yet, since the equilibrium melting, and not the supercooling, is concerned, this effect is not considered here. The decrease in ΔH_m for nanoparticles here refers only to the size effect, which need to be considered in two ways:

(i) the decrease in the equilibrium melting temperature, as the size of the nanoparticles decreases with decreasing amount of zinc metal on thermal cycling, and

(ii) the increase in the enthalpy of the nanoparticles due to their higher C_p. Moreover if C_p of nanoparticles was higher, their enthalpy would decrease with temperature more rapidly than those of bulk materials and this would also lead to a lower ΔH_m^{NPs}.

However, after the third cycle even though T_m of nanoparticles becomes relatively constant, their ΔH_m decreases further. This fact seems to contradict the Gibbs-Thomson formula, in which a constant T_m represents a constant particle radius, r, corresponding to constant amount of zinc metal in the sample and hence a constant ΔH_m. Therefore, it must be clearly understood that constant T_m does not necessarily indicate that the particle size distribution within the sample would also be constant. Rather, the constant T_m only indicates that the lowest size of nanoparticles in the distribution that melt first does not change, without ignoring the fact that conversion of zinc metal to ZnO persists. In brief, the decrease in the amount of zinc metal, shown by the decrease in ΔH_m, changes the particle size distribution without necessarily changes the size of zinc metal which would firstly melt.

As discussed in section 2.4.2.2.2, the non-uniform ZnO layer would repeatedly crack on subsequent heating cycles due to the hydrostatic pressure build-up allowing molten zinc of some nanoparticles to diffuse out of their ZnO shell and agglomerate with molten zinc of other cracked-shell nanoparticles. At the end of each heating cycle, some zinc metal particles decreased in size and other increased, both remaining were sealed with the re-formed ZnO shells, as depicted in figure 2.18 (b).
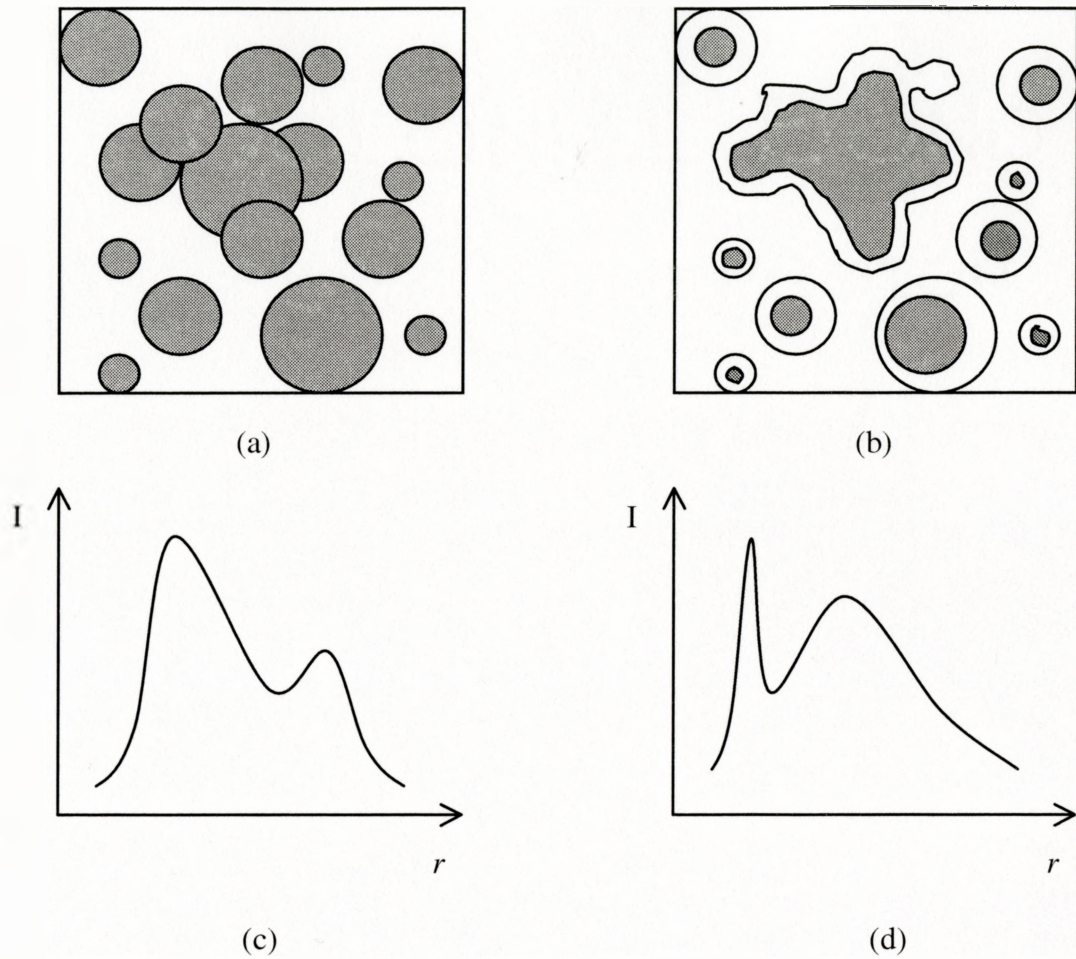
Figure 2.18 Evolution of nanoparticles zinc during thermal cycles. The initial condition of zinc nanoparticles is shown in (a) and their size distribution in (c). The post-heating condition of zinc nanoparticles is shown in (b) and their post-heating distribution in (d). The grey colour corresponds to zinc metal, while white colour corresponds to ZnO

For the very small zinc nanoparticles, the size of zinc crystals contained in the non-cracked ZnO shell would become relatively constant on further thermal cycling as the difficulties of oxygen to penetrate the ZnO layer increases. For the large zinc nanoparticles, the size of zinc crystals contained in the cracked ZnO shell would either,

(i) decreases further due to ZnO formation as oxygen from atmosphere penetrates deeper into the exposed zinc crystals through cracks on ZnO layer of the zinc nanoparticles, or

(ii) increases further due to agglomeration of zinc in molten state with other cracked-particles.

Finally, as shown in figure 2.18(c), the size distribution of zinc nanocrystals would continuously change as some zinc crystals shrink and some others grow so that it would end up in a different size distribution, as shown in figure 2.18(d). This change in size distribution of zinc nanocrystals can also be associated to the subsequent changes in the shape of double crystallization exothermic minima observed on cooling of nanoparticles. This is discussed in the next section.

2.4.2.2.4 Double Crystallization Exotherm of Zinc Nanoparticles

On cooling, double exothermic minima appear for the nanoparticles as shown in figures 2.12(B), 2.13(B) and 2.14(B). These double exothermic minima also indicate the size re-distribution of the crystallizing zinc nanodroplets, as described in the section 2.4.2.2.3.

Since the bulk sample shows only one exothermic minimum on cooling, the double exothermic minima for nanoparticles indicate two stages of crystallization of zinc nanodroplets encaged by the ZnO layer. The temperature range of the double exothermic minima becomes narrower with thermal cycling, as zinc metal is progressively consumed by ZnO formation, as shown by the data in Table 2.6. In figures 2.12(B), 2.13(B) and 2.14(B) for nanoparticles, the first minimum at higher temperature of higher intensity

eventually merges with the second one. At the end of thermal cycling, the depth of both minima becomes nearly equal one another.

The sharp, high intensity of the first crystallization minimum in figures 2.12(B), 2.13(B) and 2.14(B) for nanoparticles is mainly caused by large amount of nuclei of zinc nanodroplets readily formed due to the availability of free surfaces provided by the presence of ZnO shell. The free surfaces act as suitable sites for nucleation of zinc nanocrystals from zinc nanodroplet, so that the activation energy of nucleation is less than that of pure zinc nanodroplets alone without ZnO layer. Thus this first, high temperature minimum of the thermogram for nanoparticles is addressed as heterogeneous crystallization minimum, while the second minimum as homogeneous crystallization minimum.

The free energy of heterogeneous nucleation [Porter and Easterling (1992)] is given by,

$$\Delta G^{*}_{het} = \Delta G^{*}_{hom} \times S(\theta)$$

$$S(\theta) = (2 + \cos\theta)(1 - \cos\theta)^2 / 4 \tag{2.7}$$

where ΔG^{*}_{het} and ΔG^{*}_{hom} are the energy barrier of heterogeneous and homogeneous nucleation respectively, and $S(\theta)$ is the shape factor which depends on θ, the 'wetting' angle between the surface of the substrate and the nucleating substance. The low energy interface is favoured by a low value of θ, which corresponds to a good lattice matching between nucleating substance and the free surface.

In their study of the gas-sensing properties of ZnO, Lin et al. (2004) have shown a good epitaxial relationship between Zn and ZnO shell. They have concluded that ZnO has the same cell structure as Zn, which is hexagonal close packed structure, but the two differ in the unit cell parameters. The singular fringe spacing of high-resolution TEM of Zn was measured to be 0.24 nm while that of ZnO was about 0.28 nm. The difference of this 17 % of lattice mismatch, which is considered as semi-coherent interface, favours the heterogeneous nucleation by giving a significant value of shape factor, $S(\theta)$, which in

turn decreases the total activation free energy for nucleation of molten Zn according to equation (2.7).

The decrease in the total amount of zinc in the crystallizing nanodroplets as a result of oxidation becomes evident in the reduction of ΔH_{cryst}, the total area of exothermic minimum, with thermal cycling as presented in Table 2.7, Table 2.8 and Table 2.9. Figures 2.12(B), 2.13(B) and 2.14(B) for nanoparticles show that as ZnO layer thickens, the intensity of the first minimum decreases due to decreasing amount of zinc nanodroplets and that of the second decreases more. The increasing amount of ZnO in the sample results in suppression of the homogeneous type of crystallization and increasing tendency towards the heterogeneous crystallization. The distinction of heterogeneous and homogenous minimum becomes less clear as the total width of the double exothermic minima decreases with thermal cycling.

2.4.3 Model Experiments on Thermal Barrier Effect

In order to further investigate whether or not the double crystallization minima can be caused by the interruption of thermal conduction path by the shell of ZnO on nanoparticles zinc, another set of experiments were performed. In these model experiments, indium and low melting point pharmaceuticals were used instead of zinc nanoparticles and titania and alumina insulator layer were used instead of ZnO. In these experiments, two pieces of bulk indium were placed on top of another, with or without the insulator partition, in a DSC pan as shown in figure 2.19, as experimental study 1, 2, and 3. Thermal insulators used are VYCOR glass with diameter of 5 mm and thickness of 0.5 mm, and Al_2O_3 (alumina) powder. The DSC scans measured for 10 K/min heating rate and also 10 K/min cooling rate were obtained for each experiment. These scans for experiment 1, 2, and 3 are shown in figure 2.20(A), 2.20(B) and 2.20(C) respectively.
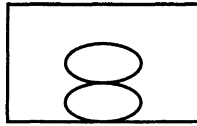
Experimental Study 1:   Experimental Study 2:   Experimental Study 3:
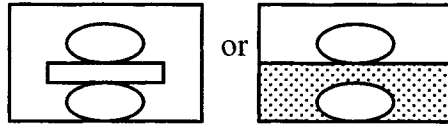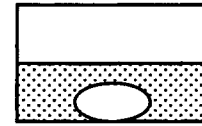
Figure 2.19 Different positions of indium, with or without the insulator partition, in a DSC pan

Experimental Study 1

The DSC scans of two pieces of indium stacked without partition in figure 2.20 (A) show a double endothermic peak due to melting that are very close to each other and a similar double exothermic minima due to crystallization. This means that the separation of particles, especially if the size of the particles is sufficiently large, even in absence of any insulating partition, will cause the endothermic peak and exothermic minimum to split as if it was a two-stage process. The sufficiently large particle, ~ 2 mm in diameter, causes thermal lag in heat conduction from heater to the sample during melting and from sample to the sensor during crystallization. First peak comes from the bottom particle that directly touches the DSC pans, while the second one corresponds to the top particle.
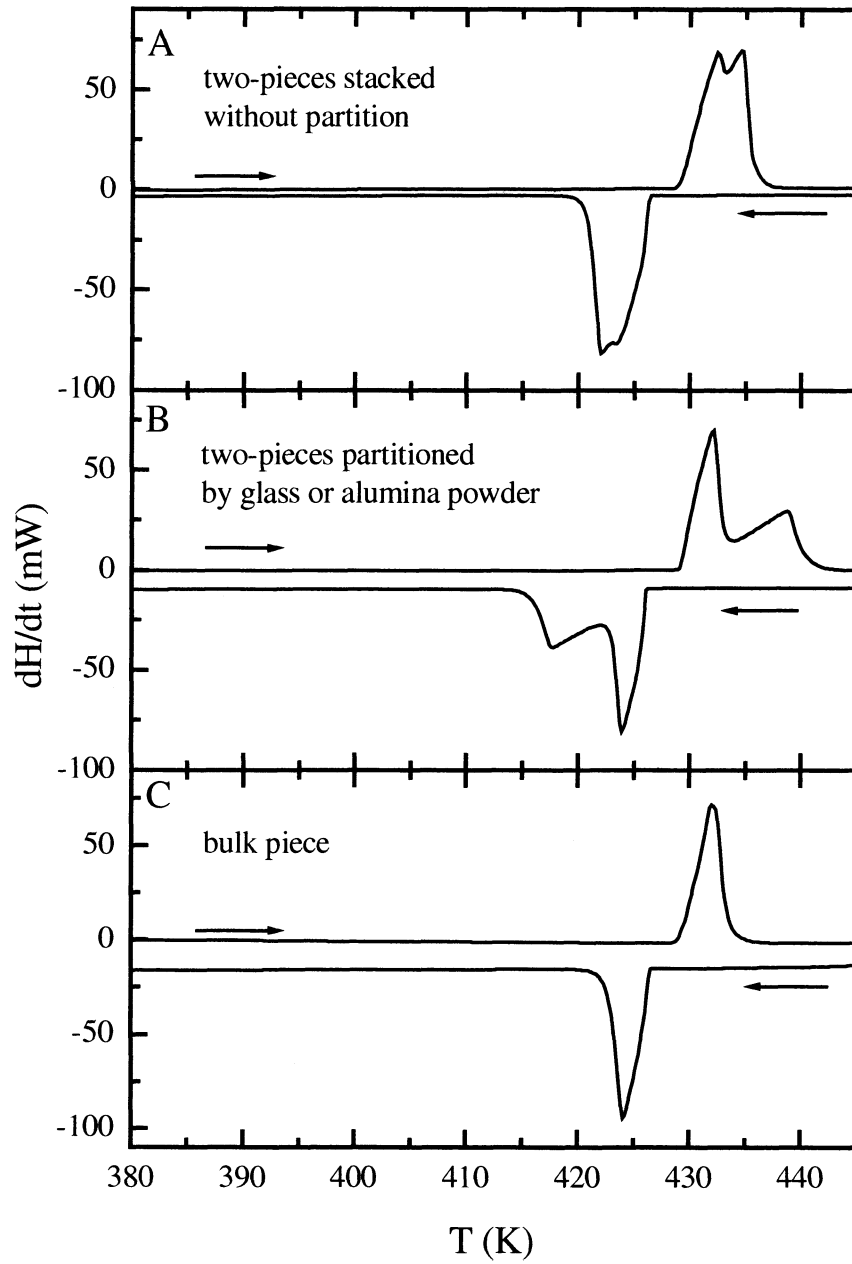
Figure 2.20 DSC thermograms on heating and cooling both at 10 K/min rate of experimental study 1, 2 and 3, respectively

Experimental Study 2

The DSC scans of two pieces of indium stacked with partition of VYCOR glass or alumina powder in figure 2.20 (B) show distinctly two endothermic melting peaks and also two exothermic crystallization minima which do not merge on thermal cycling. The first endothermic peak shows the melting of the bottom particle, while the second melting peaks shows the melting of the top one. The separation of the melting peak is due to the slow transfer of heat due to the presence of a thermal insulator. The glass or alumina acts as the heat barrier so that the heat conducted from heater to melt the sample is retarded and hence the melting process of the top particle occurs as if at a higher temperature. This explanation is also valid for the exothermic minimum due to the retarded heat release from the sample to instrument sensor.

In this condition, the splitting of the peak is caused by the presence of insulator between particles that acts as the heat barrier. Presence of insulator causes the endothermic effect due to melting of the insulated top particle to appear at a higher temperature and its exothermic effect due to crystallization to occur at lower temperature.

Experimental Study 3

The DSC scans of one piece of indium buried in alumina powder in figure 2.20 (C) show only one endothermic peak and one exothermic minimum, the same result as that obtained for indium alone. This indicates that no effect of thermal insulator surrounding the particle is observed as long as it maintains a good contact with DSC pan. This also shows that crystallization for bulk particles was not affected by the presence of insulator surrounding them. Analogue to Zn-ZnO system, the presence of ZnO outer layer in Zn bulk will have negligible effect towards the shape and position of the melting peak and crystallization minimum.

Therefore, the splitting of DSC endothermic peak or exothermic minimum are caused by either one or both of these following two occurrences:

(i) separation between quite large particles (~ 2 mm in diameter), and

(ii) presence of thermal insulator such as oxide between the metal particles.

Analogous of Thermal Barrier Effect in nanoparticles zinc with ZnO surface layer

The zinc nanocrystal encaged by ZnO layer shows DSC scan like that of a homogeneous dispersion of indium in alumina powder as depicted by Experimental Study 2. It is as if zinc crystal is dispersed in the ZnO matrix. However, the shape or position of the peaks in Experimental Study 2, as shown in figure 2.20(B), does not change with further thermal cycling because no interaction between indium and the insulator occurs. In contrast, an interaction occurs between zinc metal and ZnO layer in which the double crystallization exotherm merges and the width of exothermic minima decreases with thermal cycling.

Furthermore, in the Zn-ZnO system, the concentration of ZnO in the nanoparticles sample was not as much as that of alumina in Experimental Study 2. Hence, even though the effect of thermal barrier of ZnO is present and its effect continuously increases with thermal cycling, it is much less than the effect of alumina in Experimental Study 2, so that the presence of ZnO shell acting as heat barrier can be neglected. This thickness is also of course very small, of nanometer dimensions, in comparison with the thermal barrier thickness in the indium experiments.

2.4.4 Ball-milling Experiments

To further support the conclusion for heterogeneous nucleation and growth of zinc metal in the nanoparticles sample, another series of experiments was performed by mixing bulk zinc particles and alumina powders. The aim of these experiments, which are described below, is to envisage what is happening during the heating and cooling

processes when zinc is homogeneously spread within the insulator matrix. In these experiments the zinc particles were ball-milled with alumina powder by using 8000 Spex vibration mills for the same period of three hours. Afterwards, DSC scans were performed twice for each sample at 20 K/min rate on both heating and cooling. A correction factor of 3.8 K was applied for 20 K/min heating and cooling rates due to the thermal lag of instrument.

In the first experiment, an unknown amount of zinc metal and alumina were ball milled for three hours. The DSC scans were performed over the temperature range of 373-708 K. The corrected DSC thermograms are shown in figure 2.21. These show two endothermic peaks over 476-557 K range followed by a main double endothermic melting peak of Zn with $T_m \sim 677.6$ K. This T_m value is surprisingly lower than that of pure Zn nanoparticles purchased from the manufacturer. This indicates that nanocrystals zinc formed within alumina matrix by ball milling is smaller in size than the as-received nanoparticles. The splitting of the endothermic melting peak is caused by contribution of alumina acting as heat barrier. As there is no interaction between zinc and alumina in the sample on thermal cycling, unlike one in Zn-ZnO sample in which the conversion of Zn to ZnO continuously persists, the splitting of endothermic peak remains unchanged in the second thermogram.

The exothermic minimum of zinc-alumina system is broad and indicates merging of two exotherms. However, this merger of two exotherms does not suggest occurrence of both heterogeneous and homogeneous crystallizations. Later, the thermograms for sample #4 shown in figure 2.24 for the Zn-TiO$_2$ mixture shows more clearly two exothermic minima indicating two crystallization mechanisms. The first, sharp, high intensity minimum corresponds to the heterogeneous crystallization because it is faster, and the second broad, low intensity minimum corresponds to homogeneous crystallization. This feature is similar to that observed for Zn-ZnO system, and therefore the occurrence of both heterogeneous and homogeneous crystallization in nanoparticles zinc sample is confirmed.

The same sample was studied over the temperature range of 403-603 K and the corrected thermograms are presented in figure 2.22. There are two endothermic peaks in the first scan over 476-557 K temperature range, the same as those obtained from the first sample in figure 2.21. A small exothermic crystallization minimum appears at ~ 477 K on cooling. In the second heating scan, the double endothermic peaks vanish and are replaced by one small endothermic peak. This indicates that the double peaks on heating in the first scan correspond to irreversible process instead of melting. Since the recovery and re-crystallization processes are exothermic, the possibility that those peaks correspond to recovery and re-crystallization of zinc is eliminated. It seems that these endothermic peaks correspond to external effect and are not characteristic of the ball-milled material itself.
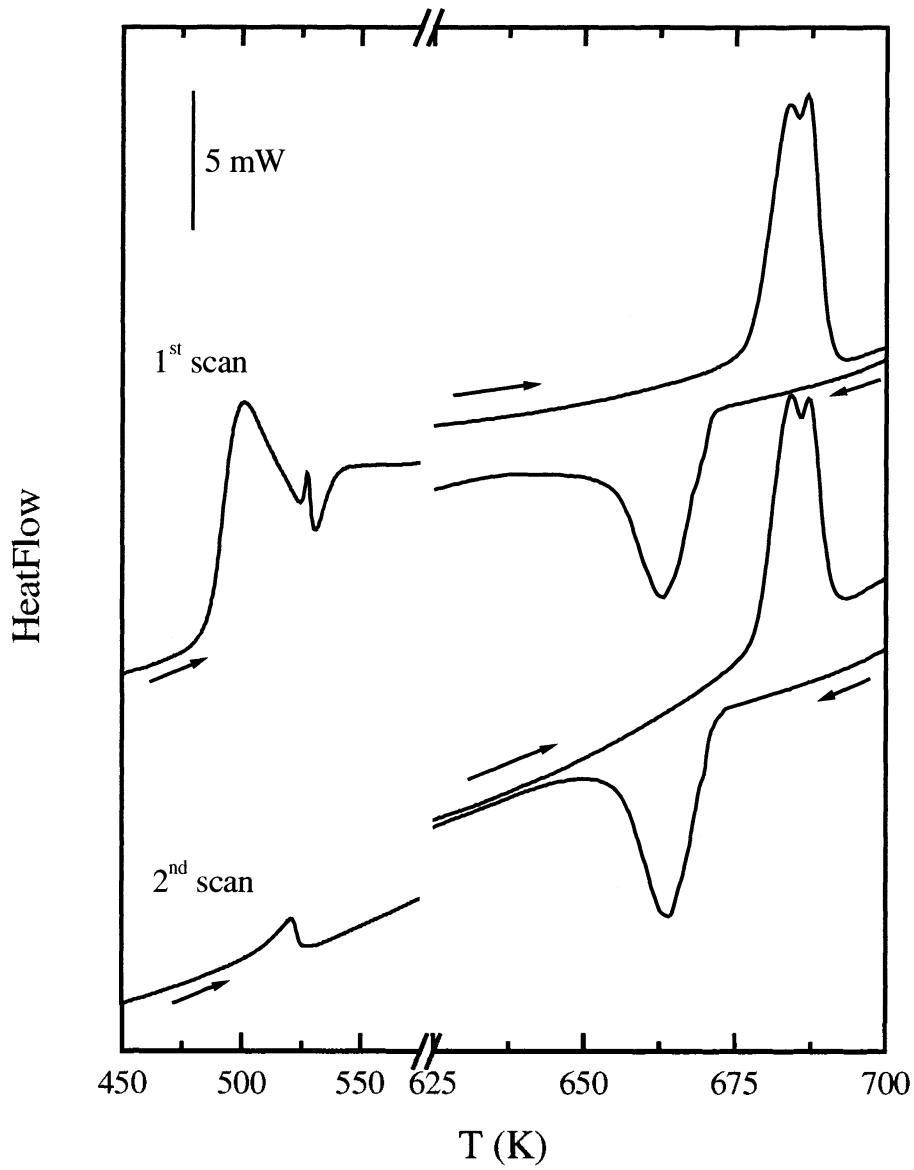
Figure 2.21 DSC thermograms of zinc metal and alumina milled for three hours
measured over the temperature range of 373-708 K
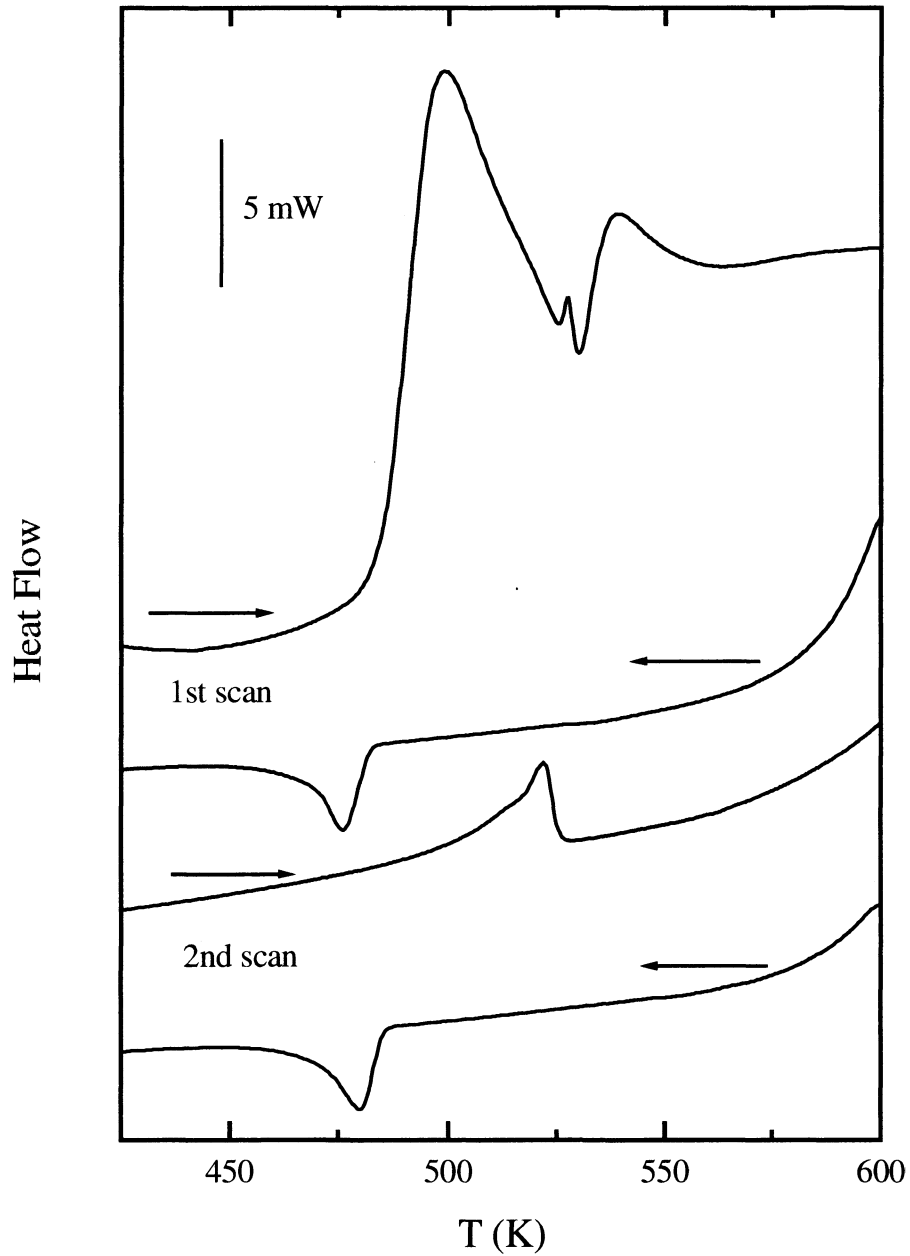
Figure 2.22 DSC thermograms of zinc metal and alumina ball-milled for three hours measured over the temperature range of 403-603 K

In the second experiment, pure alumina were ball-milled for three hours in order to further investigate whether or not the feature over the 476-557 K range is due to the presence of alumina. The DSC scans were performed over 403-603 K temperature range. The DSC thermograms are shown in figure 2.23. The first heating scan of DSC thermogram shows a slightly broad endothermic peak begins at ~ 523 K, which disappears in the second scan. No exothermic minimum due to crystallization is observed on cooling in both first and second scans. This suggests that ball-milled pure alumina contributes very little to the effects observed on heating and nearly no effect on cooling. In brief, there is no contribution of the presence of alumina in the double endothermic features described for zinc-alumina sample.

Takacs (1993), in his study of metal-metal oxide systems for nanocomposite formation by reaction milling, has presented the driving force energies of some oxidation reactions. He has described that,

Reaction	q (kcal/mole of oxygen atoms in the reaction products)
$3Fe_3O_4 + 8Al \rightarrow 9Fe + 4Al_2O_3$	-68
$Fe_3O_4 + 4Zn \rightarrow 3Fe + 4ZnO$	-17

and by combining both reactions, the result is as follows:

$$Al_2O_3 + 3Zn \rightarrow 2Al + 3ZnO \qquad q = + 4.25 \text{ kcal/mole.} \qquad (2.8)$$
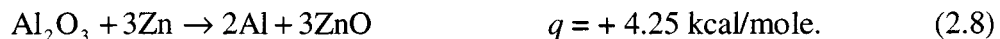
Therefore, on heating in DSC pans, zinc may interact with Al_2O_3 forming Al and ZnO by-products. This type of reaction is endothermic as indicated by positive energy value in equation (2.8), which agrees with the endothermic peaks observed in the DSC thermograms for zinc-alumina samples shown in figures 2.21 and 2.22.
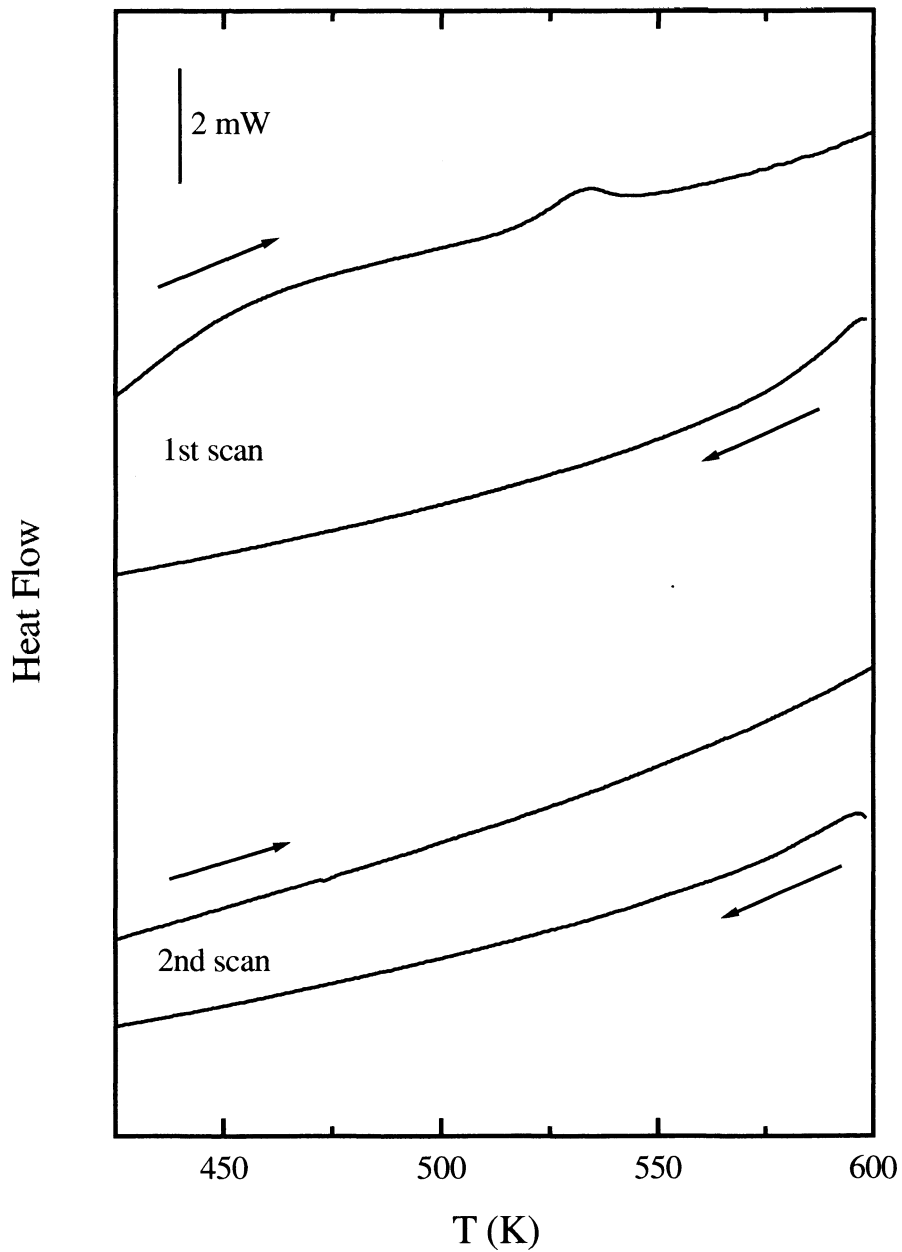
Figure 2.23 DSC thermograms of three hours ball-milled alumina measured over the temperature range of 403-603 K

Since the interaction between zinc and the oxide matrix occurred when alumina was used as the matrix, a third experiment was prepared in which TiO_2 was then used in place of alumina. The DSC scans were performed over the temperature range of 373-708 K and the thermograms are shown in figure 2.24. The three-hour milled Zn metal shows T_m of ~ 678 K, lower than literature value of bulk zinc, 692.7 K, which confirmed the formation of nanoparticles zinc by ball-milling procedure. In the first thermal cycle, the endothermic melting peak of zinc splits into two peaks on heating and the exothermic crystallization minimum also splits into two minima on cooling. The split of exothermic minimum observed is more clearly distinguished than that observed in $Zn-Al_2O_3$ system. On both heating and cooling in the second thermal cycle, the endothermic melting peak and the exothermic crystallization minima begin to merge.

The results from the three experiments have provided a more detailed picture of the process occurring in the Zn-ZnO system, especially regarding the double crystallization minima. The splitting of the peaks can occur both on heating and cooling. The split of either the endothermic peak or the exothermic minimum correspond to the presence of the metal oxide matrix, which acts as:

- A thermal insulator between the sample and the heat source and between the sample and the sensor of the instruments. The clear splitting of the peak as a function of fraction of the corresponding particles will be shown later in a model experiment using different fraction of pharmaceutical and oxide matrix as the samples. The thermograms of the mixture shown in figure 2.25 show that the splitting of melting peak occurring due to the presence of insulating matrix is possible when the fraction of oxide matrix is less than or equal to that of the metal particles. As the fraction of oxide increases, the thermal barrier effect becomes excessive, and hence the broadening instead of the splitting of the peak is observed.

- A promoter for heterogeneous crystallization on solidification of molten metal during cooling process. The oxide provides free surface and thus lowers the activation energy of solid phase nucleation. As long as there is no interaction between metal and metal oxide matrix, the split of the peak would remains unchanged with thermal

cycling. In the Zn-ZnO system, in which the reaction of formation of ZnO from Zn occurs progressively more on thermal cycling, the crystallization peaks becomes narrower and the crystallization shifts towards the heterogeneous mechanism.
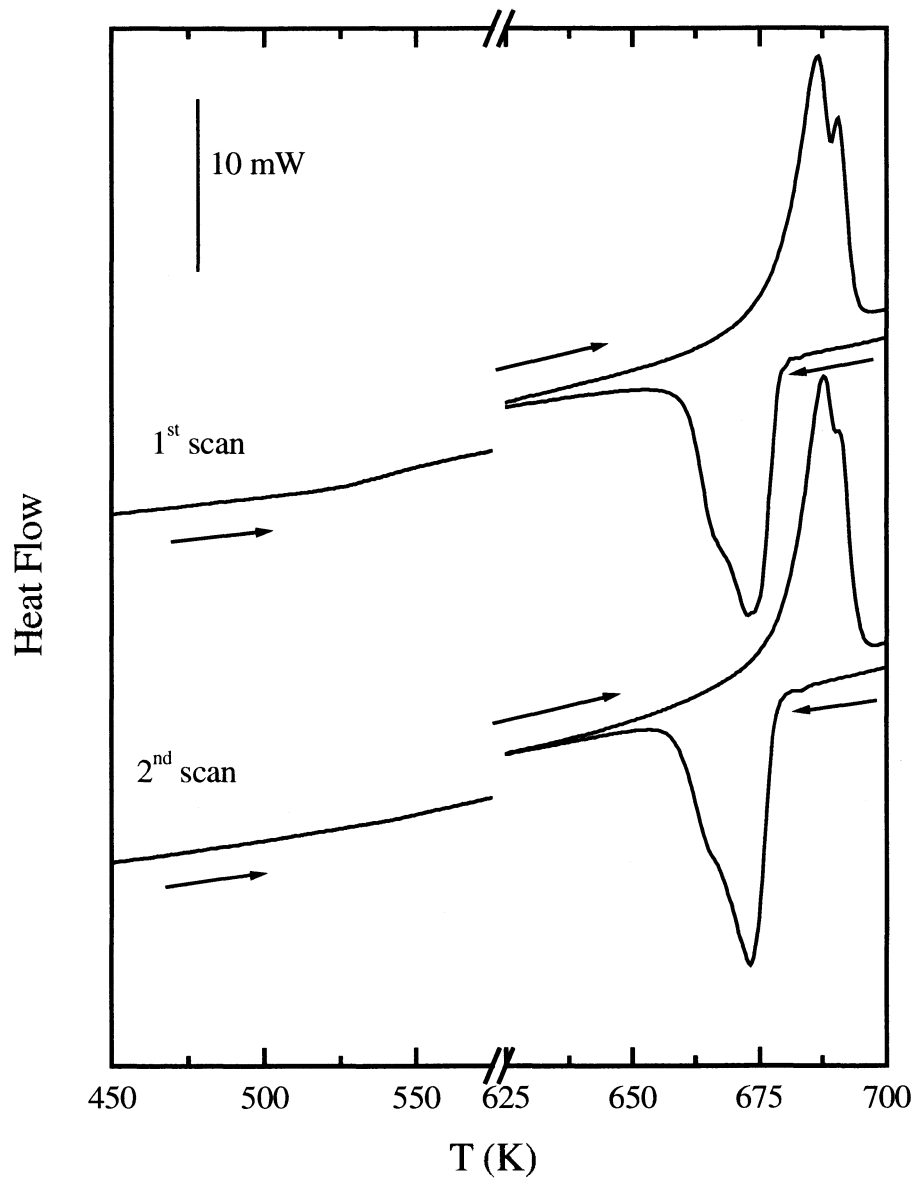
Figure 2.24 DSC thermograms of Zn metal and TiO_2 mixture ball-milled for three hours

Finally a model experiment was performed on a low melting point material, aspirin, by mixing it manually with TiO_2. The purpose of this model experiment is to investigate the effect of the homogeneously mixed matrix towards the shape and position of the melting peaks and to determine the effect of the fraction of the dispersed particles to the matrix. The DSC scans were performed over the temperature range of 353 - 438 K at 10 K/min heating rate and the thermograms are shown in figure 2.25.

The mixtures of aspirin and titania were taken in the 1:4 and 1:1 weight ratio. Both mixtures show melting of aspirin at about 413 K. However, the 1:4 aspirin to titania mixture shows only broadening of melting peak on heating, while the 1:1 mixture shows a merged double melting peaks. This confirms the interpretation for previous zinc-titania sample, that the fraction of substances in the mixture would affect the shape of the peak in DSC thermogram. The splitting of the peak is not only dependent on the thermal lag caused by insulating effect, but also on the fraction and distribution of particle size in the sample. The higher fraction of corresponding particles towards that of the matrix shows the splitting of peak rather than broadening. When the fraction of the material relative to the oxide becomes extremely small, the exothermic peak becomes smaller and splitting or broadening becomes unobservable.
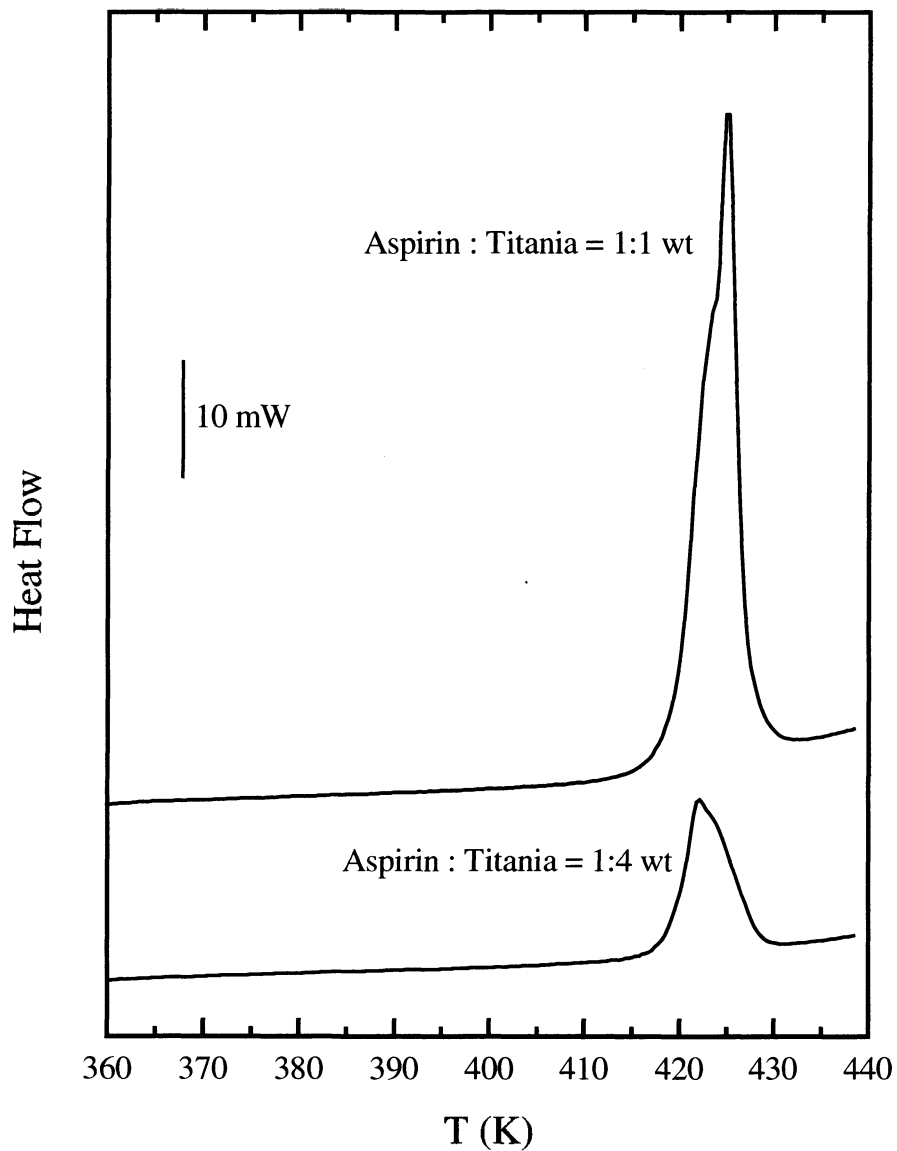
Figure 2.25 DSC thermograms of Aspirin-TiO_2 mixture at 10 K/min heating rate
measured over the temperature range of 353 - 438 K

2.5 Debye Temperature Calculation for Disordered Surface Layer on Zinc Nanoparticles

We now investigate why heat capacity of zinc nanoparticles differs from that of bulk zinc. As described in Section 1.2.1, the structure of a nanoparticle consists of an ordered crystalline core region and a disordered surface region. Therefore, it is expected that the Debye temperature of zinc nanoparticles would differ from that of bulk zinc due to the difference in frequencies of disordered surface atoms and of crystalline core atoms. The average Debye temperature of nanoparticles zinc can be weighted as the sum of Debye temperature of the crystalline core, which is the same as that of bulk, and that of the disordered surface as shown by equation (2.9) below,

$$\theta_D^{NPs} = \theta_D^{int} X^{int} + \theta_D^{surf} X^{surf} \tag{2.9}$$

where θ_D^{NPs}, θ_D^{int} and θ_D^{surf} are the Debye temperature of nanoparticles, of interior or core region, and of surface region respectively, and X^{int} and X^{surf} the volume fraction of the interior and surface regions respectively.

As mentioned in section 1.2.1, the thickness of disordered surface region, δ, is about two atom dimensions or four times its atomic radius. The atomic radius of zinc is 0.137 nm, hence the δ value would be 0.548 nm.

From histogram obtained from TEM observation described in section 2.3.1, the size range of nanoparticles zinc is between 30 and 120 nm. Thus, the average particle size is 75 nm. Using an average radius of nanoparticles zinc of 37.5 nm, the volume fraction of interior region can now be calculated by using the formula,

$$X^{int} = \left(1 - \frac{\delta}{r}\right)^3 \tag{2.10}$$

This calculation gives X^{int} value of 0.9568. As X^{surf} equals to 1- X^{int}, hence X^{surf} value is 0.0432.

As described in section 2.2.1, the heat capacity measurement at 330 K gives a value of 30.02 J/mole K for nanoparticles zinc, corresponds to C_p^{NPs}, and of 26.62 J/mole

K for bulk zinc corresponds to $C_p{}^{\text{int}}$. The law of mixing can now be applied to calculate the $C_p{}^{\text{surf}}$ at 330 K as follows,

$$C_p{}^{\text{NPs}} = C_p{}^{\text{int}} X^{\text{int}} + C_p{}^{\text{surf}} X^{\text{surf}} \tag{2.11}$$

$$30.02 = (26.62 \times 0.9568) + (0.0432\ C_p{}^{\text{surf}})$$

and $C_p{}^{\text{surf}}$ value obtained is 105.3 J/mole K.

Chen and Sundman (2001), in their study of Debye temperature of crystalline structures, have given high-temperature Debye temperature values of various elements obtained by fitting to the experimental entropy data with a model, taking electronic, anharmonic and magnetic contributions into account. They have given a high-temperature θ_D value of 225 K for bulk zinc. According to Debye T^3 law,

$$C_p = 1943\left(\frac{T}{\theta_D}\right)^3 \tag{2.12}$$

thus the Debye temperature corresponding only to the surface region of the nanoparticle, $\theta_D{}^{\text{surf}}$, at 330 K can be calculated by using,

$$\frac{C_p{}^{\text{int}}}{C_p{}^{\text{surf}}} = \frac{1943\left(330\Big/\theta_D{}^{\text{int}}\right)^3}{1943\left(330\Big/\theta_D{}^{\text{surf}}\right)^3} \tag{2.12 a}$$

$$\frac{C_p{}^{\text{int}}}{C_p{}^{\text{surf}}} = \left(\frac{\theta_D{}^{\text{surf}}}{225}\right)^3 \tag{2.12 b}$$

The $\theta_D{}^{\text{surf}}$ value obtained for our zinc nanoparticles by using the previously measured bulk heat capacity (26.62 J mol^{-1} K^{-1}) and calculated surface heat capacity (105.3 J mol^{-1} K^{-1}) data in equation 2.12 b is 142.26 K. Since $\theta_D = h\ \nu_D/k$ where h is Planck's constant, k is Boltzmann's constant and ν_D is the Debye frequency, which is inversely proportional to λ, the amplitude of lattice vibration, the ratio of λ of surface region to that of interior region in nanoparticle zinc is,

$$\frac{\lambda^{\text{surf}}}{\lambda^{\text{int}}} = \frac{\theta_D{}^{\text{int}}}{\theta_D{}^{\text{surf}}}\ . \tag{2.13}$$

The ratio of λ^{surf} to λ^{int} obtained is 1.548, suggesting that the vibrational amplitude of the lattice in surface region is approximately 55 % larger than that in interior region of nanoparticles. The large difference in the amplitude of lattice vibration between the surface and interior region is due to the large excess volume of surface region. This excess volume then contributes to configurational entropy of nanoparticles as for a disordered structure and increases the total heat capacity, for example here is zinc nanoparticles, whose C_p of is ~ 13 % higher than that of their bulk particles at the temperature range of 323-373 K.

2.6 Conclusion

The foregoing studies lead to these following conclusions:

1. The heat capacity of nanoparticles zinc is ~ 13 % higher than that of bulk zinc in temperature range of 323-373 K. Calculations based on the Debye theory show that the higher C_p value of nanoparticles is attributable to ~ 55 % greater amplitude of atomic vibrations of the surface atoms. Consequently, the difference in the atomic packing density between the core and surface region of nanoparticles increases the volume occupied per atom and increases also the coefficient of thermal expansion of the surface layer.

   The Debye frequency of the surface layer of nanoparticle is about half of that of the crystalline core. The lower Debye frequency of surface lead to higher entropy of the nanoparticles than the bulk. Accordingly, the total entropy increases as the size of nanoparticles decreases.

2. The melting point of nanoparticles zinc is lower than that of the bulk for several reasons. This appears to be consistent with the Gibbs-Thomson equation but it also requires that the increase in the entropy of the nanoparticles over the bulk phase, which has been neglected in the Gibbs-Thomson equation, be included. The heat capacity difference between the nanoparticles and the bulk materials confirms this.

3. The enthalpy of melting of nanoparticles zinc is ~ 77 % of that of bulk zinc and the entropy of melting of nanoparticles zinc is also smaller than that of bulk zinc. Both are determined from the melting endotherm. These are also evident in the independently determined higher heat capacity of solid nanoparticles relative to the bulk materials and the same or higher heat capacity of nanodroplets.

   Both enthalpy and entropy of melting further decreases with further thermal cycling. This occurs because the size of the nanoparticles zinc progressively decreases as a result of partial conversion to ZnO on thermal cycling. This causes a further reduction in the melting point and the enthalpy of melting. Hence both the melting point and enthalpy of melting becomes further lower than the corresponding values for the bulk.

4. The small endothermic feature observed on the first heating of zinc nanoparticles corresponds to the melting of the smallest particles in the nanoparticles aggregate. This peak vanishes on second and further thermal cycling partly because its melting temperature is far below the bulk's melting temperature and largely due to the small and undetectable heat flow signal.

   The shift of the lower temperature endotherm toward a higher temperature on increasing heating rate is caused by the thermally-insulating ZnO layer on the surface of nanoparticles. The effect of thermal barrier has been confirmed by the model experiment in which a low melting compound bulk-indium was embedded in alumina matrix. This shows the splitting of melting peak into two endotherms whose separation increases as the thickness of the separation increases.

5. A double crystallization minima was observed on cooling of nanodroplets. This shows a two-stage crystallization of nanodroplets, which results from heterogeneous nucleation on the ZnO surface layer and homogeneous nucleation in the core of the nanodroplets.

   In addition to acting as a thermal barrier, ZnO provides free surfaces suitable for heterogeneous nucleation of solid nanoparticles zinc from the molten state. Consequently, the activation energy for heterogeneous nucleation needed is reduced so that crystallization of zinc metal in ZnO-encaged nanodroplets can occur faster than that of pure zinc alone. As ZnO layer thickens on thermal cycling, the amount of available molten zinc decreases. Therefore, the two well-separated crystallization exotherms tend to become less separated.

Chapter 3. Formation of Nanocrystals in a Matrix and a Production Technique of Nanodrug Samples

3.1 Introduction

We now describe a general technique for producing nanocrystals in a matrix, with particular reference to the formation of nanodrugs – a subject of much current interest. The fact that novel properties of a material can be achieved by reducing its size to nanoscale is potentially useful for pharmaceuticals materials. Such nano-scale pharmaceuticals would have high surface to volume ratio that would enhance the solubility, bioavailability, reactivity, etc. of a drug [Mumper et al. (2003), Chen et al. (2004), http://nano.cancer.gov (2005)]. These novel properties improve the quality of the drugs itself, as well as the means of delivery of other drugs to a specific cells or tissue layers of organs [Fattal and Vauthier (2002)]. Furthermore, the higher solubility and reactivity of the drugs can increase the effectiveness of the drugs to be absorbed by the body.

Fattal and Vauthier (2002) have presented a review of some of the pharmaceutical applications of nanoparticles as drug delivery systems, which were considered to be highly suitable for human applications, as follows:

1. Intravenous administration

   Nano-scale drugs are expected to have the ability of achieving tissue targets and to enhance the intracellular penetration of drugs. Consequently, they can increase the effectiveness of inhibiting the malignant cancer cells as well as reduce the toxicity of a drug because of reduced accumulation in organs where the most acute toxic effects are exerted.

2. Subcutaneous/intramuscular administration

   This type of administration is mainly for the delivery of peptides and vaccines which allows the slow release of the entrapped drugs, therefore reducing the number of

administrations, increasing the blood half-life of the active drug and finally, in some cases, reducing the side effects.

3. Oral route

There have been abundant reports from various independent workers showing evidence of absorption of particulate systems by the gastrointestinal tract. However, the oral absorption of nanoparticles of drugs remains a controversial issue.

4. Oral delivery of peptides and proteins and vaccines

In nano-capsules, their surfaces act as promoters of absorption thus improving and prolonging the therapeutic effects of the peptides after administration by the oral route.

5. Ocular delivery

The conventional ocular dosage forms exhibit extremely low bioavailability. Limited absorption of the drug through corneal barrier is increased either by improving the pre-corneal residence time and/or penetration ability of the active ingredient by utilizing nano-liposomes and nano-capsules.

Recently, there has been a thorough review of techniques to produce organic or inorganic nanoparticles [Cushing et al. (2004)] by co-precipitation, chemical vapor deposition, sol-gel processing, electrodeposition, mechano-chemical milling, microemulsion, biomimetic, etc. In this thesis, a new and simpler way for producing nano-scale materials is introduced. It utilizes a nanoporous polymer matrix. This polymer matrix is poly-2(hydroxyethyl)methacrylate, abbreviated as polyHEMA. Johari and co-workers have studied nano-confined water, aqueous solutions in this polymer and have developed it for ocular delivery of antibiotic drug.

Hill et al. (2000) have stated that polyHEMA and its copolymers have been suitable for numerous medical applications due to their acceptable biocompatibility [Wichterle and Lim (1960), Choudhary and Varma (1983), Jeyanthi and Rao (1990)]. This polymer has also been identified as having potential for use in controlled release

95

drug delivery systems [Martin et al. (1983), Peppas et al. (1987), Tinghe et al. (1987)]. This polymer has been used for construction of soft contact lens.

Here we develop a technique for producing nano-crystalline pharmaceuticals in a polymer matrix. For this purpose, we use polyHEMA, which contains nanopores with diameter of 50 nm as a matrix to form pharmaceuticals nanocrystals. This is done by first diffusing the pharmaceuticals solution into a dried polymer, which swells as its nanopores are filled with the solution. The swollen polymer is then dried, which leaves crystals of size much smaller than the pore size in the polymer matrix.

We use benzoic acid, salicylic acid and methyl-4-hydroxy benzoate (methyl paraben). These pharmaceuticals are chosen because of their high solubility in ethanol, which was used as a solvent, their low melting point and their non-reactivity with the polymer matrix.

3.2 Experimental Methods

3.2.1 Sample Preparation

Benzoic acid, salicylic acid and methyl paraben with purity >99.9% in crystalline state were purchased from Sigma-Aldrich chemicals. The samples were stored in tightly closed containers with silica gel in order to prevent the moisture contamination of the samples.

The polyHEMA samples with the maximum capacity of water absorbance of 68% weight were obtained from SNOFLEX (Smith & Nephew Optics, London), one of the leading contact lens manufacturers. The polyHEMA hydrogel, which had been previously immersed in distilled water and swollen by filling its pores by water, was cut to 3 mm × 2 mm × 1 mm dimensions sample for DSC experiment and to 10 mm × 7 mm × 5 mm dimensions sample for X-ray Diffraction experiment. Finally polyHEMA was dried in a convection oven at 333 K-348 K for at least ten hours to remove all nano-confined water.

3.2.2 DSC Experiments

After the initial sample preparation was completed, the oven-dried polyHEMA was weighed to determine its dry mass, m_1. Crystalline pharmaceutical was dissolved in ethanol until a supersaturated solution was obtained. The weighed dry polyHEMA sample was then immersed in the supersaturated solution and kept immersed for at least ten hours, thus allowing sufficient time for the solution to diffuse into the nanopores of polyHEMA. The diffusion of the solution into the polyHEMA nanopores was evident from the swelling of the sample up to nearly two times of its original dimensions. Thereafter, the immersed polymer containing nano-confined solution was heated in a convection oven at 333 K-343 K for ten hours and all the ethanol (boiling point 351.5 K) was evaporated from the polymer. The sample after this procedure shrank to dimensions larger than the original dried sample.

97

The dry polyHEMA containing nanocrystals was then placed in a DSC aluminum pan with lid of known weight, $m_{pan+lid}$, and then it was re-weighed, m_2. This sample was then thermally scanned using Perkin Elmer Pyris Diamond DSC in one set of experiments and DSC Q100 TA Instruments in the second set of experiments. The scans were performed using either 10 K/min or 20 K/min both heating and cooling rates over the necessary range of temperature, determined from T_m of the pharmaceutical. The difference between the weight of dry polyHEMA containing nanocrystals, $m_2 - m_{pan+lid}$, and the initial weight of dry polyHEMA, m_1, is the net weight of pharmaceutical nanocrystals in the polymer.

The DSC scans of (i) polyHEMA with nano-confined ethanol, (ii) pharmaceutical in ethanol solution, and (iii) pure pharmaceutical were also performed in order to investigate whether or not the pharmaceutical itself reacted with the solvent and/or the polymer matrix.

3.2.3 X-ray Diffraction Experiments

Similar to the procedure for preparing DSC samples, the sample for x-ray diffraction experiment was kept immersed in supersaturated solution for at least 18 hours, a longer period because of its larger dimensions. Thereafter, the swollen polyHEMA containing nano-confined solution was taken out of the solution and kept at room temperature in a foil-covered glass container in order to allow evaporation of ethanol. The drying process took three to four days. At the end of drying period, it was found that a layer of pharmaceutical crystals was deposited on surface of the polyHEMA. This layer was carefully removed from the surface by using smooth sandpaper and the surface was then gently wiped with kimwipes. The sample of crystal-free surface was used for x-ray diffraction studies.

X-ray diffraction spectra were obtained by using a Nicolet I2 x-ray powder diffractometer and Cu K_α radiation with a wavelength of 0.154 nm. The scan speed used was 0.04 degrees per minute and the 2θ range used was 5° - 45°.

PolyHEMA containing nano-confined benzoic acid was firstly studied. As mentioned earlier here the sample was in 10 mm × 7 mm × 5 mm dimensions. It was directly mounted onto a glass slide of 30 mm × 5 mm × 1 mm dimensions and adhered to the glass by a thin layer of vacuum grease. Once the sample was firmly attached onto the glass piece, it was then mounted on the x-ray sample holder and the experiment was ready to start. Nanocrystalline salicylic acid and methyl paraben samples in polyHEMA matrix were prepared in a similar manner, and their x-ray diffraction spectra were studied.

Second, x-ray diffraction spectra of pure benzoic acid were studied by x-ray diffraction. For this purpose, the pure benzoic acid was lightly ground in an agate mortar and pestle in order to obtain a random orientation so that the number of diffraction peaks obtained would be sufficient for analysis of particle size of nanocrystals. The preparation procedure of the powder sample for the x-ray diffraction experiment was as follows: the sample was uniformly spread on a clean paper and a transparent glass slide of 30 mm × 5 mm × 1 mm dimensions, with one surface covered with a thin film of vacuum grease, was gently pressed onto the powder sample on the clean paper. Once the powder sample was adhered to the glass slide, the slide was mounted on the x-ray spectrometer's sample holder.

As will be shown in section 3.3.2, the peaks observed for the finely ground sample are broader even than those for nanoconfined sample. Therefore in a final experiment, the x-ray diffraction study was repeated for pure benzoic acid sample. The sample was directly used in the as-received state, which consisted of crystals of ~ 0.5 mm in size. The sample procedure was followed as for the sample before.

Since it was hypothesized that powder pharmaceuticals crystals deform in the grinding process and the fine powder crystals contain residual stresses that do not vanish on aging, samples for further x-ray diffraction experiments were not ground to a fine powder. Polycrystalline salicylic acid and methyl paraben samples were studied in the as-received state without grinding.

3.3 Results and Discussions

3.3.1 Differential Scanning Calorimetry Studies

3.3.1.1 Investigation of Ethanol-PolyHEMA Interaction

The purpose of this experiment was to investigate whether there is any chemical interaction between polyHEMA and ethanol, which was used as the solvent. The DSC scans of polyHEMA containing nano-confined ethanol were performed at 10 K/min and 20 K/min rates, on both heating and cooling. The DSC thermograms for 10 K/min heating and cooling rates are shown in figure 3.1(A) and for 20 K/min heating and cooling rates in figure 3.1(B). The direction of the arrows indicates the heating and cooling and the temperature range shown here is 310-400 K.

The thermograms show only a very small change of slope at ~ 370 K. Neither an endothermic nor an exothermic feature was observed during heating and cooling over the temperature range of 313 - 423 K. There is no indication of decomposition of polyHEMA and ethanol or compound formation between them during heating and cooling over 313 - 423 K temperature range for which measurements were made. This shows that polyHEMA did not chemically react with ethanol.
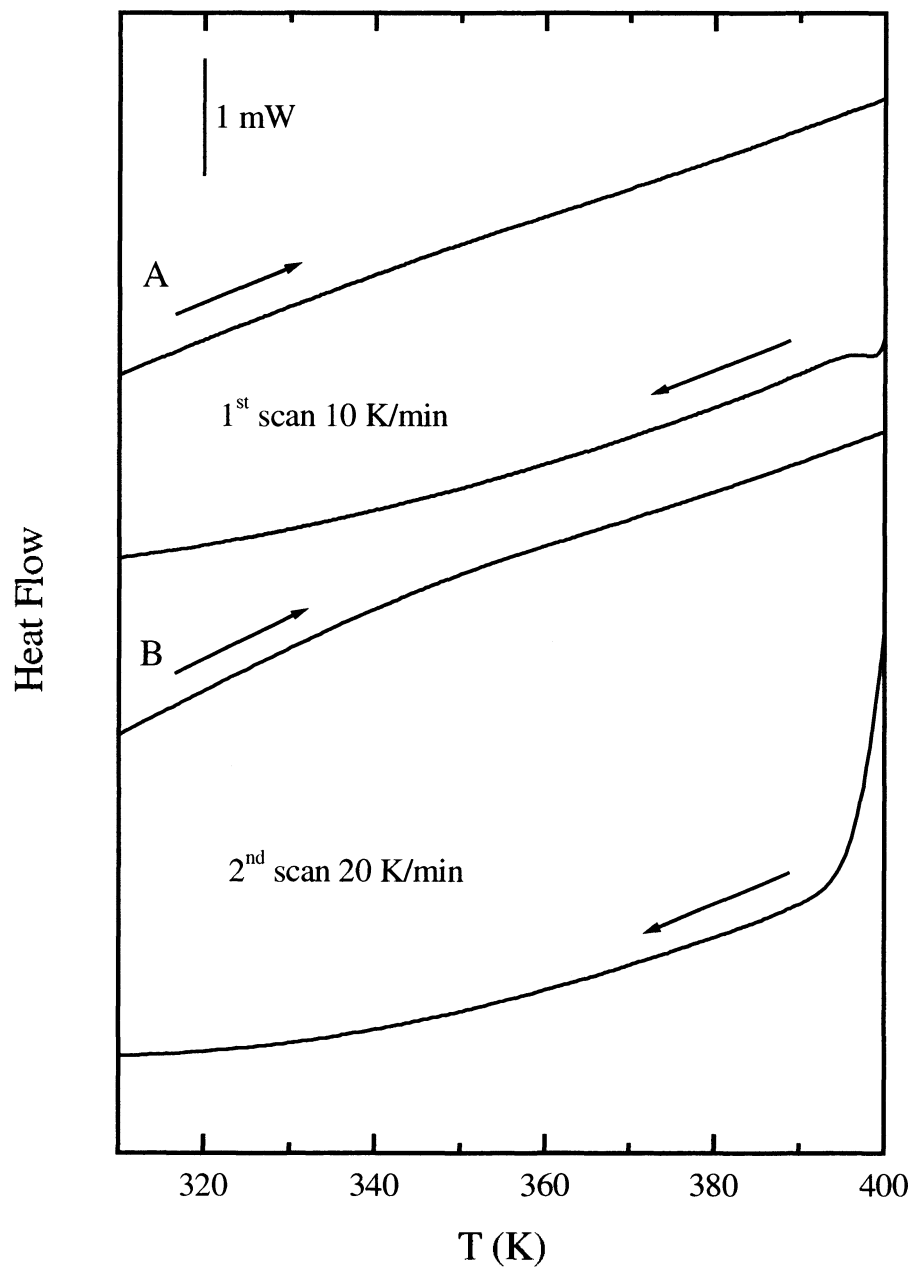
Figure 3.1 DSC thermograms of polyHEMA and ethanol thermally cycled at **(A)** 10 K/min heating and cooling rates and then subsequently at **(B)** 20 K/min heating and cooling rates

3.3.1.2 Investigations of Benzoic Acid, PolyHEMA and Ethanol

In general carboxylic acids and ethanol react to produce an ester and water as products, but it is not certain whether benzoic acid reacts with ethanol to produce an ester, ethyl benzoate. In order to investigate whether or not the ethyl benzoate is formed at room temperature, a drop of supersaturated solution of benzoic acid in ethanol was kept in an open aluminum pan isothermally for three hours at 298 K inside Q100 TA Calorimeter. The isothermal DSC thermogram obtained is shown in figure 3.2. It shows a broad exothermic minimum at ~ 8 min.

To investigate whether the exothermic minimum was caused by spontaneous precipitation of benzoic acid from solution or by formation of ethyl benzoate, we searched for studies of benzoic acid solution. Perlovic and Bauer-Brandl (2003) have reported that the enthalpy of solution of benzoic acid in ethanol at 298 K is 14.5 ± 0.3 kJ mol^{-1}. More recently, Qin, et al. (2005) have also reported that the enthalpy of vaporization of ethanol at 351 K is 38.56 kJ mol^{-1}, and it would be lower at 298 K. Therefore dissolution of benzoic acid in ethanol as well as vaporization of ethanol are endothermic. Since our solution was supersaturated, the spontaneous precipitation of benzoic acid, whose amount was much more than that of ethanol, would dominate the heat effect. But, this exothermic effect was partly compensated by the vaporization endotherm.

It was also noted that at the end of experiment, no liquid was left in the aluminum pan. Since the melting point and boiling point of ethyl benzoate are 239 K and 485 K, respectively, neither the ester nor water was formed. Only thin, white plates of benzoic acid crystals were found in the pan. Also ethyl benzoate forms only in the presence of catalyst, such as sulfuric acid, supports this findings. We conclude that no chemical reaction between benzoic acid and ethanol occurred at room temperature.
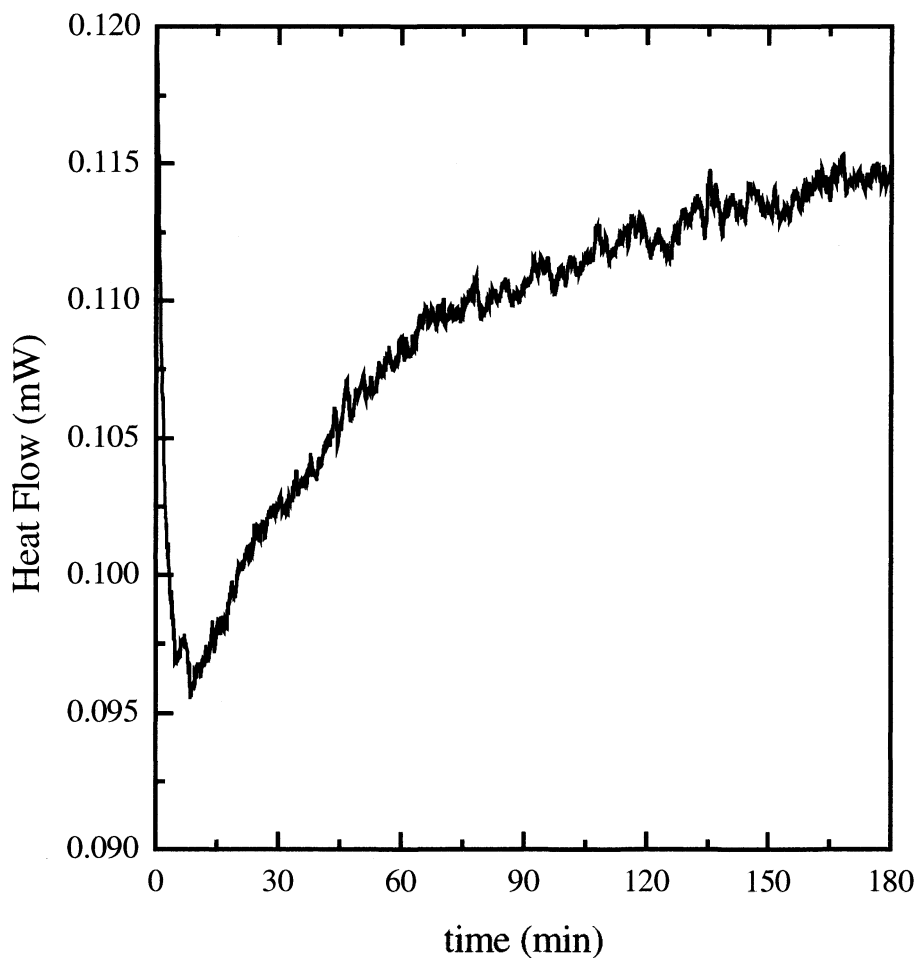
Figure 3.2 DSC thermogram of isothermal annealing at 298 K of benzoic acid
supersaturated solution

DSC studies were also performed for pure benzoic acid, its supersaturated

solution, and dry polyHEMA containing benzoic acid nanocrystals. The DSC scans of

each sample were performed on heating and cooling, both at 10 K/min rate over

temperature range of 323 - 413 K. The DSC scan was repeated only for dry polyHEMA

containing benzoic acid nanocrystals. The DSC thermograms obtained at 10 K/min heating rate are shown in figure 3.3(A) for pure benzoic acid crystals, in figure 3.3 (B) for benzoic acid dissolved in ethanol, and in figure 3.3(C) for benzoic acid nanocrystals embedded in polyHEMA.

Figure 3.3(A) shows one endothermic peak corresponding to melting of benzoic acid. The observed onset melting temperature, T_m, of benzoic acid is 395 K, which agrees with its literature value of 395 K.

Figure 3.3(B) shows two endothermic peaks. One peak has an onset temperature of 395 K corresponding to the melting of bulk benzoic acid and the other one shows an onset temperature of ~ 400 K. As ethyl benzoate (ester) has melting point of 238 K and boiling point of 486 K, this second endothermic peak corresponds to neither melting nor boiling of the ethyl benzoate. This again confirms that there was no ester formation.

In figure 3.3(C), two endothermic peaks on heating of dry polyHEMA containing benzoic acid nanocrystals, similar to those observed in figure 3.3(B), are again observed. However, as described in the beginning of this section, ethanol evaporates from the solution at room temperature leaving the pharmaceutical crystals in the DSC pan. Thus it is possible that some ethanol solution itself evaporated and deposited underneath the DSC pan holder's platinum cover. This solution evaporated leaving benzoic acid underneath the DSC pan holder's cover. The thermal lag between the sample and the pan holder's cover showed as melting of benzoic acid at a 5 K higher temperature.

Figure 3.3 (C) also shows that T_m of the benzoic acid nanocrystals in the polyHEMA matrix is 364 K, ~ 20 K below that of pure benzoic acid bulk crystals. The second heating scan shows a slight exothermic dip prior to the endotherm of benzoic acid nanocrystals shifts upward to 376 K. This indicates that on second heating cycle, benzoic acid nanocrystals inside nanopores coalesce and the released energy appears as an exotherm.
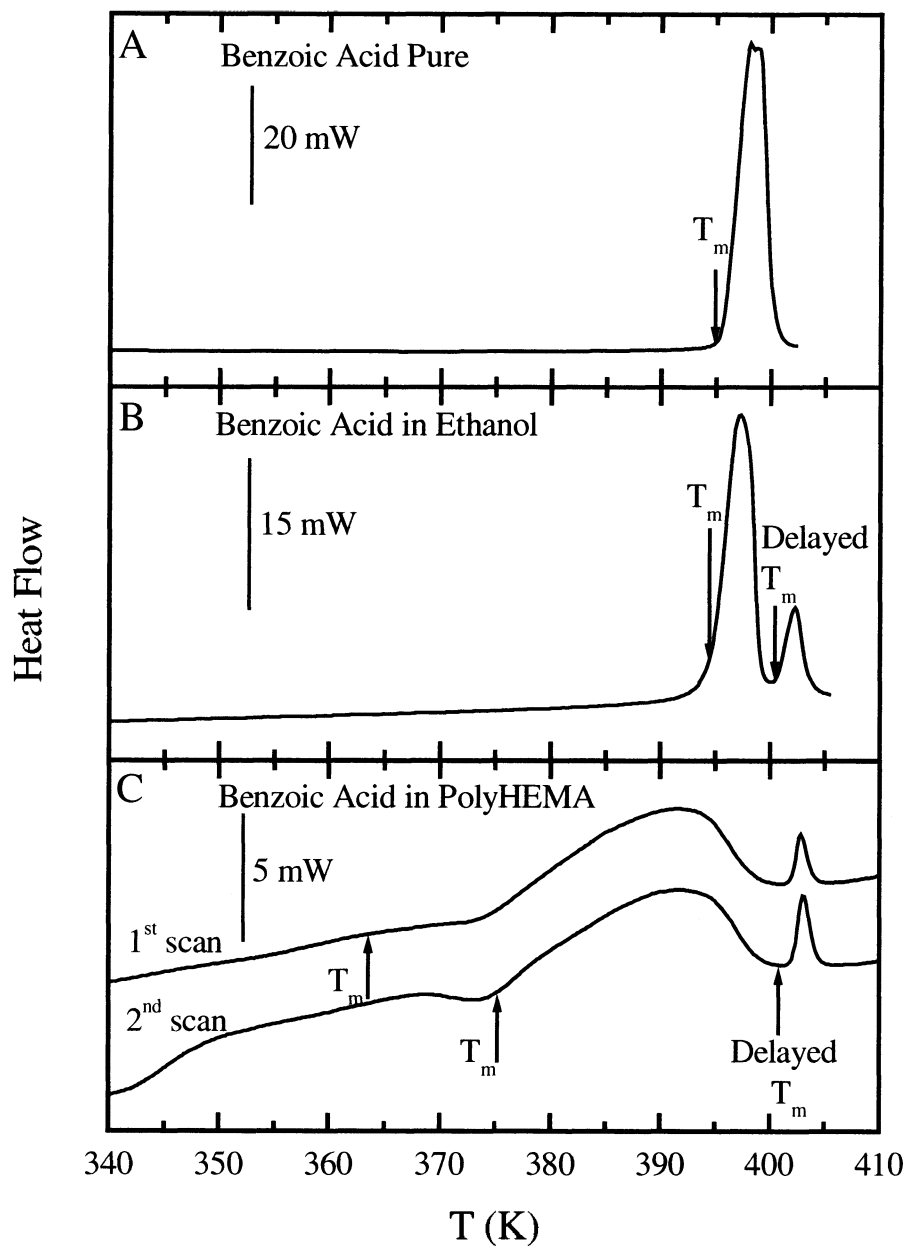
Figure 3.3 DSC thermograms on heating at 10 K/min rate of benzoic acid **A.** pure crystal **B.** supersaturated solution and **C.** embedded in PolyHEMA

3.3.1.3 Investigation of Salicylic Acid, PolyHEMA and Ethanol

The DSC studies performed for pure salicylic acid crystals, its supersaturated solution, and salicylic acid nanocrystals in dry polyHEMA matrix are shown in figures 3.4(A), 3.4(B) and 3.4(C) respectively. The DSC scans of each sample was performed on heating and cooling, both at 10 K/min rate over temperature range of 333 - 443 K and the scan was repeated only for the dry polyHEMA containing salicylic acid nanocrystals.

Figure 3.4(A) shows that only one endothermic melting peak appears for bulk salicylic acid crystals. Its onset melting temperature is 431 K, which agrees with its known T_m of 431 K.

Figure 3.4(B) shows two endothermic peaks. The first endothermic peak shows T_m of 431 K corresponding to the melting of pure bulk salicylic acid. The second peak, relatively smaller than the first one, is similar to that observed for benzoic acid supersaturated solution. This second peak shows T_m of ~ 437 K corresponds to delayed melting of the salicylic acid underneath the DSC platinum pan holder's cover, as for the benzoic acid studies.

Figure 3.4(C) shows that T_m of salicylic acid nanocrystals in polyHEMA is 398 K, 33 K lower than that of bulk salicylic acid crystals. The second heating scan shows the increase in T_m by as much as 6 K to 404 K due to the agglomeration or coalescence of salicylic acid nanocrystals inside polyHEMA that occurred on heating. As for benzoic acid, it also shows an exothermic dip prior to the broad melting endotherm, thereby indicating coalescence of nanocrystals.
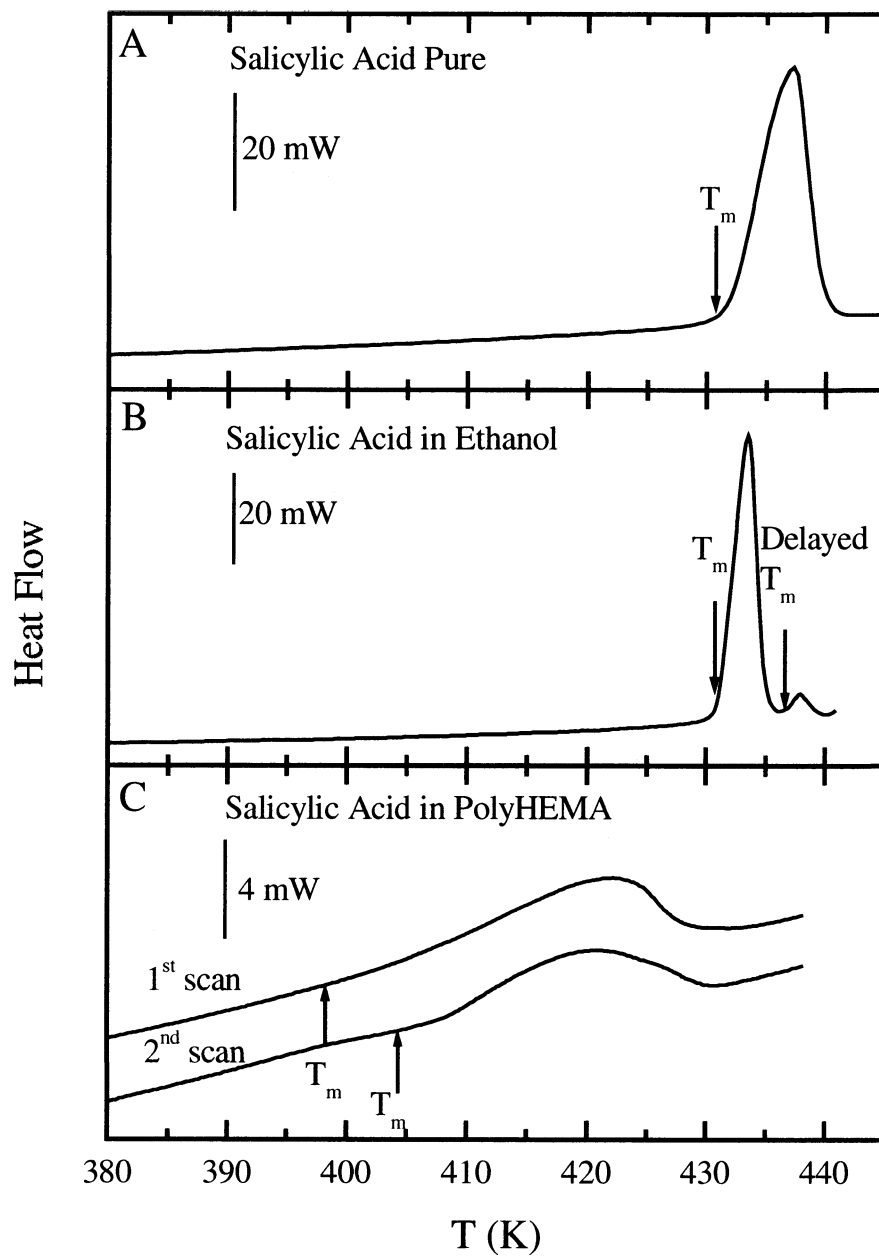
Figure 3.4 DSC thermograms on heating at 10 K/min rate of salicylic acid **A.** pure crystal **B.** supersaturated solution and **C.** embedded in PolyHEMA

3.3.1.4 Investigations of Methyl Paraben, PolyHEMA and Ethanol

The DSC studies performed for pure methyl paraben crystals, its supersaturated solution, and methyl paraben nanocrystals in polyHEMA matrix are shown as thermograms in figures 3.5(A), 3.5(B) and 3.5(C) respectively. The thermal cycles were performed two times for each sample at 10 K/min rate on both heating and cooling over temperature range of 343 - 408 K.

Figure 3.5(A) shows that T_m of pure methyl paraben observed is 398 K for the first heating scan and 388 K for the second heating scan. The 10 K difference of T_m between the first-scan melting peak and the second-scan endothermic peak indicates that new crystal phase of methyl paraben had formed on freezing of its melt. A search in the literature has never mentioned about formation of any polymorphs nor any degradation of methyl paraben during thermal cycling. Thus, this could be one of interesting topics for further study of polymorphs and compound formation of pharmaceuticals by using a calorimetry.

Figure 3.5(B) shows that T_m for the first heating scan of methyl paraben supersaturated solution is 398 K, which agrees with that of the bulk methyl paraben. But, T_m of the same sample for the second heating scan is 6 K below that of the second heating scan of bulk, 382 K.

Figure 3.5(C) shows two endothermic peaks for the first scan. The first peak shows that T_m of methyl paraben nanocrystals in polyHEMA is 381 K, 1 K less than that of methyl paraben solution. The second peak shows T_m at 388 K corresponds to melting of deposited methyl paraben underneath the DSC platinum pan-holder's cover. Even though the extent of decrease in T_m is very small, ~ 1 K, it still indicates that methyl paraben nanocrystals form in the nanopores of polyHEMA. The second scan shows only one endothermic peak corresponding to melting of methyl paraben nanocrystals. The second peak found in the first scan vanishes.
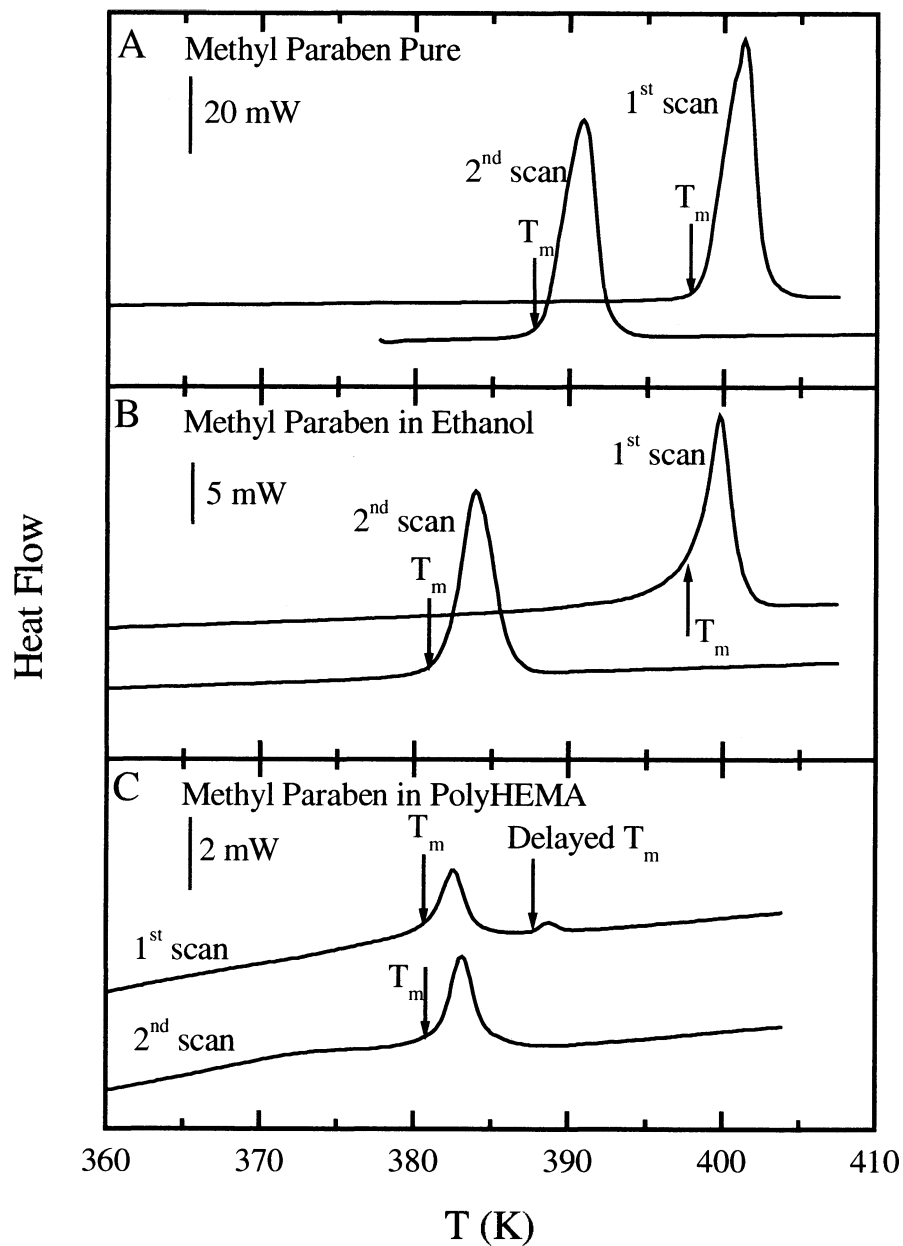
Figure 3.5 DSC thermograms on heating at 10 K/min rate of methyl paraben **A.** pure crystal **B.** supersaturated solution and **C.** embedded in PolyHEMA

3.3.1.5 Sample Calculation for Determining the Critical Radii for α-β Tin
Transformation

Although no phase inversion was found for methyl paraben, in our study, it seemed appropriate to determine the conditions in which phase inversion may occur. This was done for material whose surface tension and other properties are known, namely white tin (I4$_2$/amd) and grey tin (Fd3m). As described in Section 1.5 as the particle size of a polymorphic material is decreased below its critical radius, an inversion of its phase stability would occur.

The β-tin, also known as white-tin, is stable at above 298 K. Its polymorphic phase, α-tin, also known as grey-tin, is formed at temperature below 13.2 °C or 282.2 K. The characteristics of these two phases of tin are provided in Table 3.1.

Table 3.1 The characteristics of grey and white tin

Characteristic	Grey (α) tin	White (β) tin
Cell structure	Diamond cubic	Body centered tetragonal
Density (g/cm^3)	5.79	7.28
Work function, φ (eV)	4.42	4.42
Structure coefficient (q)	1	1.62
Coordination electron (z)	1	1
Molecular weight (g/mole)	118.7	118.7
Heat of transformation (J/mole)	5298	5298

From the information given above, the surface energies, γ, of both phases of tin can be calculated based on theoretical approach by Missol (1972) following a relation,

$$\gamma = \frac{1530}{q}\varphi\left(\frac{1}{V}z\right)^{2/3} \quad \text{mJ/m}^2 \tag{3.1}$$

110

The calculation gives γ value of 903 mJ/m^2 for α-tin and 650 mJ/m^2 for β-tin. Since γ_α is higher than γ_β, the concept of phase stability inversion is applicable for tin.

There are three equations for phase inversion in Section 1.5, one by Chraska et al. (2000) is equation (1.14) and the other two by Johari (2005) are equation (1.15) and (1.16). Since equation (1.14) directly provides the temperature difference from the equilibrium transformation temperature, we use this equation and the data for tin from the literature, as listed in Table 3.1, for determining the critical radius. The critical radius, r_c, defined as the radius of a particle at which the transformation occurs at a given temperature and pressure, for α-β tin solid-solid transformation is determined by using equation (1.14) in Section 1.5 given by Chraska et al. as follows,

$$r_c = \frac{-3(\gamma_\beta - \gamma_\alpha)}{\Delta H_t^{\beta \to \alpha}\left(1 - \frac{T}{T_t}\right)} \tag{1.14}$$

where $\Delta H_t^{\beta \to \alpha}$ is the heat involved during α-β tin transformation process, T_t the transition temperature of bulk tin, whose value is 286.2 K, and γ_α and γ_β the surface energies of α- and β-tin respectively.

The calculation for various temperatures gives critical radii as listed in Table 3.2. The temperature-dependent critical radii of α-β tin transformation are shown in figure 3.6. As the temperature increases, the critical radius for transformation also increases, reaching a bulk radius as $T \to T_t$.

This information is provided here as an example for calculation of critical radii for phase inversion of nanoparticles of materials, including pharmaceuticals, and can be used for stabilizing phases at ambient temperature which are not formed under these conditions.

Table 3.2 The critical radius, r_c, obtained from calculation for various temperatures, T

T (K)	r_c (nm)	T (K)	r_c (nm)
20	2.51	160	5.30
40	2.71	180	6.29
60	2.95	200	7.75
80	3.24	220	10.10
100	3.59	240	14.47
120	4.02	260	25.51
140	4.57	280	107.79
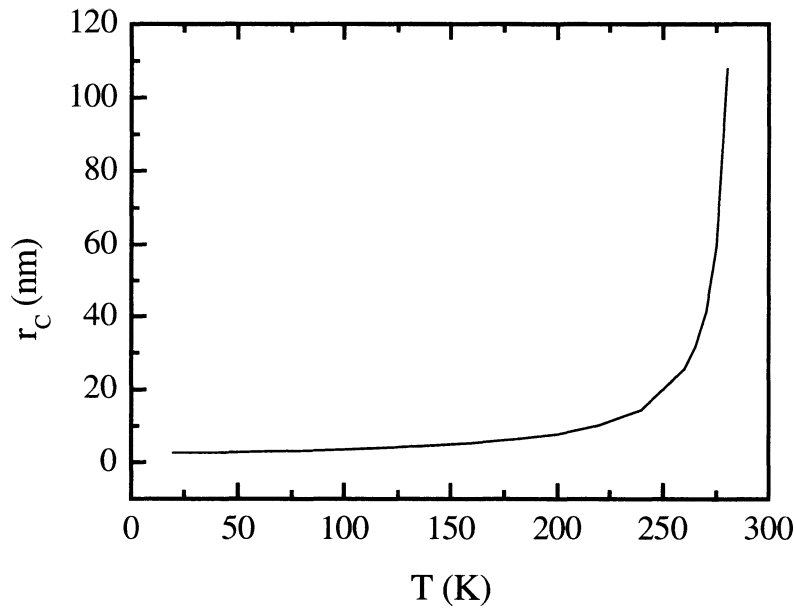
Figure 3.6 The critical radii, r_c, for α-β tin solid-solid transformation as a function of temperature

112

3.3.2 X-Ray Diffraction Results

The x-ray diffraction spectra of finely ground sample, nano-confined sample in polyHEMA matrix and as-received sample of benzoic acid are shown in figure 3.7. For convenience of description, we have chosen one peak at 2θ of 16.25° for each sample.

The standards for each pharmaceutical crystal were obtained from the Joint Committee on Powder Diffraction Standards (JCPDS 1983). The XRD results of pure pharmaceuticals are in accordance with the standards given. This confirmed the structures of the crystal and their purity. The XRD results of pure crystals and that of nanocrystals confined in the matrix are shown for benzoic acid in figure 3.8(A) and (B), for salicylic acid in figure 3.9(A) and (B), and for methyl paraben in figure 3.10(A) and (B).

From the diffraction peaks obtained, the size of the crystals in nanoporous polyHEMA can be calculated. The full width at half maximum for each peak is measured for crystals in the matrix and pure crystals. The total broadening of the peak due the size effect is calculated by using Warren's formula [Cullity (2001)],

$$B = \sqrt{B_m^2 - B_s^2} \tag{3.2}$$

and the crystal size in polyHEMA matrix by Scherrer's formula [Cullity (2001)],

$$t = \frac{0.9\lambda}{B\cos\theta} \tag{3.3}$$

where,

B_s = Full width at half maximum of pure crystals

B_m = Full width at half maximum of the sample of pharmaceutical crystals in the nanopores of polyHEMA matrix

B = Total broadening

λ = The wavelength used for X-ray diffraction experiments

t = The crystal size
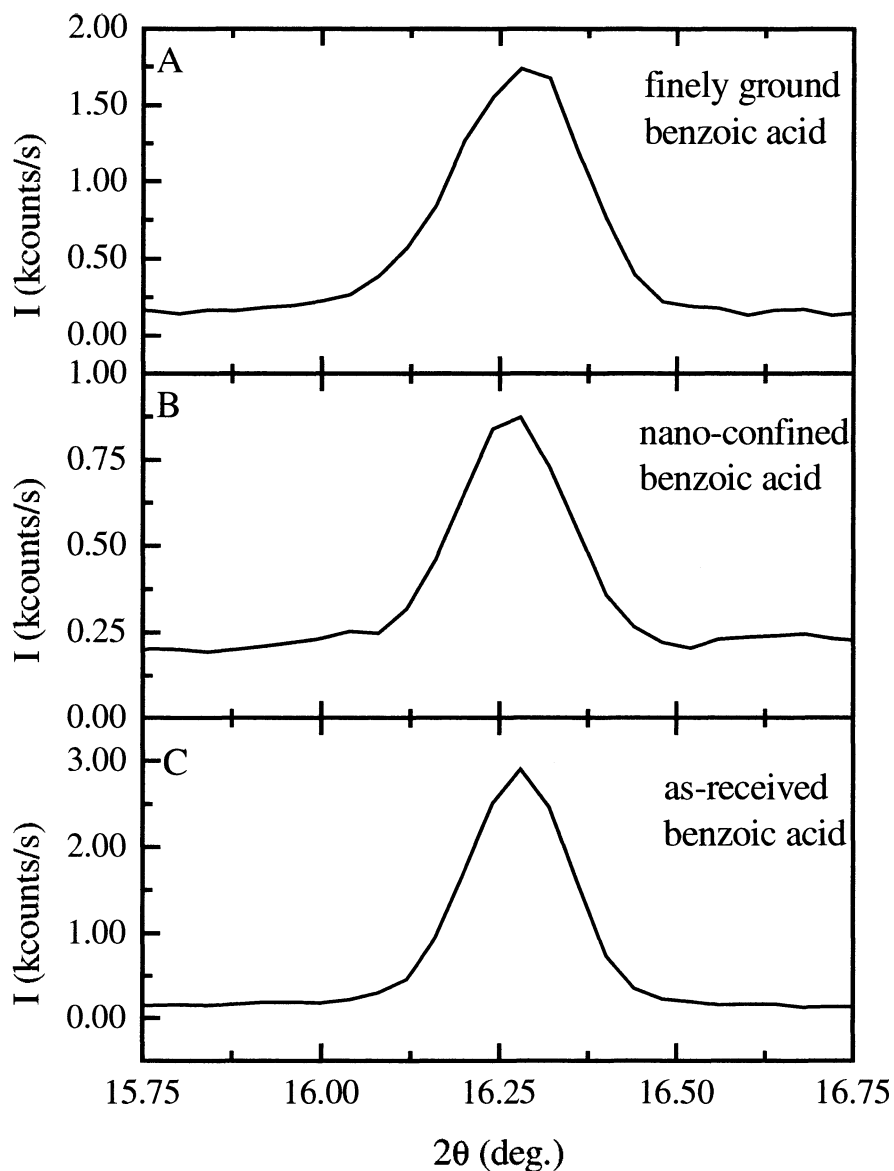
Figure 3.7 XRD peak of **A.** finely ground benzoic acid **B.** nano-confined benzoic acid in polyHEMA matrix and **C.** as-received benzoic acid at 2θ of $16.25°$. The peaks have been shifted to match the position so that the instrumental adjustment errors are eliminated.
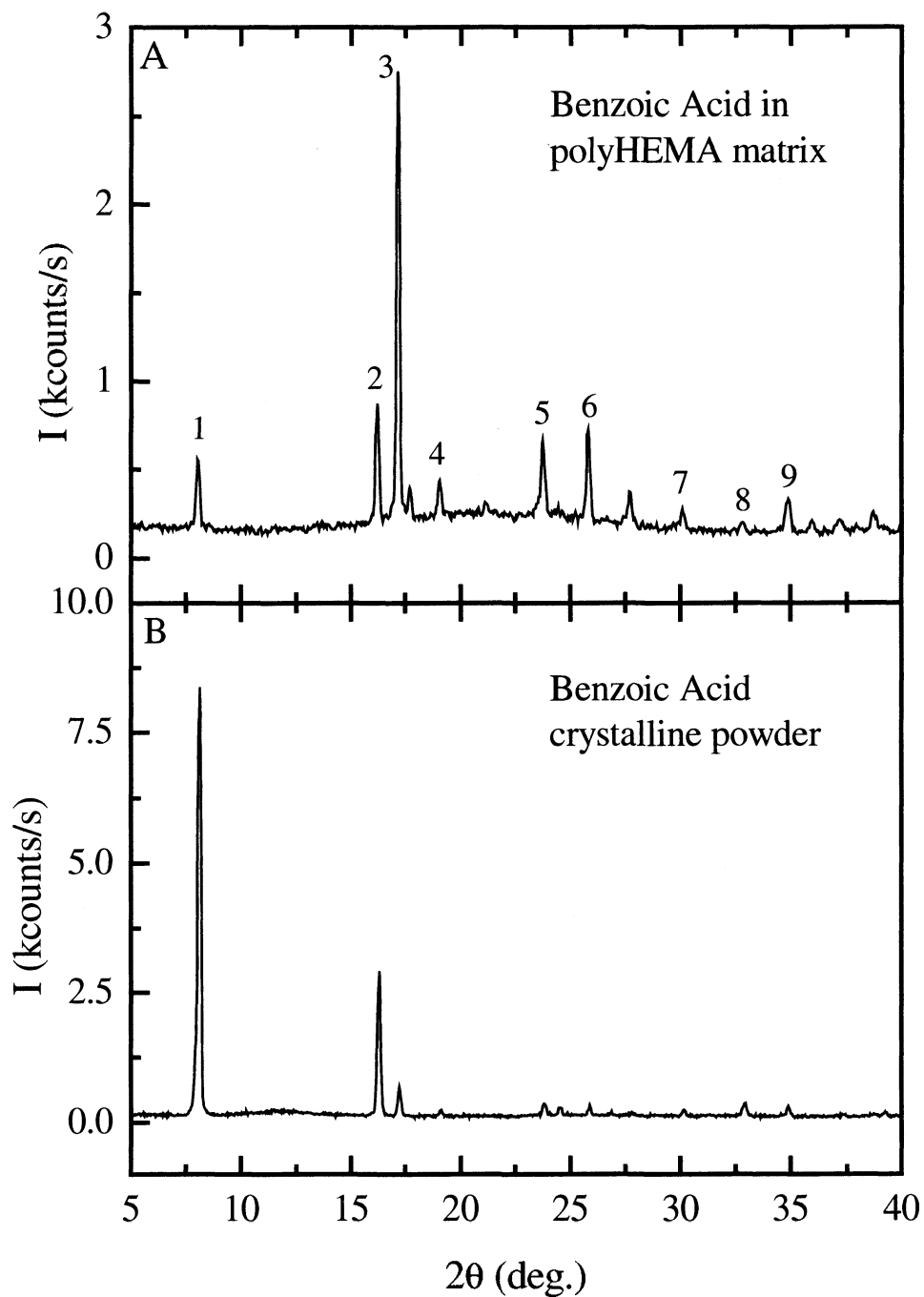
Figure 3.8 A. XRD spectra of confined benzoic acid nanocrystals in polyHEMA matrix.
B. XRD spectra of pure benzoic acid bulk crystalline powders
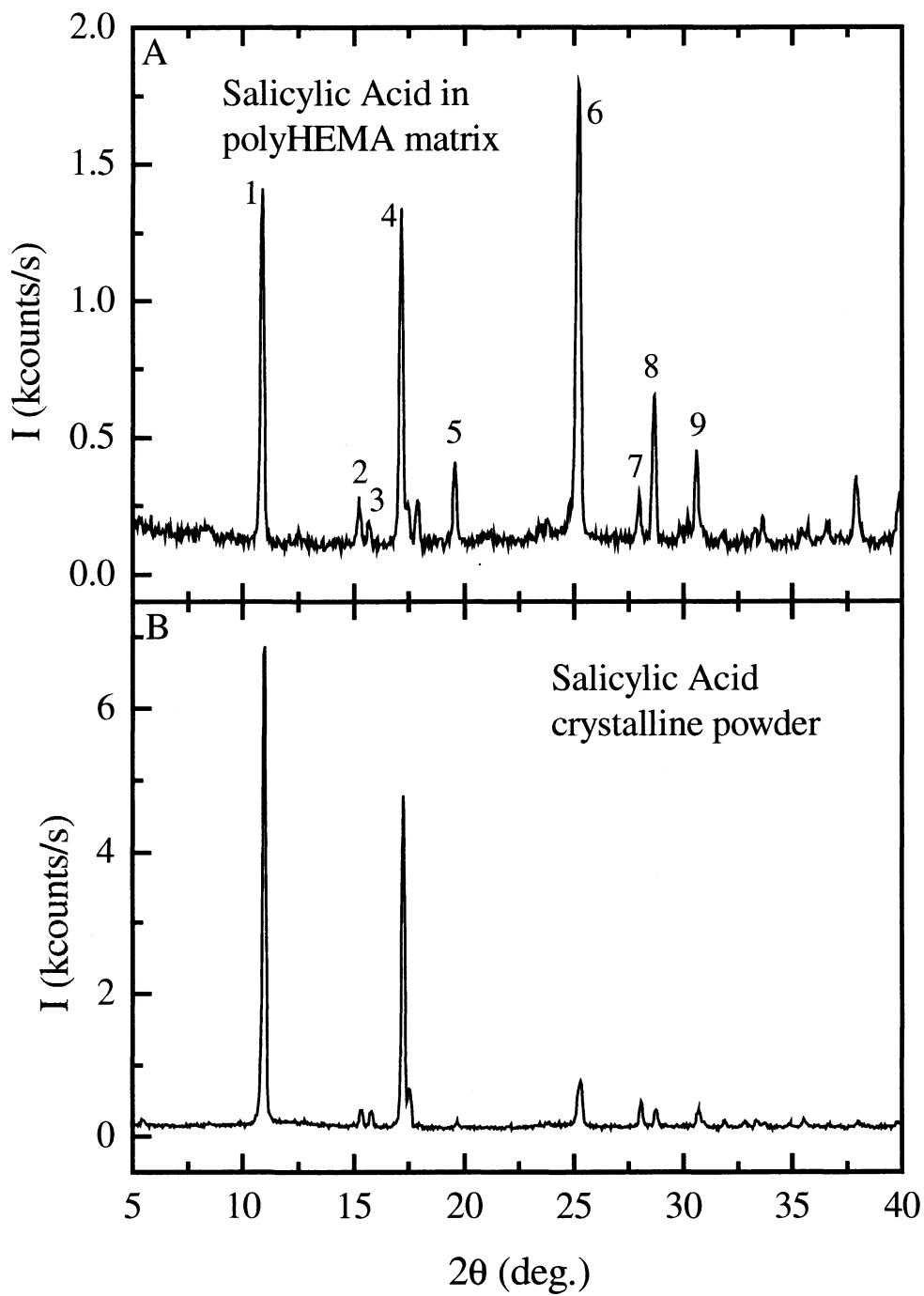
Figure 3.9 **A.** XRD spectra of confined salicylic acid nanocrystals in polyHEMA matrix.
B. XRD spectra of pure salicylic acid bulk crystalline powders
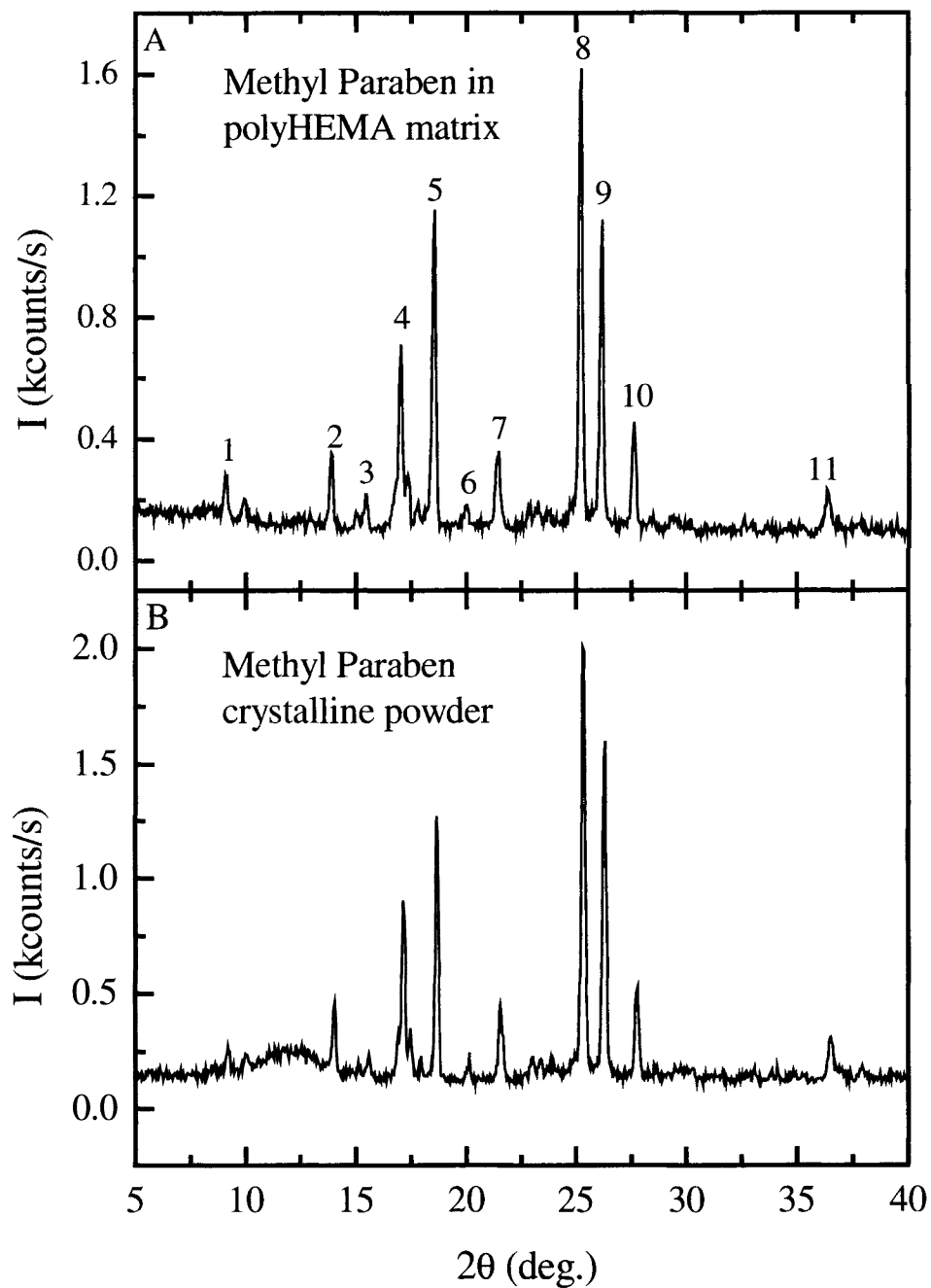
Figure 3.10 A. XRD spectra of confined methyl paraben nanocrystals in polyHEMA
matrix. **B.** XRD spectra of pure methyl paraben bulk crystalline powders

The standard broadening, B_s, defined as the full width at half maximum (FWHM) of standard pure pharmaceutical crystals, represents the measurable width of the diffraction lines due to instrumental artifacts, i.e. due to the divergence of the incident beam and the width of X-ray source, and crystal size effect of the bulk samples. The total broadening, B, refers to the extra width due to the particle size effect alone. Cullity (1976, p. 284-285) has stated:

"The experimental difficulties involved in measuring particle size from line broadening increase with the size of the particle measured. Roughly speaking, relatively crude measurements suffice in the range 0-500 Å, but very good experimental technique is needed in the range 500-1000 Å. The maximum size measurable by line broadening was formerly placed at 1000 Å, chiefly as a result of the use of camera techniques. With the diffractometer, however, the upper limit has been pushed to almost 2000 Å."

However, the x-ray spectra of the first two x-ray diffraction of benzoic acid showed that the full width at half maximum (FWHM) of powdered benzoic acid were broader than the corresponding FWHM of benzoic acid nanocrystals in polyHEMA. This is shown in figure 3.7(A) and (B), whereby for convenience in comparison, only the diffraction peaks with 2θ of 16.25° are shown. Thus, the particle size analysis cannot be determined due to this error.

The broader FWHM of the pure benzoic acid than that of the nanocrystals benzoic acid was not caused by the small particle size effect, rather by the presence of residual strains induced by the internal stress. It was hypothesized that the grinding process during sample preparation did not only introduce the desired random orientation within the sample, resulting in more diffraction peaks, but also internal stresses. The internal stresses introduced residual strains in pure benzoic acid sample and made the FWHM of its diffraction peaks broader than the corresponding FWHM of that of nanocrystals benzoic acid. The spectra of the final experiment showed that the diffraction peaks obtained was fewer, sharper and higher in intensity than those obtained from the ground sample. The fewer high intensity diffraction peaks obtained from the pure as-received

118

sample were due to the preferred orientation, instead of random orientation, of the crystal within the sample.

The peaks, for which broadening was calculated, are labeled 1-9 for both benzoic acid and salicylic acid, and 1-11 for methyl paraben. The peaks showed narrowing were neglected. Because of the less random orientations and possibly nano-confined effect, peaks observed for bulk benzoic acid differ in intensity than those observed for the nano-confined states. Because of these, all peaks in the nanoconfined-sample are not clearly seen in the bulk sample, but all are likely to be present.

From the XRD results of the three pure crystals, benzoic acid gives the narrowest width at half maximum throughout all the obtained diffraction peaks. The larger FWHM of salicylic acid and methyl paraben compared to that of benzoic acid were partly due to their different molecular weight and partly due to orientational disorder, which may arise from their complicated molecular shapes, potentially causing larger thermal vibrations. Therefore, only the broadening of diffraction lines for pure benzoic acid crystals represented the instrumental artifacts. Hence, FWHM of benzoic acid was used as a standard broadening for further particle size calculation of other pharmaceuticals by using Scherrer's formula.

For benzoic acid nanocrystals in polyHEMA matrix nine peaks were observed in Figure 3.8 A and only one of these does not show a broadening. For salicylic acid nanocrystals in polyHEMA matrix in figure 3.9 A, the ratio of broadening to non-broadening peak was 8:1, while for methyl paraben nanocrystals in polyHEMA in figure 3.10 A, the ratio of broadening to non-broadening peak was 10:1.

As the 2θ peaks obtained for benzoic acid sample are different from those for salicylic acid and pure methyl paraben, the closest value of 2θ of benzoic acid was chosen for calculation of standard broadening for nanocrystals of all the three in polyHEMA matrix. Additionally, the cos θ value used for crystal size calculation was the average of cos θ value of the benzoic acid peak and that of the corresponding nanocrystals in polyHEMA. The list of the calculated crystal size for benzoic acid, salicylic acid and methyl paraben are presented in Table 3.3, Table 3.4, and Table 3.5

119

respectively. The example of the calculation steps used for determining the crystal size in the polyHEMA matrix is given in Appendix C.

Table 3.3 Calculation of benzoic acid crystal size in polyHEMA

2θ (deg.)	B_s (deg.)	B_m (deg.)	B (deg.)	B (rad.)	t (nm)
8.105	0.1839	0.2012	0.0815	0.00142	97.75
16.250	0.1714	0.1788	0.0509	0.00089	157.64
19.112	0.1620	0.2098	0.1333	0.00233	60.43
23.836	0.1813	0.2074	0.1007	0.00176	80.61
25.879	0.1223	0.1885	0.1434	0.00250	56.83
30.157	0.1596	0.2248	0.1583	0.00276	51.97
32.815	0.2156	0.2721	0.1660	0.00290	49.89
34.854	0.1796	0.2969	0.2364	0.00413	35.22

Average: 73.79 nm

Table 3.4 Calculation of salicylic acid crystal size in polyHEMA

2θ (deg.)	B_s (deg.)	B_m (deg.)	B (deg.)	B (rad.)	t (nm)
10.982	0.1839	0.1901	0.04812	0.00084	165.68
15.784	0.1714	0.1968	0.09671	0.00169	82.96
17.271	0.1754	0.1887	0.06959	0.00121	115.47
19.672	0.1620	0.1767	0.07056	0.00123	114.22
25.317	0.1223	0.2561	0.22501	0.00393	36.21
28.090	0.1596	0.1751	0.07203	0.00126	113.96
28.775	0.1596	0.1985	0.11803	0.00206	69.60
30.709	0.1596	0.1709	0.06111	0.00107	134.72

Average: 99.73 nm

Table 3.5 Calculation of methyl paraben crystal size in polyHEMA

2θ (deg.)	B_s (deg.)	B_m (deg.)	B (deg.)	B (rad.)	t (nm)
13.847	0.1714	0.1958	0.0947	0.00165	84.66
15.264	0.1714	0.1888	0.0792	0.00138	101.30
17.004	0.1754	0.1947	0.0845	0.00148	95.05
18.547	0.1754	0.1912	0.0761	0.00133	105.67
19.981	0.1620	0.2125	0.1375	0.00240	58.62
21.446	0.1620	0.2520	0.1930	0.00337	41.81
25.208	0.1223	0.1775	0.1286	0.00225	63.32
26.188	0.1223	0.1894	0.1446	0.00252	56.38
27.593	0.1223	0.2116	0.1727	0.00301	47.29
36.342	0.1796	0.2604	0.1886	0.00329	44.25

Average: 69.84 nm

The average crystal sizes in the samples obtained from the calculation are 73.79 nm, 99.73 nm, and 69.84 nm for benzoic acid, salicylic acid and methyl paraben respectively. The average crystal size for all three pharmaceuticals in polyHEMA matrix is in the range of 70 to 100 nm, which represents the size distribution of nanopores in polyHEMA matrix. This study shows that solution diffusion and evaporation technique indeed produces nanocrystals and it can be useful for pharmaceutical sciences. It also shows the advantage of materials science techniques for study of pharmaceuticals.

3.4 Conclusion

A new method has been developed for producing nano-sized crystals in polymer matrix. From a calorimetric study of benzoic acid, salicylic acid and methyl paraben nanocrystals formed in the polyHEMA matrix by solution diffusion process using ethanol, it is shown that the technique is effective in producing nano-sized pharmaceuticals for controlled-release. The presence of the nanocrystals is confirmed by the decrease in T_m of the bulk pharmaceutical crystals through DSC experiments. Furthermore, the average size of each of pharmaceuticals nanocrystals has been determined by using X-ray diffraction spectra.

In brief, this study provides a new technique for producing controlled-release nano-sized pharmaceuticals by using a biocompatible polymer as a matrix. The general procedure done is as follows:

(1) Bulk pharmaceutical crystals are dissolved in a solvent, in which pharmaceuticals show a considerable amount of solubility and with which it does not chemically react, and its supersaturated state is produced.

(2) A polymer is immersed in the solution for sufficient time, depending on its dimensions, and the solution is allowed to diffuse into the nanopores of the swollen polymer.

(3) The swollen polymer is dried in open convection oven and the solvent is evaporated. This leaves nanocrystals of the pharmaceuticals in the polymer matrix.

For applications, when the body fluid diffuses into the polyHEMA, the pharmaceutical nanocrystals will rapidly dissolve in the fluid. The solution will lose its active pharmaceutical by diffusion into the body fluid at a controlled rate to the addressed body part.

This study therefore provides a new method of producing nanocrystals, which is not available for metals such as zinc studies here. It uses the same materials science techniques as the study of zinc nanocrystals described in chapter 2.

A sample calculation for transformation between α-tin and β-tin shows that below the equilibrium transformation temperature at which α-tin is stable, a decrease in the particle size would transform α-tin to β-tin. This phase inversion temperature decreases as the particle size is further decreased. The lower value of surface energy of the metastable phase than that of the stable phase causes this inversion of phase stability of polymorphic materials as a function of its radius.

REFERENCES

Bachels, T.; Güntherodt, H-J.; Schäfer, R., *Phys. Rev. Lett.* **85** (2000) 1250-1254

Banerjee, R.; Jayakrishnan, R.; Ayyub, P., *J. Phys. Condens. Matter* **12** (2000) 10647-10654

Baraton, M-I.; Merhari, L.; Ferkel, H.; Castagnet, F., *Mater. Sci and Eng. C* **19** (2002) 315-321

Bergese, P.; Colombo, I.; Gervasoni, D.; Depero, L. E., *J. Phys. Chem. B* **108** (2004) 15488-15493

Berry, C. R., *Phys. Rev.* **88** (1952) 596-599

Borg, R. J., and Dienes, G. J., *The Physical Chemistry of Solids*, Academic Press, New York, 1992, p. 69-83

Boyer, L. L., *Phase Transitions* **5** (1985) 1-47

Buffat, Ph. and Borel, J-P., *Phys. Rev. A* **13**, (1976) 2287-2298

Chalmers, B., *The Structure and Properties of Solids*, 1982, Heyden & Son Ltd., London

Chase, M. W., Jr., NIST-JANAF Thermochemical Tables, 4th ed., Part II, Cr-Zr, J. Phys. Chem. Ref., Data Monograph No. 9, 1998

Chen, J. P.; Sorensen, C. M.; Klabunde, K. J., *Phys Rev B* **51** (1995) 11527-11532

Chen, J-F.; Zhou, M-Y.; Shao, L.; Wang, Y-Y.; Yun, J.; Chew, N. Y. K.; Chan, H-K., *International Journal of Pharmaceutics* **269** (2004) 267-274

Chen, Q., and Sundman, B., *Acta Mater.* **49** (2001) 947-961

Cheng, H. P., and Berry, R. S., *Phys. Rev. A* **45** (1992) 7969-7980

Cho, S.; Ma, J.; Kim, Y.; Sun Y.; Wong, G. K. L.; Ketterson, J. B., *Appl. Phys. Lett.* **75** (1999) 2761-2763

Choudhary, M. S., and Varma, I. K., *Macromol. Sci. Chem. A* **20** (1983) 771-779

Chraska, T.; King, A. H.; Berndt, C. C., *Mater. Sci Eng. A* **286** (2000) 169-178

Coombes, C. J., *J. Phys. F : Metal Phys.* **2** (1972) 441-449

Cotterill, R. M., *J. Cryst Growth.* **48** (1980) 582-588

Couchmann, P. R. and Jesser, W. A., *Nature* **269** (1977) 481-483

Cullity, B. D., *Elements of X-Ray Diffraction*, 3rd ed., Addison-Wesley Inc., 1967

Cushing, B. L.; Kolesnichenko, V. L.; O'Connor, C. J., *Chem. Rev.* **104** (2004) 3893-3946

Dachun, Z.; Zhongkai, Q.; Xiaoren, P.; Muji, D.; Minggen, S., *J. Vac. Sci. Tehnol. B* **15** (1997) 805

De Planta, T.; Ghez, R.; Piuz, F., *Helv. Phys. Acta* **37** (1964) 74-76

Dick, K. et. al., *J. Am. Chem. Soc.* **124** (2002) 2312-2317

Dippel, M.; Maier, A.; Wider, H.; Evenson, W. E.; Rasera, R. L.; Schatz, G., *Phys Rev Lett.* **87** (2001) 095505(1-4)

Dobson, P. J., Paper for *"Commercial and Industrial Applications for Microengineering and Nanotechnology"*, 26th April 1999, London.

Fattal, E., and Vauthier, C., *Nanoparticles as Drug Delivery Systems*, Encyclopedia of Pharmaceutical Technology, 2002, 1864-1882

Ferroni, M.; Boscarino, D.; Comini, E.; Gnani, D.; Guidi, V.; Martinelli, G.; Nelli, P.; Rigato, V.; Sberveglieri, G., *Sensors and Actuators B* **58** (1999) 289-94

Gillet, S. L., *Nanotechnology* **7** (1996) 168-177

Ginnings, D. C., and Furukawa, G. T., National Bureau of Standards in *J. Am. Chem. Soc.* **75** (1953) 522-527

Gleiter, H., *Acta Mater.* **48** (2000) 1-29

Goldstein, A. N.; Echer, C. M.; Alivisatos, A. P., *Science* **256** (1992) 1425.

Górecki, T., *Z. Metallkd.* **65** (1974) 426-431

Górecki, T., *Z. Metallkd.* **67** (1976) 269

Grønvold, F. and Stølen, S., *Thermochim. Acta* **327** (1999) 1-32

Grønvold, F. and Stølen, S., *Thermochim. Acta* **395** (2003) 127-131

Gupta, R. K.; Sridhar, N.; Katiyar, M., *Mater. Sci. in Semicond. Process.* **5** (2002) 11-15

Hayashi, C. and Oda, M., *J. Aerosol Science* **29** (1998) 757-760

Hill, D. J. T.; Moss, N. G.; Pomery, P. J.; Whittaker, A. K., *Polymer* **41** (2000) 1287-1296

Hofer, F.; Grogger, W.; Warbichler, P; Papst, I., *Mikrochim. Acta* **132** (2000) 273-288

Hofmeister, H.; Dubiel, M.; Schurig, E., *Phys. Status Solidi B* **203** (1997) R5-6

Hofmeister, H.; Thiel, S.; Dubiel, M.; Schurig, E., *Appl. Phys. Lett.* **70** (1997) 1694-1696

Hooker, S. A., *The Nanoparticles 2002 Conference Proceedings*, 2002

Hornbogen, E., "Precipitation Hardening – The Oldest Nanotechnology," Lightweight Alloys for Aerospace Application, ed. K. Jata et al., (Warrendale, PA: TMS, 2001) p. 2-11

Hu, Y.; Tsai, H.-L.;Huang, C.-L., *Mater. Sci. and Eng. A* **344** (2003) 209-214

Hunt, W. H., *JOM* **56** (2004) 13-18

Janczuk, B.; Chibowski, E.; Wojcik, W.; Guindo, M. C.; Gonzalez-Caballero, F., *Mater. Chem. Phys.* **37** (1994) 64-67

Jeyanthi, R., and Pandhurang Rao, K., *Biomaterials* **11** (1990) 238-243

Jiang, Q.; Zhang, S.; Zhao, M., *Mater. Chem. and Phys.* **82** (2003) 225-227

Johari, G. P., *Advanced Thermodynamic Lecture Notes*, 2003

Johari, G. P., *Phil. Mag. A* **77** (1998) 1367-1380

Johari, G. P., *J. Chem. Phys.* **122** (2005) 194504(1-4)

Kersen, Ü., *Appl. Phys. A* **75** (2002) 559-563

Kersen, Ü., *The Gas Sensing Potential of Nanocrystalline SnO2 produced by different chemical reactions and milling conditions*, Helsinki University of Technology, Laboratory of Electromechanics, Report 70, Espoo 2003.

Kirchheim, R.; Huang, H. Y.; Cui, P.; Birringer, R.; Gleiter, H., *Nanostructured Mater.* **1** (1992) 167-172

Kittel, C., *Introduction to Solid State Physics*, 7th ed., John Wiley and Sons, Inc., New York, 1996.

Knauth, P. and Schoonman, J., *Nanocrystalline Metal and Oxides : Selected Properties and Applications*, 2002, Kluwer Academic Publisher

Kofman, R.; Cheyssac, P.; Lereah, Y.; A., Stella, A.; *Eur. Phys. J. D* **9** (1999) 441-444

Kofman, R.; Lereah Y.; Pennison, J.; Deutscher, G.; Cheyssac, P.; David B. T.; Bourret, A., *Phil. Mag. B* **81** (2001) 1801-1819

Kofman. R.; Cheyssac, P.; Aouaj, A.; Lereah, Y.; Deutscher, G.; David, T. B.; Penisson J. M.; Bourret, A., *Surf. Sci.* **303** (1994) 231-246

Koper, O. and Klabunde, K. J., *Chemisty of Materials* **9** (1997) 2481-2485

Kristensen, J. K., and Cotterill, *J. Phil. Mag. A* **36** (1977) 437-452

Kuhlmann-Wilsdorf, D., *Physical Review A* **140** (1965) A1599-A1610

Kumar, P. S.; Saraswathi, Y. L.; Sunandana, C. S., *Mater. Phys. Mech.* **4** (2001) 71-75

Lai, S. L.; Carlsson, J. R. A.; Allen, L. H., *Appl. Phys. Lett.* **72** (1998) 1098-1100

Lai, S. L.; Guo, J. Y.; Petrova, V.; Ramanath, G.; Allen, L. H., *Phys. Rev. Lett.* **77** (1996) 99-102

Landau, L., *J. Phys. USSR.*, **8** (1944) 201

Li, F.; Xu, J.; Yu., X.; Chen, L.; Zhu, J.; Yang, Z.; Xin, X., *Sensors and Actuators B* **81** (2002) 165-169

Lin, C. C.; Liu, K. H.; Chen, S. Y., *J. Cryst. Growth* **269** (2004) 425-431

Lin, H. M.; Tzeng, S. J.; Hsiau, P. J.; Tsai, W. L., *Nanostructured Materials* **10** (1998) 465-477

Lindemann, F. A., *Z. Phys.* **11** (1910) 609-612

Liu, X. D.; Nagumo, M.; Umemoto, M., *Mater. Trans. JIM* **38** (1997) 1033-1039

Liz-Marzan, L. M., and Kamat, P. V., *Nanoscale Materials*, 2003, Kluwer Academic Publisher

Loss, R. D., IUPAC commission on atomic weights and isotopic abundancies, *Chem. Int.* **23** (2001) 179

Lu, K, *Materials Science and Engineering*, **R16** (1996) 161-221

Lu, K.; Lück, R.; Predel, B., *Z. Metallkd* **84** (1993) 740-743

Lu, K.; Wang, J. T.; Wei, W. D., *J. Phys. D: Appl. Phys.* **25** (1992) 808-812

Martin, A.; Swarbrick, J., Cammarata, A., *Physical Pharmacy 3*, Philadephia, PA: Lea and Febiger, 1983, p. 579

Matthewson, C. H., *ZINC The Science and Technology of The Metal, Its Alloys and Compounds*, 1959, Am. Chem. Soc., Chapman & Hall London

McHale, J. M.; Auroux, A.; Perrotta, A. J.; Navrotsky, A., *Science* **277** (1997) 788-791

Meng, Q.; Zhou, N.; Rong, Y.; Chen, S.; Hsu, T. Y., *Acta Mater.* **50** (2002) 4563-4570

Metal Use Research Group, *The Properties of Zinc*, 1956, Consolidated Mining & Smelting Company of Canada

Montano, P. A.; Schulze, W.; Tesche, B.; Shenoy, G. K.; Morrison, T. I., *Phys. Rev. B* **30** (1984) 672-677

Morgan, S. W. K., *Zinc and Its Alloy*, 1977, Industrial Metal Series, Macdonald and Evans

Mumper, R. J.; Cui, Z., Oyewumi, M. O., *J. of Dispersion Science and Technology* **24** (2003) 569-588

Nanda, K. K.; Kruis, F. E.; Fissan, H., *Phys. Rev. Lett.* **89** (2002) 256103-(1-4)

Nanda, K. K.; Maisels, A.; Kruis, F. E.; Fissan, H.; Stappert, S., *Phys. Rev. Lett.* **91** (2003) 106102-(1-4)

Nanda, K. K.; Sahu, S. N.; Behera, S. N., *Phys. Rev. A* **66** (2002) 13208(1-8)

Narayan, J.; Venkatesan, R. K.; Kvit, A., *J. Nanoparticles Res.* **4** (2002) 265-269

Nieh, T. G., and Wadsworth, J., *Scripta Metall. et Mater.* **25** (1991) 955-958

Oleszak, D.; Portnoy, V. K.; Matyja, H., *Nanostruc. Mater.* **12** (1999) 621-624

Peppas, N. A. and Moynihan, H. J., In: Peppas, N. A., editor. *Hydrogels in medicine and pharmacy, II*, Boca Raton, FL: CRC Press, 1987, p. 49

Peppiatt, S. J., and Sambles, J. R., *Proc. R. Soc. Lond. A* **345** (1975) 387-399

Peppiatt, S. J., *Proc. R. Soc. Lond. A* **345** (1975) 401-412

Perlovich, G. L., and Bauer-Brandl, A., *Pharm. Res.* **20** (2003) 471-478

Peters, K. F.; Cohen, J. B.; Chung, Y. W., *Phys. Rev. B* **57** (1998) 13430-13439

Porter, D. A. and Easterling, K. E., *Phase Transformations in Metals and Alloys*, 2nd ed., Nelson Thornes Ltd.: Cheltenham, UK, 1992

Puchert, M. K.; Timbrell, P. Y.; Lamb, R. N., *J. Vac. Sci. Technol. A* **14** (1996) 2220-2230

Qin, X.; Ju, Y.; Bernhard, S., and Yao, N., NSTI – *Nanotech 2005* Vol. **2** (2005) 9-12 (www.nsti.org)

Ram, S., *J. Mater. Sci.* **35** (2000) 3561-3571

Ram, S., *Mater. Sci. Eng. A* **304-306** (2001) 923-927

Rao, C. N. R. and Rao, K. J., *Phase Transitions in Solids, An approach to the study of the chemistry and physics of solids*, McGraw-Hill, 1978

Révész, Á., and Lendvai, J., *Nanostruc. Mater.* **10** (1998) 13-24

Reynolds, J. G. and Hart, B. R., *JOM* **56** (2004) 36-39

Rittner, M. N., *JOM* **56** (2004) 22-26

Rodríguez-Paéz, J. E.; Caballero, A. C.; Villegas, M.; Moure, C.; Durán, P.; Fernández, J. F., *J. Eur. Ceram. Soc.* **21** (2001) 925-930

Roncone, K., *JOM* **56** (2004) 31-33

Rupp, J. and Birringer, R., *Phys. Rev. B* **36** (1987) 7888-7890

Sakai, H., *Surf. Sci.* **351** (1996) 285-291

Sato, H.; Kitakami, O.; Sakurai, T.; Shimada, Y.; Otani, Y.; Fukamichi, K., *J. App. Phys.* **81** (1997) 1858-1862

Schaefer, H. E. and Würschum, R., *J. of The Less-Common Metals* **140** (1998) 161-169

Schaefer, H. E., Würschum, R., Birringer, R., and Gleiter, H, *J. of Less-common Metals* **140** (1988) 161-169

Schmidt, M.; Kusche, R.; Kronmueller, W.; von Issendorff, B.; Haberland, H., *Phys. Rev. Lett.* **79** (1997) 99-102

Shaw, L. L., *JOM* **52** (2000) 41-45

Sheng, H. W.; Xu, J.; Yu, L. G.; Sun, X. K.; Hu, Z. Q.; Lu, K., *J. Mater. Res.* **11** (1996) 2841-2851

Shim, J. G., Master Thesis: *Structural Relaxation in Glassy Metals and Other Glassy Materials by Enthalpy Measurements*, 1998

Shrivastava, K. N., *Nano Lett.* **2** (2002) 21-24

Silvidi, A. A., and Daunt, J. G., *Physical Review* **77** (1950) 125-129

Stix, G., "Little Big Science," Scientific American.com (September 16, 2001)

Storozhev, V. B., *Surf. Sci.* **397** (1998) 170-178

Sun, N. X. and Lu, K., *Phys. Rev. B* **54** (1996) 6058-6061

Takagi, M., *J. of The Phys. Soc. of Japan* **9** (1954) 359-363

The Royal Society and The Royal Academy of Engineering "*Nanoscience and Nanotechnologies: Opportunities and Uncertainties,*" (July 29, 2004)

Thornton, G., *Science* **300** (2003) 1378-1379

Tinghe, B. J., In: Peppas, N. A., editor. *Hydrogels in medicine and pharmacy, II,* Boca Raton, FL: CRC Press, 1987, p. 53

Turnbull, D., *J. Appl. Phys.* **21** (1950) 1022-1027

Wakefield, G.; Keron, H. A.; Dobson, P. J.; Hutchison, J. L., *J. Phys. Chem. Solids* **60** (1999) 503-508

Wang, J.; Cheng, X.; Wang, G.; Wang, B.; Lu, W.; Zhao, J., *Phys. Rev. B* **66** (2002) 085408(1-5)

Wasserman, H. J. and Vermaak, J. S., *Surf. Sci.* **22** (1970) 164-172

Wautelet, M., *Phys. Lett. A* **246** (1998) 341-342

Weertman, J., *Mater. Sci. Eng. A* **166** (1993) 161-167

Wichterle, O., and Lim, D., *Nature* **185** (1960) 117-118

Wronski, C. R. M., *Brit. J. Appl. Phys.* **18** (1967) 1731-1737

Wu, R.; Xie, C., Hu, J.; Xia, H.; Wang, A., *Scripta Mater.* **43** (2000) 841-846

Wu, R.; Xie, C., Wu, J.; Zhang, J.; Wang, A., *Mater. Sci. Eng. A* **328** (2002) 196-200

Wu, R.; Xie, C.; Hu, J.; Xia, H.; Wang, A., *J. Cryst. Growth* **217** (2000) 274-280

Wu. R.; Xie, C., *Mater. Res. Bulletin* **39** (2004) 637-645

Yan, Y.; Liu, P.; Wen, J. G.; To, B.; Al-Jassim, M. M., *J. Phys. Chem. B* **107** (2003), 9701-9704

Zhang, H. Z. and Banfield, J. F., *J. Mater. Chem.* **8** (1998) 2073-2076

Zhang, H. Z. and Banfield, J. F., *J. Mater. Res.* **15** (2000) 437-448

Zhang, H. Z. and Banfield, J. F., *J. Phys. Chem. B* **104** (2000) 3481-3487

Zhang, H. Z. and Banfield, J. F., *Nanostruc. Mater.* **10** (1998) 185-194

Zhang, H. Z.; Huang, F.; Gilbert, B.; Banfield, J. F., *J. Phys. Chem. B* **107** (2003) 13051-13060

Zhang, H. Z.; Huang, F.; Gilbert, B.; Banfield, J. F., *Nature* **424** (2003) 1025-1029

Zhao, M.; Zhou.; X. H.; Jiang, Q., *J. Mater. Res.* **16** (2001) 3304-3308

Zhao, S. J.; Wang, S. Q.; Cheng, D. Y.; Ye, H. Q., *J. Phys. Chem. B* **105** (2001) 12857-12860

Zhong, J.; Jin, Z. H., and Lu, K., *J. Phys.: Condens. Matter* **13** (2001) 11443-11452

Vlachos, D. S., and Xenoulis, A. C., *Nanostruc. Mater.* **10** (1998) 1355-1361

http://www.integran.com/applications/consumer.htm

http://www.apt-powders.com/zinclear.htm

http://www.loeralusa.com/research.nanosomes.aspx

http://nano.cancer.gov

http://www.nano.csiro.au/welcome.htm

http://www.gatan.com/analysis/eftem_stem.html

Appendix A

A.1 Experimental heat capacities of solid and liquid zinc

M_{Zn} = 65.409 g mole^{-1} (Grønvold and Stølen, 2003)

T (K)	$C_{p,m}$ (J K^{-1} mol^{-1})	T (K)	$C_{p,m}$ (J K^{-1} mol^{-1})
Solid zinc, sample 1		631.92	29.44
302.24	25.56	640.91	29.62
309.26	25.57	649.91	29.79
316.25	25.72	658.91	30.03
323.23	25.75	667.92	30.24
330.24	25.84	674.45	30.59
337.25	25.91	682.05	30.65
344.24	25.98	684.81	30.76
351.24	26.00	684.85	30.75
358.27	26.10	685.15	30.62
365.28	26.19		
372.30	26.20	*Liquid zinc*	
379.30	26.31	*Sample 1*	
386.28	26.44	698.52	33.40
393.26	26.47	705.56	33.31
400.24	26.52	751.49	33.01
407.22	26.54	760.58	32.79
315.21	25.61	769.71	32.74
323.99	25.77	778.84	32.68
332.77	25.88	788.03	32.62
341.53	25.94	698.33	33.29
350.27	26.03	697.39	33.34
359.01	26.10	701.37	33.31
367.73	26.21		
376.45	26.31	*Sample 2*	
385.17	26.35	747.64	32.82
393.88	26.46	757.94	32.75
411.30	26.60	768.33	32.78
420.01	26.71	778.79	32.64
428.72	26.80	789.18	32.42
437.44	26.89	799.20	32.45
446.17	26.94	808.77	32.38
454.91	27.06	818.03	32.38
463.67	27.15	828.62	32.56
472.43	27.24	839.44	32.48
481.20	27.34	850.29	32.25
489.98	27.42	861.09	32.45
498.77	27.54	872.00	32.25
507.59	27.63	882.94	32.25
516.41	27.72	893.93	32.33
525.24	27.80	932.62	32.28
534.35	27.90		
542.93	28.01		
551.79	28.18		
560.64	28.39		
569.50	28.39		
578.39	28.55		
587.29	28.68		
596.15	28.81		
605.13	28.99		
614.04	29.08		
622.96	29.27		

A.2 Thermodynamic properties of zinc at selected temperatures

T (K)	$C_{p,m}$ ($J\ K^{-1}\ mol^{-1}$)	$\Delta_0^T H_m$ ($J\ mol^{-1}$)	$\Delta_0^T S_m$ ($J\ K^{-1}\ mol^{-1}$)	$-(\Delta_0^T G_m - \Delta_0^0 H_m)/T$ ($J\ K^{-1}\ mol^{-1}$)
0	0	0	0	0
0.5	0.0004	0.00007	0.00026	0.00012
0.84	0.0012	0.00035	0.00066	0.00024
1	0.0007	0.00045	0.00078	0.00033
2	0.0018	0.0016	0.0016	0.00080
4	0.0071	0.0095	0.0041	0.00173
5	0.012	0.019	0.0061	0.00230
10	0.158	0.325	0.043	0.0105
15	0.731	2.325	0.198	0.0430
20	1.798	8.473	0.544	0.120
30	4.851	40.90	1.817	0.454
40	8.133	106.05	3.669	1.018
50	11.009	202.16	5.802	1.758
60	13.400	324.60	8.027	2.617
80	16.939	630.39	12.40	4.522
100	19.335	994.58	16.45	6.509
120	21.041	1399.3	20.14	8.479
140	22.255	1833.0	23.48	10.39
160	23.055	2286.7	26.51	12.22
180	23.564	2753.2	29.25	13.96
200	23.989	3228.7	31.76	15.62
220	24.364	3712.4	34.06	17.19
240	24.693	4203.0	36.20	18.69
260	24.988	4699.9	38.19	20.11
280	25.252	5202.3	40.05	21.47
298.15	25.470	5662.7	41.64	22.65
300	25.492	5709.8	41.80	22.77
350	26.02	6997.9	45.77	25.77
400	26.51	8311.3	49.28	28.50
450	27.01	9649.1	52.43	30.98
500	27.54	11013	55.30	33.27
550	28.14	12404	57.95	35.40
600	28.87	13829	60.43	37.38
650	29.84	15295	62.78	39.25
692.681	30.96	16591	64.71	40.76
$\Delta_{fus}H_m = 7070\ J\ mol^{-1}$				
692.681	33.42	23661	74.91	40.76
700	33.34	23905	75.26	41.12
750	32.85	25559	77.55	43.47
800	32.53	27193	79.65	45.67
850	32.35	28815	81.62	47.72
900	32.28	30430	83.47	49.66
940	32.31	31722	84.87	51.13

Appendix B
DSC Errors

Temperature Scan	:	$\pm\,0.2$ K
Heat Flow Signal	:	$\pm\,2$ % (mW)
Integrated Exotherm and Endotherm with a linear baseline	:	$\pm\,2$ % (J/ K)
Onset Temperature	:	$\pm\,0.2$ K

Appendix C

XRD Sample Calculation of Crystal Size and Error Analysis

C.1 Crystal Size Determination from XRD Peak Broadening

The sample calculation of crystal size determination of the pharmaceuticals embedded in polyHEMA matrix is provided for Benzoic Acid (400) peak at 2θ of 16.25°. The corresponding measured breadth at half maximum (FWHM) is 3.12×10^{-3} radians. The standard FWHM of the pure Benzoic Acid at the same 2θ is 2.99×10^{-3} radians. The total broadening corresponds to crystal size effect is calculated according to Warren's method:

$$B = \sqrt{B_M^2 - B_S^2}$$

$$B = \sqrt{(3.12 \times 10^{-3})^2 - (2.99 \times 10^{-3})^2}$$

$$B = 8.9 \times 10^{-4}\text{ rad}$$

The crystal size determination is then calculated according to Scherrer's formula:

$$t = \frac{0.9\lambda}{B\cos\theta}$$

$$t = \frac{0.9 \times 0.154\text{ nm}}{(8.9 \times 10^{-4}) \times \cos(8.125)} = 157.64\text{ nm}$$

C.2 XRD Error Analysis

An error of 5 % was used for the measured breadth width values taken at full width half maximum (FWHM). In addition to that, an error of ± 0.04 was taken for the value of 2θ (two times the Bragg angle). Using this error value, calculations were conducted and errors were carried through each stage of the calculation.

135

Errors in Measured Breadth (B_M) of embedded Benzoic Acid in polyHEMA matrix

$$B_M = 3.12 \times 10^{-3} \text{ radians}$$

$$\text{error} = 5 \% \times B_M$$

$$= 5 \% \times (3.12 \times 10^{-3}) = 1.56 \times 10^{-4} \text{ radians}$$

$$B_M \pm \text{error} = 3.12 \times 10^{-3} \pm 1.56 \times 10^{-4} \text{ radians}$$

Thus the range of B_M is 2.96×10^{-3} to 3.27×10^{-3} radians

Errors in Standard Breadth (B_S) of pure Benzoic Acid sample

$$B_S = 2.99 \times 10^{-3} \text{ radians}$$

$$\text{error} = 5 \% \times B_S$$

$$= 5 \% \times (2.99 \times 10^{-3}) = 1.50 \times 10^{-4} \text{ radians}$$

$$B_S \pm \text{error} = 2.99 \times 10^{-3} \pm 1.5 \times 10^{-4} \text{ radians}$$

Thus the range of B_S is 2.84×10^{-3} to 3.14×10^{-3} radians

Errors in the Total Breadth (B)

$$B + \text{error} = \sqrt{(B_M + \text{error})^2 - (B_S + \text{error})^2} = 9.35 \times 10^{-4} \text{radians}$$

$$B - \text{error} = \sqrt{(B_M - \text{error})^2 - (B_S - \text{error})^2} = 8.48 \times 10^{-4} \text{radians}$$

Thus the range of B is 8.48×10^{-4} to 9.35×10^{-4} radians

Errors in Bragg Angle (θ)

An error of 0.02 degrees (3.94×10^{-3} radians) was added and subtracted from the θ values determined from XRD data. For 2 θ value of 16.25°, or θ value of 8.125°:

$$\theta \pm \text{error} = 8.125° \pm 0.02°$$

136

Thus the range of θ is $8.105°$ to $8.145°$, or 0.139 to 0.145 radians.

Error in crystallite size (t)

Using B of 9.35×10^{-4} radians and θ of 0.145 radians:

$$t = \frac{0.9 \times 0.154 \, \text{nm}}{(9.35 \times 10^{-4}) \times \cos(0.145)} = 149.8 \, \text{nm}$$

Using B of 8.48×10^{-4} radians and θ of 0.139 radians:

$$t = \frac{0.9 \times 0.154 \, \text{nm}}{(8.48 \times 10^{-4}) \times \cos(0.139)} = 165 \, \text{nm}$$

Range of t of 149.8 to 165 nm leads to an average t value of 157.4 nm with error of ± 7.6 nm.